nature metabolism

Article

https://doi.org/10.1038/s42255-025-01352-4

BDH2-driven lysosome-to-mitochondria iron transfer shapes ferroptosis vulnerability of the melanoma cell states

Received: 28 October 2024

Accepted: 18 July 2025

Published online: 16 September 2025

Check for updates

A list of authors and their affiliations appears at the end of the paper

Iron sustains cancer cell plasticity, yet it also sensitizes the mesenchymal, drug-tolerant phenotype to ferroptosis. This posits that iron compartmentalization must be tightly regulated. However, the molecular machinery governing organelle Fe(II) compartmentalization remains elusive. Here, we show that BDH2 is a key effector of inter-organelle Fe(II) redistribution and ferroptosis vulnerability during melanoma transition from a melanocytic (MEL) to a mesenchymal-like (MES) phenotype. In MEL cells, BDH2 localizes at the mitochondria–lysosome contacts (MLCs) to generate the siderophore 2,5-dihydroxybenzoic acid (2,5-DHBA), which ferries iron into the mitochondria. Fe(II) transfer by BDH2 supports mitochondrial bioenergetics, which is required to maintain lysosomal acidification and MLC formation. Loss of BDH2 alters lysosomal pH and MLC tethering dynamics, causing lysosomal iron sequestration, which primes MES cells for ferroptosis. Rescuing BDH2 expression, or supplementing 2,5-DHBA, rectifies lysosomal pH and MLCs, protecting MES cells from ferroptosis and enhancing their ability to metastasize. Thus, we unveil a BDH2-dependent mechanism that orchestrates inter-organelle Fe(II) transfer, linking metabolic regulation of lysosomal pH to the ferroptosis vulnerability of the mesenchymal, drug-tolerant cancer cells.

Iron sustains a wide range of cellular processes, and maintenance of intracellular iron homeostasis is crucial for cell viability[1–3]. Lysosomes regulate iron import, export and mobilization in the cell, whereas mitochondria are the major cellular site of iron utilization[4–6]. Mitochondria utilize iron for the biosynthesis of haem and Fe–S clusters, which are cofactors of mitochondrial enzymes involved in the tricarboxylic acid (TCA) cycle and respiratory-chain complexes, as well as of several non-mitochondrial enzymes[7,8]. However, intracellular iron can be detrimental to the cell because of the reactive nature of its redox-active ferrous form (Fe(II))[9–13]. Fe(II) can react with hydrogen peroxide in Fenton reactions, generating reactive oxygen species (ROS) that can induce lethal damage to cellular components[9–13]. Cellular membranes rich in polyunsaturated fatty acids are particularly prone to ROS attack. Lipid peroxidation is an established hallmark of ferroptosis, an iron-dependent lytic form of cell death driven by dysregulation of major cellular antioxidant systems[9,14–16]. This implies that intracellular iron compartmentalization needs to be tightly controlled.

Iron bolsters cancer cells' epigenetic and metabolic remodelling, thereby supporting cancer cell plasticity[11,17], which refers to the ability of cancer cells to transition from one cell state to another in response to environmental cues, including therapeutic insults[18,19]. Importantly, cancer cell plasticity is a key driver of therapeutic resistance and metastatic spread[17–20].

The accumulation of redox-active iron in lysosomes has been suggested to sustain the mesenchymal, drug-resistant phenotype[11,17] while priming these malignant cells for ferroptosis[11,13]. We therefore postulated that cancer cells evolved mechanisms to fine-tune intracellular iron compartmentalization effectively, enabling metabolic and

e-mail: julie.bonnereau@kuleuven.be; patrizia.agostinis@kuleuven.be

phenotypic plasticity while circumventing its toxic effects. Strikingly, the specific molecular machinery governing inter-organelle iron trafficking—and the impact of its disruption on cancer cell fate—remains unexplored.

Results

Inter-organelle iron redistribution is a hallmark of the melanoma phenotype switching

To unravel whether inter-organelle redistribution of Fe(II) occurs during the transition of cancer cell states, we used melanoma as a model of phenotype plasticity[21,22]. A key determinant of melanoma phenotypic identity is the microphthalmia-associated transcription factor (MITF), which promotes proliferation and differentiation while suppressing invasion[21–23]. Melanoma cells can reversibly switch between two major transcriptional states: an MITF^{hi} melanocytic (MEL) (or 'proliferative') to an MITF^{lo} mesenchymal-like (MES) (or 'invasive') phenotype. The MEL state is characterized by high levels of the transcription factor SOX10 and low levels of the receptor tyrosine kinase AXL. By contrast, the less-differentiated MES state exhibits high AXL levels, along with increased expression of the epithelial-to-mesenchymal transition (EMT) markers, such as SOX9 (ref. 24), EGFR and ZEB1 (ref. 25), and melanoma-specific regulators, such as TCF4 (ref. 26) (Extended Data Fig. 1a). These transcriptional states are linked to differences in invasion, metastasis, and therapy resistance[21,25,27,28].

We examined organelle iron redistribution in steady-state conditions in a panel of melanoma cell lines and short-term patient-derived melanoma cell lines, with a well-defined MEL (MITF^{hi}AXL^{lo}SOX10^{hi}) or MES (MITF^{lo}AXL^{hi}SOX9^{hi}) phenotype (Extended Data Fig. 1a and Supplementary Table 1). Compared with their MEL counterpart, MES cells displayed a modest increase in cellular Fe(II) levels in basal conditions and upon iron(II) overload with ferrous ammonium sulfate (FAS) (Extended Data Fig. 1b,c). Levels of the endogenous Iron Regulatory Protein 2 (IRP2), which undergoes proteasomal degradation in iron-replete cells[29,30], were lower in MES than in MEL cells, and this difference was further exacerbated by FAS treatment (Extended Data Fig. 1d,e). Chelating lysosomal iron with deferoxamine (DFO) enhanced IRP2 levels in both cell types (Extended Data Fig. 1d,e).

We then used super-resolution microscopy to image the intracellular compartmentalization of ferrous iron with various small-molecule fluorescent probes in conjunction with organelle-specific dyes: LysoTracker Green for late endosomes (LEs) and lysosomes, and MitoTracker Deep Red for the mitochondrial network. Total redox-active Fe(II) was detected with FerroOrange (Fig. 1a,b and Extended Data Fig. 1f,g), and mitochondrial iron and lysosomal iron were visualized using Mito-FerroGreen (Fig. 1c,d and Extended Data Fig. 1h–k) and RhoNox-M (Extended Data Fig. 1l,m), respectively.

MES cells were characterized by a marked accumulation of Fe(II) in LEs and lysosomes (Fig. 1a,b and Extended Data Fig. 1f,g,l,m) coupled with a reduced Fe(II) level in mitochondria (Fig. 1c,d and Extended Data Fig. 1h–k). By contrast, MEL cells displayed the opposite phenotype, with a clear mitochondrial iron distribution (Fig. 1a–d and Extended Data Fig. 1f–m).

Live imaging and colocalization analysis of FerroOrange-labelled MEL and MES cells transfected with CD63–enhanced GFP (eGFP) or Lamp1–eGFP to stain LEs only or LEs/lysosomes, respectively, confirmed that there was a significant accumulation of iron in the acidic vesicles of MES cells when compared with MEL cells (Extended Data Fig. 1n–t). No significant differences in mitochondrial mass or membrane potential were observed between MEL and MES cells (Extended Data Fig. 1u,v). These results suggest that the differential iron compartmentalization under steady-state conditions was not driven by gross mitochondrial alterations, but could involve a defect in the egress of iron from LEs/lysosomes (hereafter referred to as 'lysosomes' for brevity)[4–6].

In line with their low mitochondrial Fe(II) content, MES cells exhibited reduced expression of iron-dependent oxidative phosphorylation (OXPHOS) complexes (complexes I, II, III and IV)[31] (Extended Data Fig. 2a,b) and an overall diminished basal and maximal respiratory capacity (or oxygen consumption rate (OCR)) (Fig. 1e and Extended Data Fig. 2c). In the MEL cells, chelation of lysosomal iron by DFO lowered mitochondrial iron levels (Fig. 1f,g) and reduced mitochondrial respiration (Fig. 1e and Extended Data Fig. 2c) while further diminishing the low OCR of the MES cells (Fig. 1e and Extended Data Fig. 2c), consistent with the established requirement of mitochondrial iron for efficient respiration[4–6,11,32]. Similarly, ironomycin, a compound that sequesters iron(II) in lysosomes[11] (Extended Data Fig. 2d,e), and liproxstatin-1 (Lip-1), which localizes to the lysosomes and binds to iron in this subcellular compartment[13] (Extended Data Fig. 2h–k), reduced mitochondrial iron levels and the OCR in MEL cells[33] (Extended Data Fig. 2d–k).

We then tested whether silencing the expression of MITF in metabolically proficient MEL cells could trigger a redistribution of iron from mitochondria to lysosomes. In line with this, stable depletion (by CRISPR/Cas9) (Fig. 1h) or reduction (by short hairpin RNA (shRNA)) of MITF in MEL cells (Extended Data Fig. 2l) induced the accumulation of Fe(II) in lysosomes (Fig. 1i,j and Extended Data Fig. 2m,n). This effect was coupled with a concomitant decrease of iron levels in the mitochondria (Fig. 1k,l and Extended Data Fig. 2o,p), compromised OCR capacity (Fig. 1m and Extended Data Fig. 2q–s) and reduced levels of the iron-dependent OXPHOS complexes (Extended Data Fig. 2t–w).

Overall, these data demonstrate that organelle iron compartmentalization is rewired during melanoma phenotype switching.

Mitochondria–lysosome contacts control iron compartmentalization in melanoma cells

We next sought to characterize the molecular mechanisms underlying the differential organellar Fe(II) compartmentalization of distinct melanoma cell states. Lysosomes and mitochondria communicate by the dynamic formation of subcellular sites of close appositions, called mitochondria–lysosome contact sites (MLCs)[34,35].

MLC establishment requires the active GTP-bound form of the lysosomal GTPase RAB7 (ref. 34). Intriguingly, the downregulation of RAB7 expression has been shown to favour melanoma invasion and metastasis[36]. Consistently, RAB7 levels were lower in MES cells than in MEL cells (Extended Data Fig. 3a). We therefore posited that the differential inter-organellar iron redistribution of these melanoma cell phenotypes could involve dysregulation of MLCs.

The characterization of MLCs is technically challenging due to their nanoscopic size (≤10 nm) and highly transient nature (contact duration of >10 s)[34]. We then used the newly generated split GFP-based contact site sensors (SPLICS) engineered to visualize MLCs of varying widths, specifically short (around 4–5 nm) and long (around 10 nm) interactions[37] (Fig. 2a). Transfection of MEL and MES cells with the SPLICS sensors, combined with quantitative imaging, revealed that there were fewer short and long MLCs in MES cells than in MEL cells (Fig. 2b–e).

MLCs have been implicated in the trafficking of calcium, amino acids and cholesterol from lysosomes to mitochondria, whereas their role in iron transfer has only been hypothesized[35]. To image the dynamic formation of MLCs and concomitantly measure iron(II) transfer from lysosomes to mitochondria, we used super-resolution structured illumination microscopy (SIM) live imaging in MEL cells costained with LysoTracker Green, MitoTracker Deep Red and rhodamine B-[(2,2′-bipyridine-4-yl)-aminocarbonyl]benzyl ester (RDA). RDA is a mitochondrial-targeted fluorescence probe that experiences quenching on binding to ferrous iron[38]. Tracking lysosomal movements over time revealed that, on stable MLC formation (with a contact duration in the time range of 10–60 s), RDA fluorescence intensity diminished in the lysosomal–mitochondrial overlapping area, indicative of inter-organelle iron transfer (Fig. 2f,g). Conversely, in the absence of MLCs, mitochondrial RDA fluorescence remained stable over the same temporal interval (Fig. 2f,g). This suggests that the dynamic interaction

https://doi.org/10.1038/s42255-025-01352-4

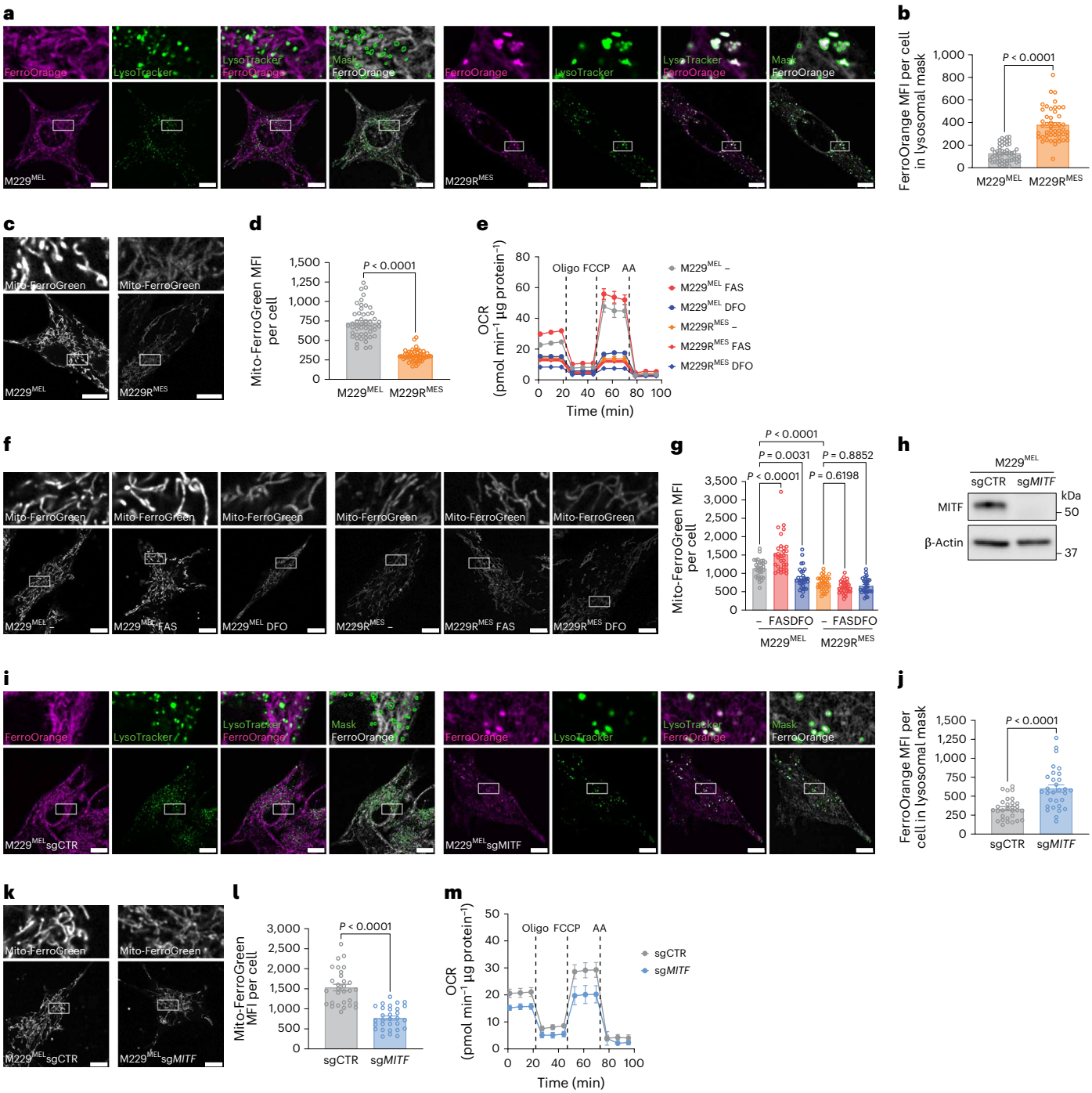

Fig. 1 | Inter-organelle iron redistribution is a hallmark of the melanoma phenotype switching. a,**b**, Representative images (**a**, scale bars, 10 µm) and quantification of lysosomal iron using FerroOrange mean fluorescence intensity (MFI) per cell in the lysosomal mask (**b**) in M229^{MEL} ($n = 54$) and M229R^{MES} ($n = 48$) cells (three independent experiments). **c**,**d**, Representative images (**c**, scale bars, 10 µm) and quantification of mitochondrial iron levels using Mito-FerroGreen MFI per cell (**d**) in M229^{MEL} ($n = 50$) and M229R^{MES} ($n = 50$) cells (three independent experiments). **e**, OCR of M229^{MEL} and M229R^{MES} cells in basal (−), FAS-treated and DFO-treated conditions ($n = 5$). **f**,**g**, Representative images (**f**, scale bars, 10 µm) and quantification of mitochondrial iron using Mito-FerroGreen MFI per cell (**g**) in M229^{MEL} basal ($n = 31$), FAS-treated ($n = 30$) and DFO-treated ($n = 30$) cells and M229R^{MES} basal ($n = 30$), FAS-treated ($n = 30$) and DFO-treated ($n = 30$) cells (three independent experiments). **h**, Representative western blot of MITF in M229^{MEL} control single-guide RNA (sgCTR) or *MITF*-targeted sgRNA (sg*MITF*) cells ($n = 3$). β-Actin was used as a loading control. **i**,**j**, Representative images (**i**, scale bars, 10 µm) and quantification of lysosomal iron levels using FerroOrange MFI per cell within the lysosomal mask (**j**) in M229^{MEL} sgCTR ($n = 30$) or sg*MITF* ($n = 30$) cells (three independent experiments). **k**,**l**, Representative images (**k**, scale bars, 10 µm) and quantification of mitochondrial iron levels using Mito-FerroGreen MFI per cell (**l**) in M229^{MEL} sgCTR ($n = 30$) or sg*MITF* ($n = 30$) cells (three independent experiments). **m**, OCR of M229^{MEL} sgCTR or sg*MITF* cells ($n = 4$). Magnified images of the boxed areas are shown for detail (**a**, **c**, **f**, **i** and **k**). Data are presented as mean ± s.e.m. Statistical significance was assessed by unpaired two-tailed Student's *t*-test (**b**,**d**,**j**,**l**) and one-way analysis of variance (ANOVA) (**g**).

between lysosomes and mitochondria is crucial for efficient iron transfer between these organelles.

To assess the role of RAB7 in MLC formation, we stably transduced RAB7^{lo} MES cells with wild-type (WT) RAB7 or its constitutively active GTP-bound mutant RAB7-Q67L, or the dominant negative mutant RAB7-T22N (Extended Data Fig. 3b), which cannot hydrolyse GTP[34]. Although the expression of RAB7 WT or RAB7-Q67L in MES cells increased the number of short MLCs, RAB7-T22N decreased their formation (Fig. 2h,i). None of the RAB7 mutants exhibited altered formation of long MLCs (Extended Data Fig. 3c,d), suggesting that these mitochondria–lysosomes appositions tend to be more stable and are less subject to changes in RAB7 expression or activity, in line with a recent report[37].

Because Ca^{2+} transfer between lysosomes and mitochondria occurs through RAB7-regulated short MLCs[37,39], we hypothesized that increased levels of lysosomal Fe(II) in MES cells specifically involves defects in RAB7-mediated short MLCs. Expression of RAB7 WT led to a decrease in lysosomal Fe(II) (Extended Data Fig. 3e,f), and this effect was blunted by expressing dominant negative RAB7-T22N (Extended Data Fig. 3e,f). However, these changes were mild and did not lead to elevated mitochondrial Fe(II) content (Extended Data Fig. 3g,h) or mitochondrial respiration of the MES cells (Extended Data Fig. 3i,j) to the extent observed in MEL cells.

To capture MLC dynamics, we used super-resolution live imaging in cells stained with LysoTracker Green and MitoTracker Deep Red. Compared with their MEL counterparts, MES cells exhibited longer contact duration (Extended Data Fig. 4a,b), a phenotype reminiscent of lysosomal pH defects[40]. In line with this, lysosomes of MES cells displayed a reduced acidity (Fig. 2j and Extended Data Fig. 4c,d), an attenuated proteolytic activity (Extended Data Fig. 4e), and an enlarged morphology (without a change in density) (Fig. 2k,l and Extended Data Fig. 4f,g), suggestive of impaired lysosomal function[1].

Preserving acidic lysosomal pH has been previously linked to the ability of lysosomes to release iron[4–6]. Genetic manipulation of *RAB7* levels or activity in MES cells did not induce lysosomal acidification, whereas RAB7-T22N showed a trend toward further alkalinization of the lysosomal pH (Extended Data Fig. 4h). Overall, these findings indicate that, although RAB7 can restore the formation of short MLCs in MES cells, its impact on lysosomal iron trafficking is limited. This is because RAB7 cannot reverse lysosomal pH, and as a result, it fails to enhance mitochondrial iron uptake and restore the OCR capacity of these cells.

To evaluate the relevance of lysosomal pH for organellar Fe(II) redistribution, we rectified the defective lysosomal pH of MES cells by exploiting poly(D,L-lactide-co-glycolide) (PLGA)-acidic nanoparticles (acNPs)[41–43] (Fig. 2m), which have been previously used to restore lysosomal acidification defects in cellular and in vivo models of lysosomal diseases[42,43]. In accordance with this, supplementing MES cells with acNPs rescued the acidic lysosomal pH (Fig. 2n), improved lysosomal morphology (Fig. 2o,p), reduced lysosomal iron load (Fig. 2q,r), increased the integrity of short MLCs (Fig. 2s,t) and partially, yet significantly, rescued mitochondrial Fe(II) levels (Fig. 2u,v). However, mitochondrial respiration was not fully rescued by acNPs either (Extended Data Fig. 4i,j). Notably, providing FAS, which enters the cell independently of endocytosis, increased total iron levels in both MEL and MES cells (Extended Data Fig. 1b,e and Extended Data Fig. 4k), but failed to elevate mitochondrial iron levels and OCR in MES cells (Fig. 1e–g).

Thus, all tested interventions—genetic (*RAB7*) or chemical (acNPs)—that improve the stability of short MLCs and the release of lysosomal iron do not fully rescue mitochondrial Fe(II) content and OCR capacity. This suggests that additional molecular players operating at the mitochondria–lysosome interface are involved.

The MES phenotype is associated with reduced levels of BDH2, the mammalian homologue of the bacterial EntA

To gain insights into potential mediators of inter-organelle iron trafficking, we performed an in silico analysis using the published transcriptome of 51 melanoma cell lines classified according to their cell status[28]. We compiled a literature-based list of all iron-metabolism-related genes (Supplementary Table 2) and extracted their expression values from this dataset to obtain an iron-metabolism-specific transcriptional signature of melanoma lines. A semi-supervised principal component analysis of the dataset, including 110 iron-related genes, separated melanoma cells into two clusters associated with the MEL and MES melanoma phenotypes (Fig. 3a). Differential expression (DE) analysis revealed that MES cells were hallmarked by the downregulation of the lysosomal ATP6V genes (encoding essential subunits of the lysosomal proton pump v-ATPase)[4–6], *SLC11A2* (or *DMT1*, the major lysosomal iron transporter and exporter)[44–46], *MCOLN1* (or *TRPML1*, the non-selective cation channel permeable to Fe(II) and Ca^{2+})[47] and several genes encoding mitochondrial proteins involved in Fe–S cluster and haem synthesis, such as *BOLA3* (ref. 48), *MMS19* (ref. 49) *HMOX2* (ref. 50,51) and *UROS*[52,53] (Fig. 3b, Extended Data Fig. 5a and Supplementary Table 3). As expected, the MLC mediator *RAB7*, which is under the control of the melanocytic transcription factor SOX10 and the oncogene MYC[36], was also downregulated, altogether confirming our functional data in a larger set of human melanoma cell lines (Fig. 3b, Extended Data Fig. 5a

Fig. 2 | Mitochondria–lysosome contacts regulate iron compartmentalization in melanoma cells. a, Schematics of the SPLICS sensor mechanism. Parts of this figure were created using BioRender. **b**,**c**, Representative images (**b**, scale bars, 10 µm) and quantification of short MLCs per cell (**c**) in M229^{MEL} ($n = 30$) and M229R^{MES} ($n = 29$) cells (three independent experiments). **d**,**e**, Representative images (**d**, scale bars, 10 µm) and quantification of long MLCs per cell (**e**) in M229^{MEL} ($n = 29$) and M229R^{MES} ($n = 30$) cells (three independent experiments). **f**,**g**, Representative images (**f**, scale bars, 1 µm) and quantification of the average difference (Δ) in the RDA MFI per cell, measured between the end and start of MLC events (**g**); quantification compares 'MLC' regions, that is, overlapping MitoTracker$^+$LysoTracker$^+$ area (in white, $n = 22$), to 'No MLC' regions, that is, mean RDA intensity in the MitoTracker$^+$ area during the same time interval ($n = 20$) in M229^{MEL} cells (four independent experiments). *t*, time. **h**,**i**, Representative images (**h**, scale bars, 10 µm) and quantification of short MLCs per cell (**i**) in M229^{MES} EV ($n = 30$), RAB7 WT ($n = 30$), RAB7-Q67L ($n = 28$) and RAB7-T22N ($n = 40$) cells (three independent experiments). **j**, Relative lysosomal pH levels (LysoSensor MFI) of M229R^{MES} versus M229^{MEL} cells ($n = 3$). **k**,**l**, Representative images (**k**, scale bars, 10 µm for whole-cell images, 0.5 µm for magnified images) and quantification of cellular density and average area (**l**) of lysosomes in M229^{MEL} ($n = 30$) and M229R^{MES} ($n = 30$) cells stained with LysoTracker (three independent experiments). **m**, Schematics of the acNP mechanism. Parts of this figure were created in BioRender. **n**, Relative lysosomal pH levels (LysoSensor MFI) of acNP-treated (+) versus untreated (–) M229R^{MES} cells ($n = 4$). **o**,**p**, Representative images (**o**, scale bars, 10 µm for whole-cell image; 0.5 µm for magnified images) and quantification of average area (**p**) of lysosomes in acNP-treated ($n = 79$) and untreated ($n = 76$) M229R^{MES} cells (four independent experiments). **q**,**r**, Representative images (**q**, scale bars, 10 µm) and quantification of lysosomal iron levels using FerroOrange MFI per cell in the lysosomal mask (**r**) in acNP-treated ($n = 59$) and untreated ($n = 60$) M229R^{MES} cells (three independent experiments). **s**,**t**, Representative images (**s**, scale bars, 10 µm) and quantification of the number of short MLCs per cell (**t**) in acNP-treated ($n = 26$) and untreated ($n = 29$) M229R^{MES} cells (three independent experiments). **u**,**v**, Representative images (**u**, scale bars, 10 µm) and quantification of mitochondrial iron using Mito-FerroGreen MFI per cell (**v**) in acNP-treated ($n = 60$) and untreated ($n = 61$) M229R^{MES} cells (four independent experiments). Data in bar plots are shown as mean ± s.e.m. Data in the box plot (**g**) represent the median (centre line), the 25th and 75th percentiles (bounds of the box); and the whiskers indicate the minimum and maximum values. Statistical significance was assessed by unpaired two-tailed Student's *t*-test (**c**,**e**,**g**,**l**,**p**,**r**,**t**,**v**), one-way ANOVA (**i**) and two-tailed one-sample *t*-test (**j**,**n**). Magnified images of the boxed areas are shown for detail (**o**, **q** and **u**).

https://doi.org/10.1038/s42255-025-01352-4

and Supplementary Table 3). However, MES cells showed a consistent upregulation of *SLC25A37* (coding for Mitoferrin-1, the inner mitochondrial membrane iron transporter)[54–56], *STEAP3* (lysosomal ferric reductase that reduces Fe(III) to Fe(II))[57] and *CD44* (a transmembrane glycoprotein involved in cellular uptake of iron via endocytosis in mesenchymal cells)[17] (Fig. 3b, Extended Data Fig. 5a and Supplementary Table 3). Of note, the levels of *SLC25A28*, encoding Mitoferrin-2, were unchanged (Fig. 3b, Extended Data Fig. 5a and Supplementary

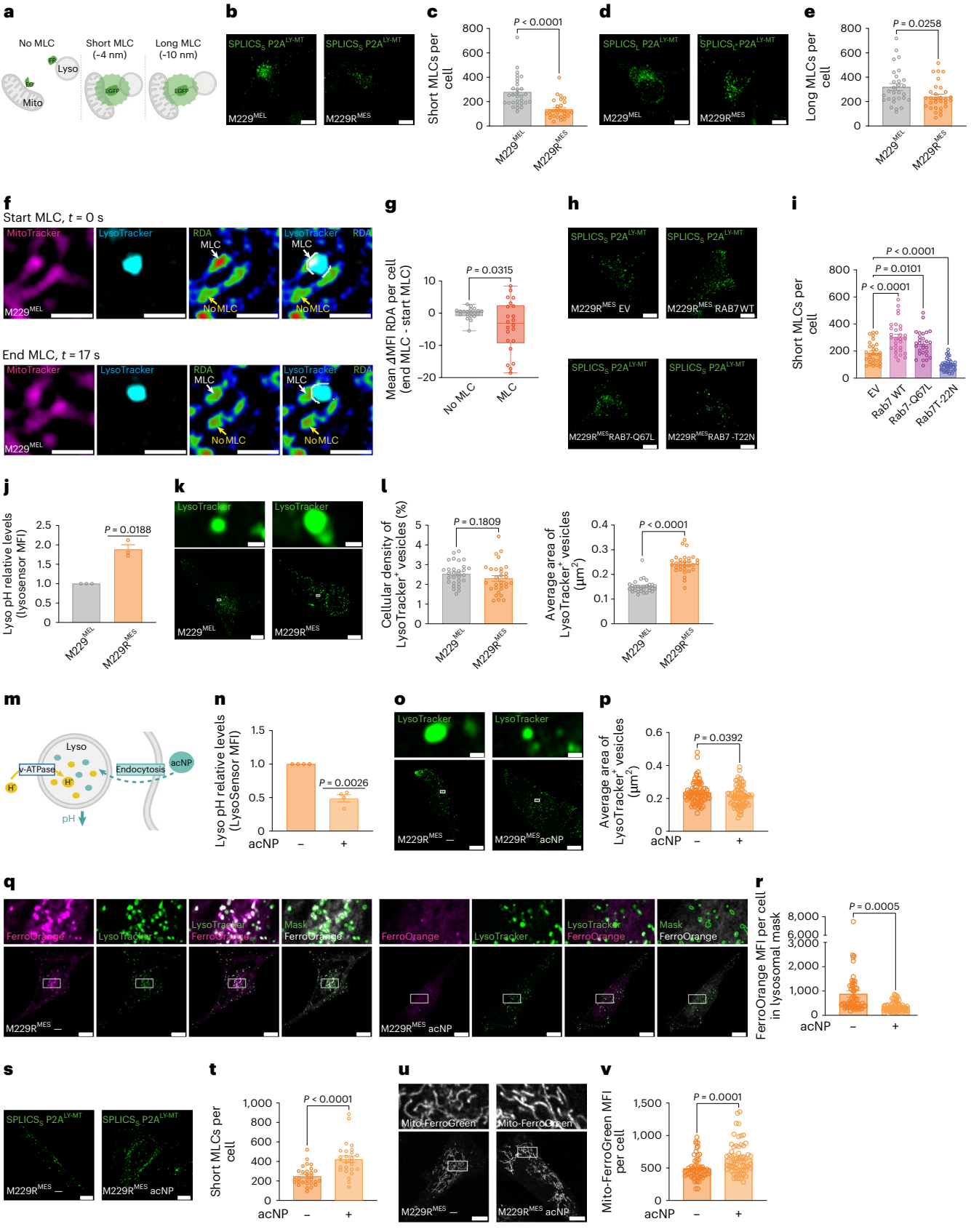

https://doi.org/10.1038/s42255-025-01352-4

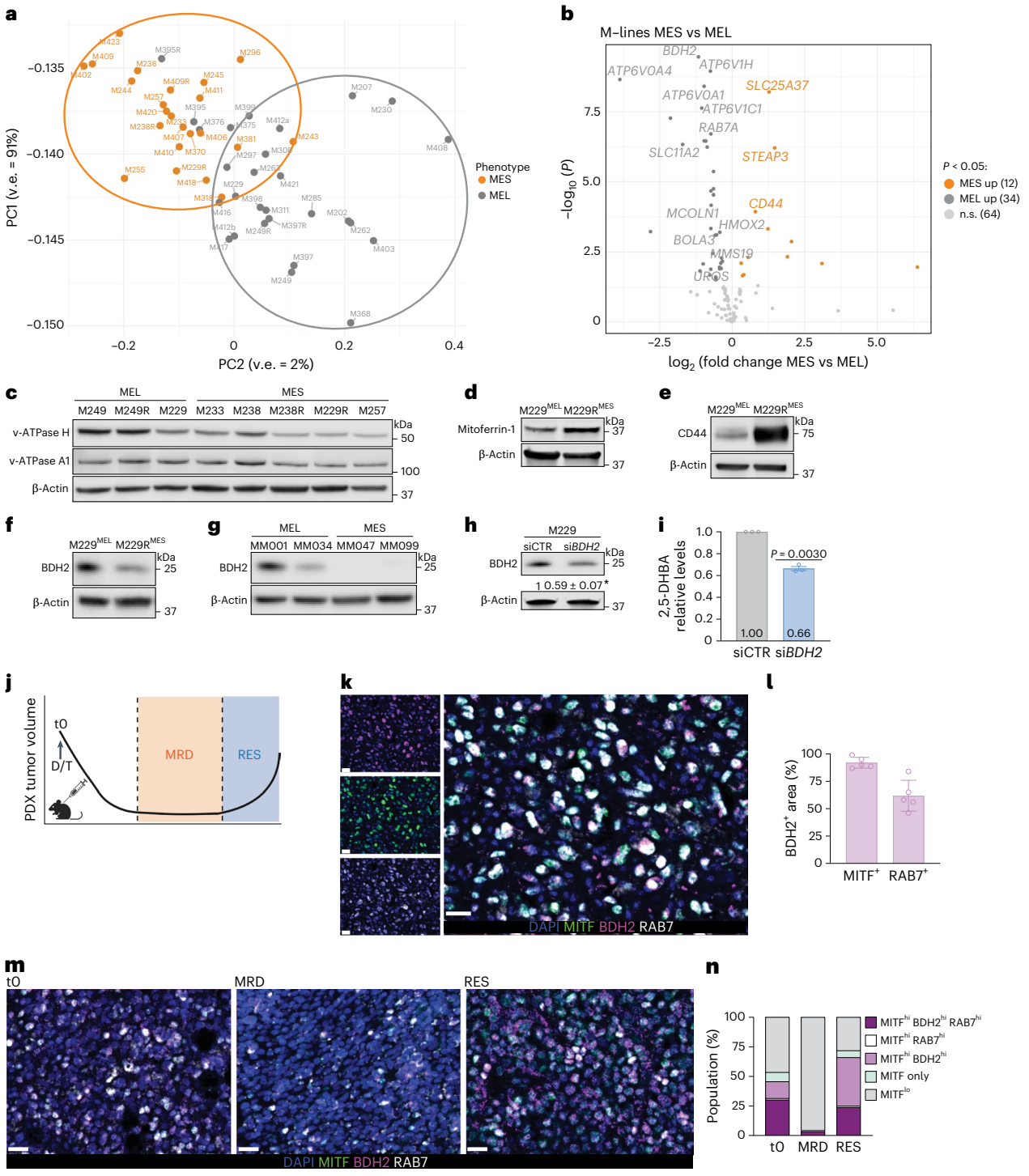

Fig. 3 | The MES phenotype is associated with reduced levels of BDH2, the mammalian homologue of the bacterial EntA. a, Principal component analysis (PCA) plot showing the clustering pattern of melanoma cell lines[28] on the basis of the expression of 106 iron metabolism-related genes. Cell lines are coloured by their phenotype (MES in orange, MEL in grey). v.e., variance explained. **b**, Volcano plot showing the statistically significant differentially expressed (DE) iron-metabolism-related genes between the two melanoma clusters (or melanoma M-lines), MES versus MEL. The number of significant genes per condition is reported in brackets in the legend (*t*-test, *P* value threshold < 0.05; n.s., not significant). **c**–**e**, Representative western blot of v-ATPase H and v-ATPaseA1 (**c**), Mitoferrin-1 (**d**) and CD44 (**e**) in MEL (M249, M249R and M229) and MES (M233, M238, M238R, M229R and M257) cells ($n = 2$). **f**,**g**, Representative western blot of BDH2 in MEL (M229, MM001, MM034) and MES (M229R, MM047, MM099) cells ($n = 3$). **h**, Representative western blot and quantification of BDH2 in $M229^{MEL}$ control siRNA (siCTR) or siRNA targeting *BDH2* (si*BDH2*) cells ($n = 3$). **i**, Relative 2,5-DHBA levels in $M229^{MEL}$ siBDH2 versus siCTR cells ($n = 3$). **j**, Schematics of PDX model treatment and tumour progression. MRD, minimal residual disease; RES, resistance. Parts of this figure were created in BioRender. **k**,**l**, Representative images (**k**, scale bars, 20 µm) of BDH2, MITF and RAB7 multiplex costaining of the primary tumour from a melanoma PDX model, and quantification (**l**) of BDH2 correlation with MITF and RAB7 expression in five PDX tumours. **m**,**n**, Representative images (**m**, scale bars, 20 µm) of BDH2, MITF and RAB7 multiplex costaining of the primary tumour from a melanoma MEL006 PDX model[21] at different drug-resistant stages in response to D/T treatment and quantification (**n**) of the percentage of different populations on the basis of their expression levels. For western blots, β-actin was used as a loading control. Data are presented as mean ± s.e.m. Statistical significance was assessed by two-tailed one-sample *t*-test (**h**,**i**). *$P < 0.05$.

Table 3). In line with their RNA levels, the protein expression levels of several subunits of the lysosomal proton pump v-ATPase were downregulated in MES cells (Fig. 3c), Mitoferrin-1 and CD44 were upregulated (Fig. 3d,e), whereas the levels of DMT1 and TRPML1 were unchanged (Extended Data Fig. 5b,c). Despite the increased expression of Mitoferrin-1, mitochondrial iron import remained defective in MES cells (Fig. 1c,d and Extended Data Fig. 1h,i), pointing to an inadequate Fe(II) transfer through the outer mitochondrial membrane.

Of note, the top DE iron-related gene significantly downregulated in MES cells was *BDH2*, a member of the family of 3-hydroxybutyrate dehydrogenase 2 enzymes[58] (Fig. 3b, Extended Data Fig. 5a and Supplementary Table 3). This enzyme drew our attention because BDH2 has been described as the functional mammalian homologue of the bacterial EntA protein involved in the synthesis of 2,3-dihydroxybenzoic acid (DHBA), the iron-binding moiety of the bacterial enterobactin[59]. In mammalian cells, BDH2 produces 2,5-DHBA, which works as a siderophore to import iron into the mitochondria[59]. In line with RNA expression data, BDH2 protein levels were high in MEL cells (Fig. 3f,g) but were either low or undetectable in MES cells (Fig. 3f,g). Silencing BDH2 in MEL cells (Fig. 3h) reduced the levels of 2,5-DHBA as measured by liquid chromatography–mass spectrometry (LC–MS) (Fig. 3i), thus confirming the role of BDH2 in 2,5-DHBA production.

To explore *BDH2* expression profile in an in vivo disease context, we analysed a single-cell RNA-seq (scRNA-seq) dataset from melanoma patient-derived xenografts (PDXs), which describes the dynamics of the melanoma cell-state transition in response to treatment with inhibitors of $BRAF^{V600E}$ and $BRAF^{V600K}$ ($BRAF^{V600E/K}$) (dabrafenib) and MEK (trametinib) (D/T)[21] (Fig. 3j). *BDH2* expression was higher in the $MITF^{hi}$ MEL melanoma lineages than in the $MITF^{lo}$ MES drug-resistant melanoma phenotype, which includes neural crest stem cells (NCSC) and invasive states with enhanced metastatic potential (Extended Data Fig. 5d).

Given this tight correlation between *MITF* and *BDH2*, and the reported downregulation of *RAB7* levels in MES cells[36], we performed multiplexed immunohistochemistry in PDX models (MEL006, MEL015) derived from patients with $BRAF^{V600E/K}$ mutant melanoma[21] to evaluate their coexpression in baseline conditions and under therapeutic pressure. MITF expression was heterogeneous in treatment-naive (t0) lesions (Fig. 3k), and BDH2 positively correlated with MITF and RAB7 levels (Fig. 3k,l). In response to D/T treatment, the $MITF^{hi}RAB7^{hi}BDH2^{hi}$ population decreased in drug-tolerant cells, with the emergence of the minimal residual disease (MRD) phase, and reappeared at the onset of resistance (RES) (Fig. 3m,n and Extended Data Fig. 5e). This is consistent with the importance of reversible phenotype switching as a driver of drug tolerance and resistance, previously reported in these models[18,20,21].

We next tested whether MITF could directly regulate the transcription of this iron-modulating enzyme. Chromatin immunoprecipitation and sequencing (ChIP–seq) analysis indicated the presence of MITF binding sites upstream of the *BDH2* gene (Extended Data Fig. 5f), suggesting that MITF can contribute to the transcriptional regulation of *BDH2*, which is consistent with the coexpression analysis (Fig. 3k–n and Extended Data Fig. 5d,e). MITF depletion in MEL cells reduced, but did not abolish, BDH2 protein levels (Extended Data Fig. 5g–j), indicating that, besides MITF, other transcription factors or post-transcriptional mechanisms contribute to maintaining BDH2 expression in MEL cells.

Together these data indicate that, as MITF levels and activity decrease during the phenotype switching, the expression of *BDH2* and its product, the siderophore 2,5-DHBA, are downregulated.

Production of 2,5-DHBA by BDH2 is required for inter-organelle iron transport

MES cells exhibited elevated levels of the mitochondrial inner membrane iron importer Mitoferrin-1, suggesting a potential for importing iron into the mitochondrial matrix. However, despite this upregulation, MES cells also exhibited defective mitochondrial iron levels and metabolism. We therefore hypothesized that, in these cells, the reduction in BDH2 and its product 2,5-DBHA could underlie this deficiency, limiting effective mitochondrial iron import even in the presence of elevated expression of Mitoferrin-1 (or SLC25A37).

Silencing (Fig. 4a) or knocking out (by CRISPR/Cas9) *BDH2* (Extended Data Fig. 6e) in MEL cells led to a decrease in mitochondrial iron levels (Fig. 4b,c and Extended Data Fig. 6a,b,f,g), and a corresponding accumulation in lysosomal iron (Fig. 4d,e and Extended Data Fig. 6c,d,h,i). In line with this, increasing the expression of BDH2 in MES cells (Fig. 4f) induced the opposite organellar iron redistribution effect (Fig. 4g–j). Likewise, supplementing 2,5-DHBA to MES cells phenocopied the effects of the *BDH2* overexpression in a dose-dependent manner (Fig. 4k–n and Extended Data Fig. 6j–q). In MES cells, elevated BDH2 levels or supplementation with 2,5-DHBA was associated with a modest (although not statistically significant) increase in OCR (Fig. 4o,p and Extended Data Fig. 7a,b) and a trend toward an increase in the iron-dependent OXPHOS complexes (Extended Data Fig. 7c–f). The partial restoration of mitochondrial bioenergetics by the BDH2–2,5-DHBA axis in MES cells under these settings could involve inefficient Ca^{2+} import to the mitochondria owing to their reduced VDAC levels (Extended Data Fig. 7k,l) and/or to the absence of microenvironmental factors influencing metabolic plasticity[32].

Of note, neither BDH2 expression nor 2,5-DHBA treatment significantly altered the IRP2 protein levels (Extended Data Fig. 7g–j). Because IRP2 is an iron-responsive regulator of cytosolic iron levels, these data suggest that the BDH2–2,5-DHBA axis could specifically regulate lysosomal–mitochondrial Fe(II) redistribution, rather than affecting the overall levels of cytosolic iron.

Collectively, these data highlight a major role of the BDH2–2,5-DHBA axis in maintaining lysosome-to-mitochondria iron redistribution and, consequently, mitochondrial respiration in $MITF^{hi}$ MEL cells.

BDH2 localizes at the mitochondria–lysosome contacts to regulate lysosomal pH and MLC formation

The generation of 2,5-DHBA by BDH2 has been shown to favour iron import in the mitochondria of mammalian cells[59]. Although BDH2 is

Fig. 4 | Production of 2,5-DHBA by BDH2 is required for inter-organelle iron transport. a, Representative western blot of BDH2 in $M229^{MEL}$ shCTR and sh*BDH2* cells ($n = 2$). **b**,**c**, Representative images (**b**, scale bars, 10 µm) and quantification of mitochondrial iron levels using Mito-FerroGreen MFI per cell (**c**) in $M229^{MEL}$ shCTR ($n = 30$) and sh*BDH2* ($n = 30$) cells (three independent experiments). **d**,**e**, Representative images (**d**, scale bar: 10 µm) and quantification of lysosomal iron using FerroOrange MFI per cell within the lysosomal mask (**e**) in $M229^{MEL}$ shCTR ($n = 30$) and shBDH2 ($n = 30$) cells (three independent experiments). **f**, Representative western blot of BDH2 in $M229R^{MES}$ EV and BDH2 cells ($n = 3$). **g**,**h**, Representative images (**g**, scale bars, 10 µm) and quantification of mitochondrial iron using Mito-FerroGreen MFI per cell (**h**) in $M229R^{MES}$ EV ($n = 30$) and BDH2 ($n = 30$) cells (three independent experiments). **i**,**j**, Representative images (**i**, scale bar: 10 µm) and quantification of lysosomal iron using FerroOrange MFI per cell within the lysosomal mask (**j**) in $M229R^{MES}$ EV ($n = 30$) and BDH2 ($n = 30$) cells (three independent experiments). **k**,**l**, Representative images (**k**, scale bars, 10 µm) and quantification of mitochondrial iron using Mito-FerroGreen MFI per cell (**l**) in $M229R^{MES}$ cells that were untreated ($n = 60$), treated with FAS ($n = 60$) or treated with 1 mM ($n = 60$) or 5 mM ($n = 50$) 2,5-DHBA (three independent experiments). **m**,**n**, Representative images (**m**, scale bars, 10 µm) and quantification of lysosomal iron using FerroOrange MFI per cell within the lysosomal mask (**n**) in $M229R^{MES}$ cells that were untreated ($n = 30$), treated with FAS ($n = 30$) or treated with 1 mM ($n = 30$) or 5 mM ($n = 31$) 2,5-DHBA (three independent experiments). **o**, OCR of EV and BDH2 $M229R^{MES}$ cells ($n = 3$). **p**, OCR of $M229R^{MES}$ cells that were untreated or treated with FAS and 2,5-DHBA ($n = 5$). For western blots, β-actin was used as a loading control. Data are presented as mean ± s.e.m. Statistical significance was assessed by unpaired two-tailed Student's *t*-test (**c**,**e**,**h**,**j**) or one-way ANOVA (**l**,**n**). Magnified images of the boxed areas are shown for detail (**b**, **d**, **g**, **i**, **k** and **m**).

https://doi.org/10.1038/s42255-025-01352-4

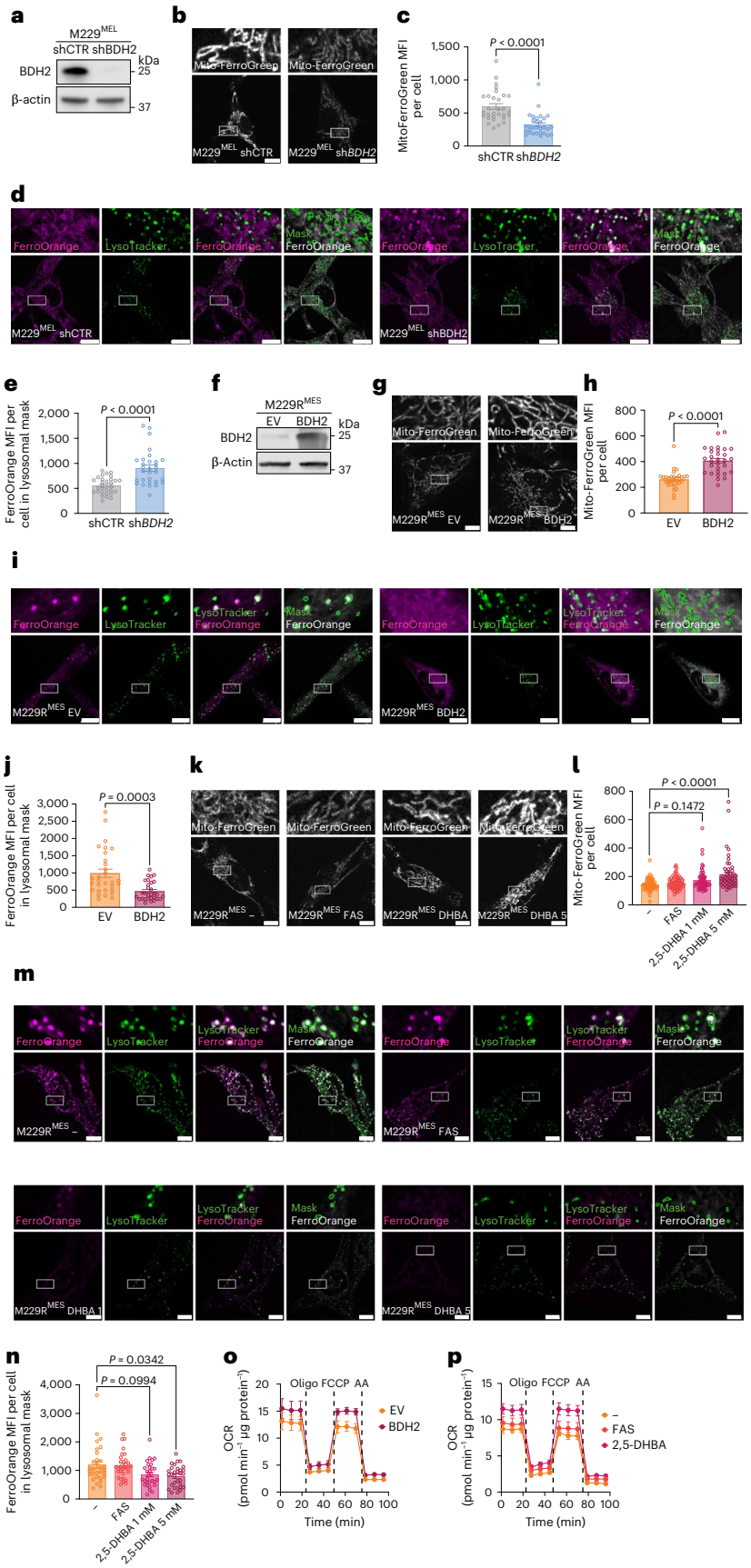

considered to be mainly a cytosolic enzyme[59], in light of our findings, we hypothesized that mitochondrial localization of BDH2 could facilitate more efficient capture of lysosomal iron and its transport in the mitochondria.

We used SIM to assess the colocalization of BDH2 with the outer mitochondrial membrane (OMM) marker TOM20 in different melanoma cell lines with defined MEL and MES phenotypes. After normalizing for the overall differential expression of BDH2 in these cells, we observed a substantial association of BDH2 with the OMM in several MEL cell lines (Fig. 5a,b and Extended Data Fig. 8a,b). By contrast, only a minor fraction of BDH2 colocalized with TOM20 in MES cells (Fig. 5a,b and Extended Data Fig. 8a,b). To image MLCs and evaluate the presence of BDH2 in these membrane subdomains, we performed SIM on cells costained with antibodies against LAMP1, TOM20 and BDH2. In MEL cells, a large fraction of TOM20–LAMP1 double-positive areas contained BDH2, suggesting that it was present at mitochondria–lysosome contacts (Fig. 5c,d). This overlap was significantly lower in MES cells (Fig. 5d).

Because increasing BDH2 expression in MES cells restored homeostatic iron redistribution between lysosomes and mitochondria, we sought to gain more mechanistic insights into the potential effects of the BDH2–2,5-DHBA axis on lysosomal pH. Silencing *BDH2* in MEL cells resulted in alkalinization of the lysosomal pH (Fig. 5e). By contrast, increasing the levels of BDH2 or supplementing 2,5-DHBA effectively reduced lysosomal pH of MES cells (Fig. 5f,g) and consistently restored their degradative capacity (Extended Data Fig. 8c,d), despite v-ATPase protein levels remaining unchanged (Extended Data Fig. 8e–h).

Our findings that lysosomal re-acidification in MES cells promoted the formation of short MLCs (Fig. 2s,t), and that *BDH2* expression or 2,5-DHBA supplementation rescued lysosomal pH (Fig. 5e–g), prompted us to test whether the BDH2–2,5-DHBA axis modulates short MLC formation. In accordance with this, the expression of *BDH2* or treatment with 2,5-DHBA led to an increase in short MLCs in MES cells (Fig. 5h–k), whereas *BDH2* silencing had the opposite effect in MEL cells (Fig. 5l,m).

To determine whether *RAB7* expression is required for recruitment of BDH2 to mitochondria, we expressed the constitutively active RAB7-Q67L mutant or the dominant negative RAB7-T22N mutant and performed colocalization studies of TOM20 and BDH2. Strengthening short MLCs in MES cells with RAB7-Q67L (Fig. 2f,g), or further weakening them with RAB7-T22N (Fig. 2f,g), did not change BDH2 localization in these cells (Extended Data Fig. 8i,j), suggesting that BDH2 is recruited to the mitochondria independently of RAB7 activity. This likely explains why restoring RAB7 levels or activity in MES cells in the absence of a functional BDH2–2,5-DHBA axis is not sufficient to fully rescue the defects in iron transfer at the MLCs (Extended Data Fig. 3e–h) and to rectify the lysosomal pH (Extended Data Fig. 4f).

The presence of BDH2 at the mitochondrial side of the MLCs, and its biological effect on iron redistribution, raised the question of whether its product 2,5-DHBA could favour the mobilization of iron from lysosomes to mitochondria.

Previous studies using different cellular settings have raised doubts about the ability of 2,5-DHBA to tightly bind iron and function as a siderophore[60–62]. However, using nuclear magnetic resonance (NMR) spectroscopy and visual inspection, we found that 2,5-DHBA binds to both Fe(III) and Fe(II) (Extended Data Fig. 8k–n). The interaction of 2,5-DHBA with Fe(III) was stable under acidic conditions (as found in lysosomes), whereas complexes with Fe(II) and Fe(III) dissociated at higher pH (>8) (Extended Data Fig. 8k–n). This finding supports the established role of 2,5-DHBA as a siderophore[59] and suggests that 2,5-DHBA can bind iron at the acidic pH of the lysosome and then release it in a more alkaline environment, similar to that found in the mitochondrial matrix[63].

Next, we conducted in-cell labelling of an alkyne-containing synthetic analogue of 2,5-DHBA, which we named cDHBA, by means of click chemistry (Extended Data Fig. 8o). We used the same concentration that corrected mitochondrial iron uptake and restored functional MLCs in MES cells (Extended Data Fig. 8o–q). cDHBA fluorescence localized in the cytosol, nucleus, and proximal to the mitochondrial network (Extended Data Fig. 8o–q), further suggesting a role for 2,5-DHBA in mediating internalization of iron in mitochondria.

We investigated whether efficient mitochondrial OXPHOS elicited by Fe(II) transfer to mitochondria through the BDH2–2,5-DHBA axis at MLCs could favour lysosomal acidification by supporting the lysosomal V-ATPase activity that utilizes ATP hydrolysis to pump protons into the lysosomal lumen (Fig. 5n). Acute inhibition of the mitochondrial complex V (ATP synthase) by oligomycin caused an alkalinization of the lysosomal pH (Fig. 5o) and curbed short MLC formation in MEL cells (Fig. 5p,q).

Of note, blocking mitochondrial iron import by knocking out (by CRISPR/Cas9) *SLC25A37* (encoding Mitoferrin-1) (Fig. 5r) counteracted the rescue effects of BDH2–2,5-DHBA on mitochondrial iron (Fig. 5s,t

Fig. 5 | BDH2 localizes at the mitochondria–lysosome contacts to regulate lysosomal pH and MLC formation. a,**b**, Representative SIM images (**a**, scale bars, 10 µm) and quantification of BDH2 intracellular localization (**b**) in M229^{MEL} ($n = 29$) and M229R^{MES} ($n = 24$) cells (three independent experiments). **c**,**d**, Representative SIM images (**c**, scale bar, 10 µm) and quantification of the presence of BDH2 at the MLCs (**d**) in M229^{MEL} ($n = 45$) and M229R^{MES} ($n = 40$) cells (three independent experiments). **e**, Relative lysosomal pH levels (LysoSensor MFI) of M229^{MEL} shBDH2 versus shCTR cells ($n = 5$). **f**, Relative lysosomal pH levels (LysoSensor MFI) of M229R^{MES} BDH2 versus EV cells ($n = 3$). **g**, Relative lysosomal pH levels (LysoSensor MFI) of M229R^{MES} 2,5-DHBA-treated versus untreated cells ($n = 4$). **h**,**i**, Representative images (**h**, scale bars, 10 µm) and quantification of short MLCs per cell (**i**) in M229R^{MES} EV ($n = 30$) and BDH2 ($n = 30$) cells (three independent experiments). **j**,**k**, Representative images (**j**, scale bars, 10 µm) and quantification of short MLCs per cell (**k**) in M229R^{MES} untreated ($n = 29$) and 2,5-DHBA-treated ($n = 28$) cells (three independent experiments). **l**,**m**, Representative images (**l**, scale bars, 10 µm) and quantification of short MLCs per cell (**m**) in M229^{MEL} shCTR ($n = 18$) and sh*BDH2* ($n = 23$) cells (two independent experiments). **n**, Schematics of the hypothesized mechanism through which ATP production by the mitochondrial OXPHOS complex V (ATP synthase) stimulates the activity of the lysosomal ATP-dependent proton pump (v-ATPase). Parts of this figure were created in BioRender. **o**, Relative lysosomal pH levels (LysoSensor MFI) of M229^{MEL} oligomycin-treated (oligo) versus untreated cells ($n = 5$). **p**,**q**, Representative images (**p**, scale bars, 10 µm) and quantification of short MLCs per cell (**q**) in M229^{MEL} untreated ($n = 30$) and oligomycin-treated (oligo, $n = 29$) cells (four independent experiments). **r**, Representative western blot of Mitoferrin-1 in M229R^{MES} sgCTR or sg*Mfrn1* cells ($n = 2$) (*Mfrn1* encodes Mitoferrin-1). **s**,**t**, Representative images (**s**, scale bars, 10 µm) and quantification of mitochondrial iron levels using Mito-FerroGreen MFI per cell (**t**) in M229R^{MES} sgCTR basal ($n = 30$) or 2,5-DHBA-treated ($n = 30$) cells and sg*Mfrn1* basal ($n = 30$) or 2,5-DHBA-treated ($n = 30$) cells (three independent experiments) **u**, Relative lysosomal pH levels (LysoSensor MFI) of M229R^{MES} sgCTR basal (−) or 2,5-DHBA-treated cells and sg*Mfrn1* basal or 2,5-DHBA-treated cells ($n = 5$). **v**,**w**, Representative images (**v**, scale bars, 10 µm) and quantification of short MLCs per cell (**w**) in M229R^{MES} sgCTR basal ($n = 24$) or 2,5-DHBA-treated ($n = 26$) cells and sg*Mfrn1* basal ($n = 26$) or 2,5-DHBA-treated ($n = 28$) cells (two independent experiments). **x**, Schematics of the molecular mechanism: in an MLC, BDH2 on the mitochondrial outer membrane produces 2,5-DHBA, which binds to Fe(II), enabling its internalization in mitochondria through the inner mitochondrial membrane transporter Mitoferrin-1; the consequent increase in mitochondrial respiration enhances the production of ATP by the ATP synthase, in turn favouring the activity of the lysosomal v-ATPase, which is responsible for lysosomal lumen acidification; finally, lysosomal acidity sustains the formation of MLCs, further promoting iron transfer from the lysosomes to mitochondria. Parts of this figure were created in BioRender. For western blots, β-actin was used as a loading control. Data are presented as the mean ± s.e.m. Statistical significance was assessed by unpaired two-tailed Student's *t*-test (**b**,**d**,**i**,**k**,**m**,**q**), two-tailed one-sample *t*-test (**e**,**f**,**g**,**o**,**u**) or one-way ANOVA (**t**,**w**). Magnified images of the boxed areas are shown for detail (**a** and **s**).

https://doi.org/10.1038/s42255-025-01352-4

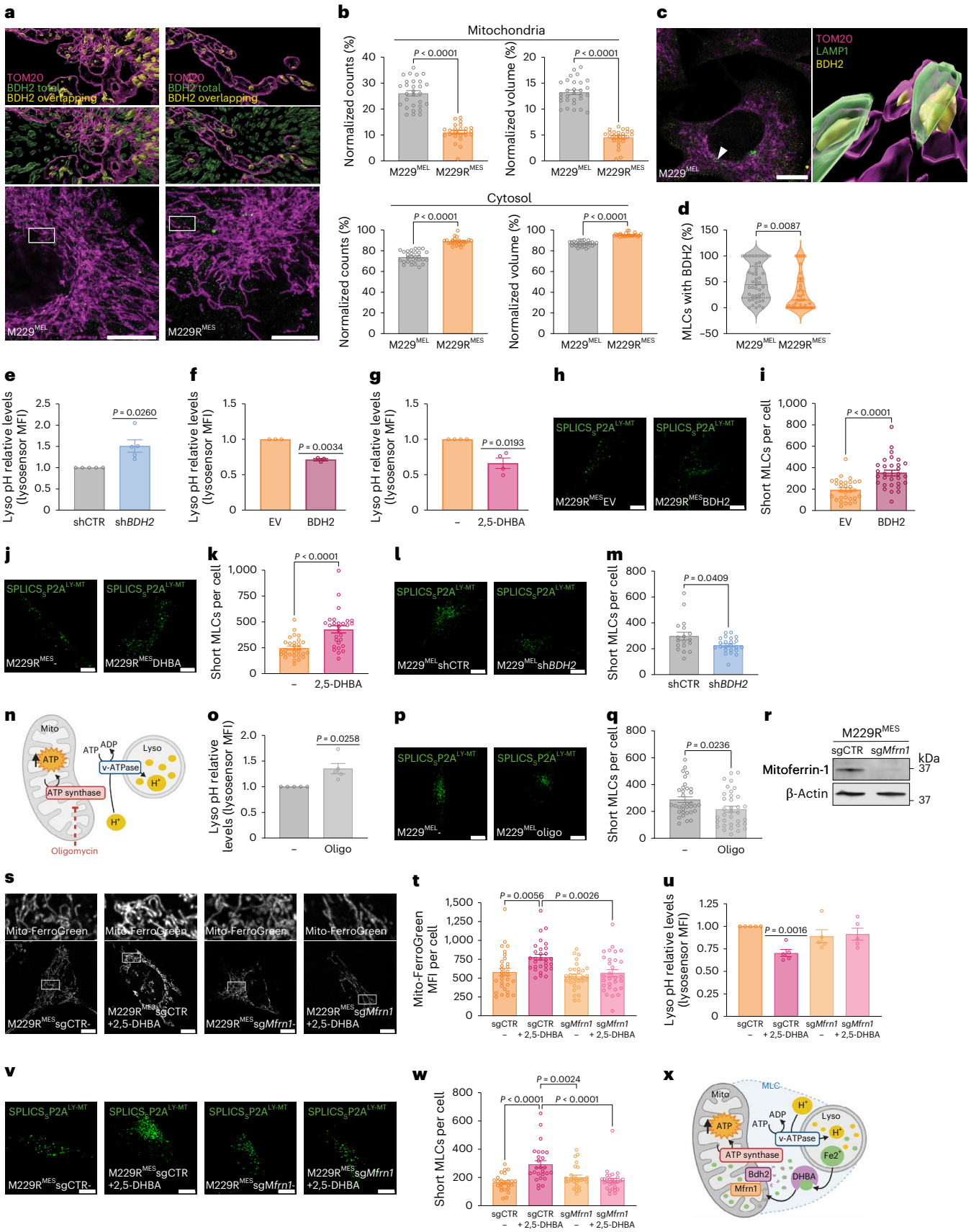

https://doi.org/10.1038/s42255-025-01352-4

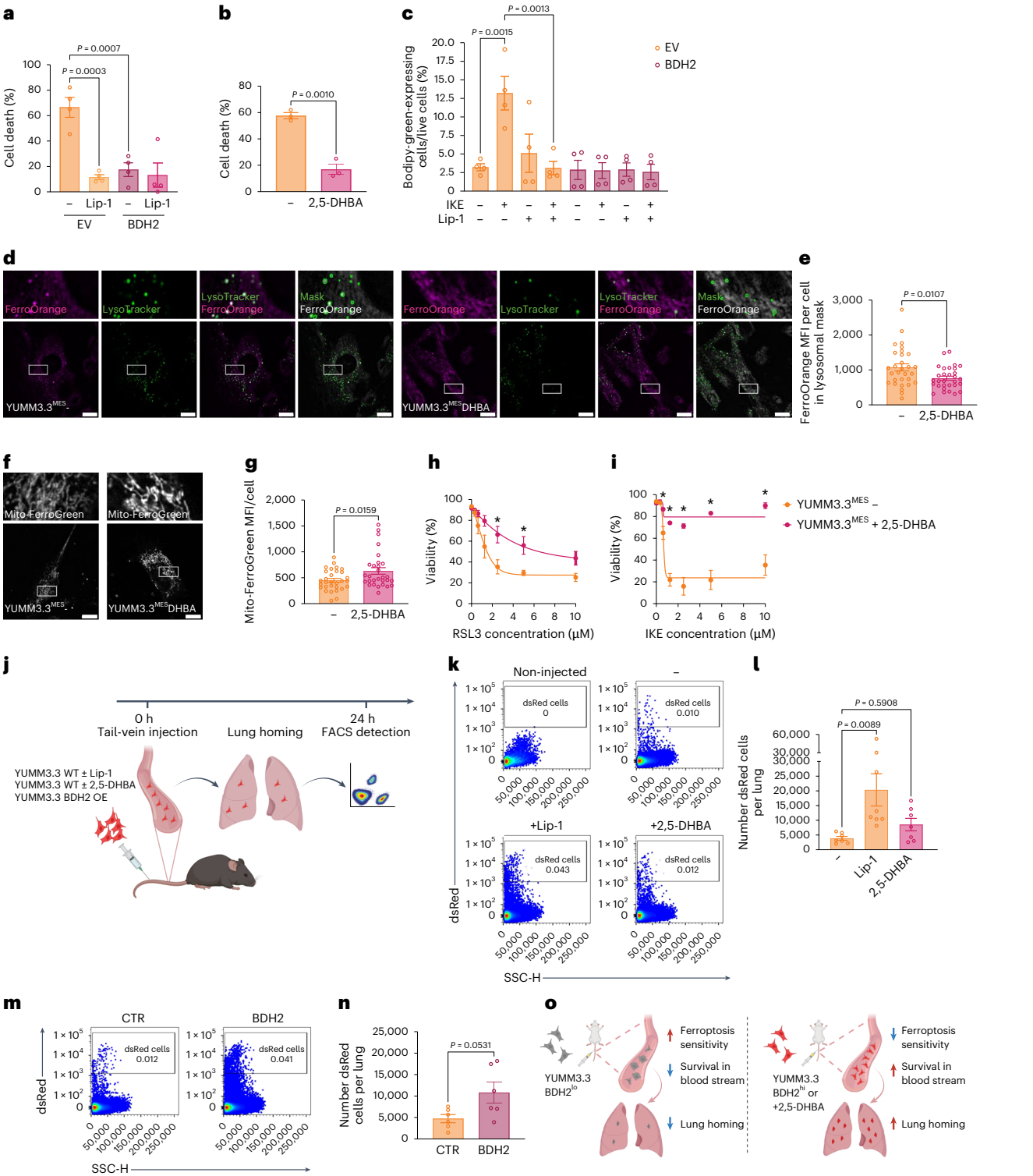

Fig. 6 | The BDH2–2,5-DHBA axis protects MES cells against ferroptosis in vitro and in the bloodstream. a, Cell death of M229R^{MES} EV and BDH2 spheroids upon IKE treatment alone (−) and in combination with Liproxstatin-1 (Lip-1) ($n = 4$). **b**, Cell death of M229R^{MES} untreated and 2,5-DHBA-treated spheroids upon IKE treatment ($n = 3$). **c**, Levels of lipid peroxidation, as determined by the Bodipy C11 assay, in M229R^{MES} spheroids upon IKE treatment alone and in combination with Lip-1 ($n = 4$). **d**,**e**, Representative images (**d**, scale bars, 10 µm) and quantification of lysosomal iron using FerroOrange MFI per cell in the lysosomal mask (**e**) in M229R^{MES} untreated ($n = 30$) and 2,5-DHBA-treated ($n = 30$) cells (three independent experiments). **f**,**g**, Representative images (**f**, scale bars, 10 µm) and quantification of mitochondrial iron using Mito-FerroGreen MFI per cell (**g**) in M229R^{MES} untreated ($n = 30$) and 2,5-DHBA-treated ($n = 29$) cells (three independent experiments). **h**,**i**, Percentage of viability of YUMM3.3^{MES} untreated and 2,5-DHBA-treated cells upon treatment with increasing doses of RSL3 (**h**) and IKE (**i**). **j**, Schematic of the in vivo experiment. Parts of this figure were created in BioRender. **k**,**l**, Flow cytometry gating strategy (**k**) and quantification (**l**) of live YUMM3.3^{MES} dsRed cells detected in the lungs 24 h after tail-vein injection and after treatment with Lip-1 ($n = 8$), 2,5-DHBA ($n = 7$) or nothing ($n = 7$) for 24 h. **m**,**n**, Flow cytometry gating strategy (**m**) and quantification (**n**) of live YUMM3.3^{MES} dsRed cells CTR ($n = 6$) and BDH2 ($n = 6$) detected in the lungs 24 h following tail-vein injection. **o**, Schematic of the in vivo mechanism. Parts of this figure were created in BioRender. Data are presented as mean ± s.e.m. Statistical significance was assessed by one-way ANOVA (**a**,**c**,**l**), and unpaired two-tailed Student's *t*-test (**b**,**e**,**g**–**i**,**n**). Magnified images of the boxed areas are shown for detail (**d** and **f**). *$P < 0.05$.

and Extended Data Fig. 8r,s), lysosomal pH (Fig. 5u) and MLCs (Fig. 5v,w) in MES cells.

Together, these results suggest that the effects exerted by the BDH2–2,5-DHBA axis on mitochondrial iron and energy metabolism favour the maintenance of the acidic lysosomal pH, which is required for MLC formation (Fig. 5x).

The BDH2–2,5-DHBA axis protects MES cells against ferroptosis in vitro and in the bloodstream

We next asked how inter-organellar iron remodelling through the BDH2–2,5-DHBA axis influences the ferroptosis sensitivity of MES cells, using both two-dimensional (2D) cultures and three-dimensional (3D) spheroids, which better recapitulate the architecture and metabolic characteristics of tumours[64–67]. We first confirmed that the panel of MES cell lines used in our study succumbed to bona fide ferroptosis following exposure to the canonical ferroptosis inducers (FINs), (1*S*,3*R*)-RSL3 (RSL3) and imidazole-ketone erastin (IKE) (Extended Data Fig. 9a,c). By contrast, MEL cells were resistant to FINs (Extended Data Fig. 9a,c). Ferroptosis was validated by the selective inhibition of cell death by the iron chelator DFO, and the ferroptosis inhibitor ferrostatin-1 (Ferr-1), but not by apoptosis or necroptosis inhibitors (Extended Data Fig. 9b,d).

Expression of *BDH2* in MES cells, or supplementation of 2,5-DHBA to the 3D spheroids, mitigated lipid peroxidation and ferroptosis as compared with parental cells (empty vector (EV) or untreated, respectively) (Fig. 6a–c). Similar protective effects were observed in 2D cultures (Extended Data Fig. 9e–g). Notably, lowering the lysosomal pH by providing acNPs to MES cells was partially protective (Extended Data Fig. 9h), thus connecting lysosomal pH control of the iron pool to ferroptosis vulnerability.

2,5-DHBA has been suggested to be an inhibitor of arachidonate 15-lipoxygenase (LOX) enzyme activity[68], raising the possibility that this could contribute to the ferroptosis-mitigating effect of the siderophore. However, at concentrations that effectively block ferroptosis, 2,5-DHBA did not affect LOX activity in basal conditions or upon stimulation with its substrate, iron(II) (provided as FAS) (Extended Data Fig. 9i). These findings rule out that the ferroptosis-protecting effects of this metabolite were mediated by the potential off-target inhibition of LOX enzymes.

We then tested whether BDH2, or its product 2,5-DHBA, influenced cell death responses induced by clinically relevant anti-melanoma therapies. Modulating *BDH2* expression, either by downregulating it in MEL cells or upregulating it in MES cells, did not change cell responses to apoptosis induced by vemurafenib or D/T (Extended Data Fig. 9j–m). Similarly, *BDH2* expression did not protect MES cells from cell death induced by H_2O_2 (Extended Data Fig. 9n). Melanoma cells are inherently resistant to necroptosis owing to the low expression of essential necroptotic effectors, such as RIPK3 or MLKL[69,70] (Extended Data Fig. 9o), suggesting that the effects of the BDH2–2,5-DHBA axis are specific to iron-mediated lipid peroxidation and do not extend to D/T-induced apoptosis or broader oxidative stress insult in our settings.

To determine whether the BDH2-dependent regulation of iron inter-organelle compartmentalization is evolutionarily conserved, we tested the effects of BDH2 and 2,5-DHBA against ferroptosis in the murine melanoma cell line YUMM3.3. This model was selected to explore the functional effects of the BDH2–2,5-DHBA axis for several reasons: (1) similar to human MES melanoma cells, it expresses low or undetectable levels of BDH2 (Extended Data Fig. 9p); (2) it exhibits the lysosomal-rich and ferroptosis-sensitive iron phenotype (Fig. 6d–i and Extended Data Fig. 9q) that (3) is mitigated by the expression of *BDH2* or by supplementing the cells with 2,5-DHBA (Fig. 6d–i and Extended Data Fig. 9q). Furthermore, YUMM3.3 cells have been shown to be particularly vulnerable to ferroptosis when disseminating through the iron-rich bloodstream while being protected by the lymph environment[71].

We then explored whether rescuing *BDH2* expression in YUMM3.3 cells or pretreating them with the siderophore 2,5-DHBA altered the seeding ability of MES cells to secondary sites, such as the lungs, during the circulatory phase of the metastatic cascade (Fig. 6j). Once surviving cancer cells enter the hostile environment of the blood flow, they reach the secondary site within a few hours[72], so we explored the lung homing potential of MES cells 24 h after tail-vein injection (Fig. 6j).

YUMM3.3 cells demonstrated poor seeding potential (Fig. 6k–n and Extended Data Fig. 9r). Pretreatment with the ferroptosis inhibitor Lip-1 significantly increased their lung-homing capacity (Fig. 6k,l and Extended Data Fig. 9r), consistent with the role of ferroptosis as a mechanism contributing to the death of blood-circulating cancer cells[71]. YUMM3.3 cells treated with 2,5-DHBA showed a trend toward increased seeding capacity relative to their corresponding control cells (Fig. 6k,l and Extended Data Fig. 9r). Notably, elevated BDH2 levels in these MES cells heightened their lung seeding competence (Fig. 6m,n and Extended Data Fig. 9r).

Together, these data indicate that the BDH2–2,5-DHBA axis shields MES cells from ferroptosis into the haematogenous circulation, thereby enhancing their seeding ability to a secondary organ (Fig. 6o).

Discussion

Our work provides multiple lines of evidence supporting an unprecedented mechanism that connects BDH2 regulation of iron inter-organellar distribution with lysosomal pH and mitochondrial metabolism. This model deploys a system conserved from bacteria through humans that relies on BDH2, the mammalian homologue of the bacteria EntA, and its product, the siderophore 2,5-DHBA[59]. Just as bacteria exploit 2,3-DHBA secretion to import iron for their growth, this BDH2-regulated cell-autonomous mechanism represents an evolutionarily conserved strategy for trafficing endocytosis-acquired extracellular iron from the lysosomes to the mitochondria, thereby fostering the metabolism of actively proliferating cancer cells. We unveil that, to ensure the effective transfer of Fe(II) to the mitochondria, BDH2 is strategically located at MLCs and fosters a positive feedforward mechanism that integrates mitochondria bioenergetics with the maintenance of lysosomal pH and functional organelle communication. As a consequence of the dedifferentiation programme driven by the loss of MITF, the BDH2–2,5-DHBA axis is compromised, causing retention of Fe(II) in the lysosomes and priming mesenchymal-like melanoma cells for ferroptosis.

Our findings indicate that the transition from the $MITF^{hi}$ cell state to the $MITF^{lo}$ drug-tolerant MES phenotype is accompanied by the redistribution of redox-active Fe(II) between mitochondria and lysosomes, key organelles involved in the utilization and storage of iron, respectively[1]. By tracking the spatiotemporal dynamics of inter-organelle iron transfer under homeostasis, we revealed that this requires efficient MLC formation. Remarkably, our data further suggest that MLCs exhibit significant heterogeneity in intermembrane distances and tethering durations, which could reflect diversity in their functional roles. For example, narrow contacts are associated with calcium transfer and mitochondrial dynamics[37]. Our findings support the notion that iron transfer requires similar short-distance contacts between organelles. However, whether metal transfer engages the simultaneous contact of lysosomes with multiple mitochondria and/or is influenced by contact duration remains to be investigated.

Notwithstanding, our work strongly supports the idea that the BDH2–2,5-DHBA axis is both necessary and sufficient to rescue the acidic lysosomal pH, which is essential for MLC formation and iron trafficking to the mitochondria. By contrast, restoring RAB7 levels or GTP hydrolysing activity in MES cells recovers MLCs but does not acidify the lysosomal pH or correct mitochondrial OXPHOS. The crucial role of the BDH2–2,5-DHBA axis is consistent with our 3D SIM imaging, which unveils a pool of BDH2 at MLCs. A prior study identified BDH2 as the mammalian homologue of the bacterial EntA protein that catalyses

the production of 2,3-DHBA during enterobactin biosynthesis[59]. Siderophore depletion in cells or zebrafish embryos blunted haem synthesis and mitochondrial iron import. Of note, the same study suggested that iron is imported into the mitochondria as an iron–siderophore complex[59].

Hence, the recruitment of BDH2 to the mitochondrial side of MLCs could enable the local production of 2,5-DHBA in these subdomains of membrane interaction, allowing efficient binding of iron and subsequent transport and release of Fe(II) in the mitochondria in a pH-regulated manner. It remains to be determined whether the effects of the BDH2–2,5-DHBA axis involve other mitochondria-tethering proteins[73,74] and work in concert with mitochondrial carriers enabling iron transport. Also, we cannot rule out further roles for cytosolic BDH2, which might contribute to the observed phenotype. Because of its ability to convert 3-hydroxybutyrate into acetoacetate, BDH2 could further support mitochondrial TCA by providing ketone bodies[75]. However, although *Bdh2*$^{-/-}$ mice display anaemia and iron overload in tissue, they do not exhibit defects in ketone-body metabolism in vivo[75]. This suggests that a major role for BDH2 is to control iron metabolism both at the cellular and systemic levels.

Notwithstanding, our study highlights the role of mitochondrial bioenergetics, facilitated by the BDH2-regulated mitochondrial iron transfer, in maintaining the acidic lysosomal pH. This aligns with the findings that inhibition of complex V by oligomycin, which impairs ATP production, or Mitoferrin-1 deletion, which prevents the uptake of mitochondrial iron, similarly cause alkalinization of the lysosomes and inhibition of MLC tethering dynamics.

Of note, the activity of the lysosomal iron transporters DMT1 and TRPML1 is pH-dependent[45,76,77], further connecting the relevance of the feedback loop driven by the BDH2–2,5-DHBA axis for inter-organelle iron trafficking. In support of our model, a recent work indicated that DMT1 silencing, by impairing mitochondrial iron transfer, reduced mitochondrial bioenergetics and heightened the invasive fitness of triple-negative breast cancer cells[78].

Silencing *MITF* in MEL cells leads to a concomitant reduction of *BDH2* levels and partially phenocopies the loss of BDH2. This suggests that *BDH2* expression is regulated by MITF, a possibility that is supported by our ChIP–seq analysis. Furthermore, loss of MITF is accompanied by impairment in mitochondrial OXPHOS and the downregulation of *BDH2* expression, along with a primary set of gene products functionally linked to the maintenance of the acidic lysosomal pH and iron transport.

In accordance with this, in samples from melanoma patients, *BDH2* is expressed in the MITF^{hi}RAB7^{hi} cell population and is co-downregulated at the emergence of MRD triggered by targeted therapy[21]. This suggests a temporal, dynamic coregulation between *MITF* and *BDH2* that remains to be fully deciphered. Our study suggests that, during targeted therapy, the concomitant downregulation of BDH2 and RAB7 and the consequent lysosomal iron compartmentalization could selectively sensitize the MRD population of MES/drug-tolerant cells to ferroptosis inducers. The avidity of the drug-tolerant/MES state for the import of iron through endocytosis[11,13,17], along with their elevated content of polyunsaturated phospholipids in membranes[79–81], exposes these cells to a 'lysosomal vulnerability' that primes the MES phenotype for ferroptosis. This hypothesis is consistent with recent studies harnessing the higher iron load of metastatic cancer cells to promote ferroptosis by activating lysosomal iron[13].

Although our findings indicate that the loss of BDH2 expression in MES cells leads to susceptibility to ferroptosis both in vitro and in vivo, BDH2 has also been reported to modulate apoptosis and autophagy in other solid tumours through various mechanisms[82,83]. Although these studies did not examine the impact on cancer cells' phenotype, they suggest that the role of BDH2 in cancer could be context-specific, warranting further investigations into the therapeutic benefits of BDH2 modulation in melanoma.

In summary, our data identify BDH2 as an essential effector of MLCs and iron compartmentalization, which mechanistically links mitochondrial metabolism and lysosomal function to the ferroptosis vulnerability of melanoma cells. We provide evidence that rescuing the BDH2–2,5-DHBA axis in human or murine mesenchymal-like cells curbs their vulnerability to ferroptosis in vitro and during metastatic seeding in vivo. After surviving in the circulation, to form metastasis cancer cells must be able to colonize and thrive within the metastatic environment. Whether fluctuations in BDH2 levels and the resulting shift in lysosome-to-mitochondria iron transfer constitute an adaptive mechanism endowing melanoma cells with the metabolic plasticity required for their survival and proliferation in the metastatic niche, remains to be investigated. Notably, loss of DMT1 fostered the outgrowth of lung metastatic nodules in both human and murine models of triple-negative breast cancer cells[78]. Thus, depleting mitochondrial iron while accumulating it in endo-lysosomes could enhance the metastatic ability of aggressive cancer cells in secondary organs, a liability that ferroptosis-inducing approaches could target.

Finally, because iron dyshomeostasis and lysosomal–mitochondrial dysfunctions are hallmarks of aging[5,6,84] and various lysosomal-associated diseases, including neurodegenerative disorders[85] linked to enhanced vulnerability to ferroptosis[86], the BDH2–2,5-DHBA inter-organelle cross-talk identified in our study could have broader implications and therapeutic potential.

Methods

Reagents

2,5-DHBA (149357), ammonium iron(II) sulfate hexahydrate (FAS) (203505), ammonium iron(III) citrate (FAC) (F5879), Resomer RG 503H PLGA (719870), Ferrostatin 1 (SML0583) and DFO (D9533),were purchased from Sigma-Aldrich. Liproxstatin-1 (950455-15-9) was purchased from Cayman. SYTOX Green Nucleic Acid Stain (S7020), Viability Dye eFluor 780 (65-0865-14) and BODIPY 581/591 C11 (D3861) were purchased from Thermo Fisher Scientific. IKE (S8877) and RSL3 (S8155) were purchased from Selleckchem. Nec-1s (2263) was purchased from BioVision. Z-Val-Ala-DL-Asp(OMe)-fluoromethylketone (ZVAD) (4027403) was purchased from Bachem. FerroOrange (F374-12) and Mito-FerroGreen (M489-10) were purchased from Dojindo. Lipoxygenase Assay Kit (ab241038) was purchased from Abcam. RhoNox-M[87] was synthesized as previously described[11]. The generation of SPLICS$_S$–P2ALY–MT and SPLICS$_L$–P2ALY–MT plasmids is described in ref. 37.

Cell culture

The human melanoma cell lines M229, M229R, M238, M238R, M249 and M249R were a gift from R. Lo (UCLA), and M202, M395, M233 and M257 were a gift from A. Ribas (UCLA). All the cell lines were maintained in Dulbecco's modified Eagle medium (DMEM) (D6546, Sigma-Aldrich) supplemented with 10% (vol/vol) FBS (PAN-Biotech), 2 mM glutamine (35050-038, Thermo Fisher Scientific) and penicillin (100 units ml^{-1})–streptomycin (0.1 mg ml^{-1}) (P0781, Sigma-Aldrich). Cell lines with acquired resistance to vemurafenib (PLX4032/PLX, 10618-10, Sanbio) (M249R, M229R and M238R) were maintained continuously on 1 µM PLX in cell culture. For specific assays, cells were treated with 100 µM FAS or FAC, 100 µM DFO, 2.5 µM ironomycin and 1 mM 2,5-DHBA for 24 h; 100 nM bafilomycin A1 and 1 µM oligomycin for 1 h; and 1 µM Liproxstatin-1 for 1 h (imaging) or 24 h (lipid peroxidation and cell death). To generate shCTR-, sh*MITF*- and sh*BDH2*-transfected M229 cells and EV or RAB7-WT-, RAB7-Q67L-, RAB7-T22N- and BDH2-overexpressing M229R cells, following viral particle production and transduction, cells that had integrated the constructs were kept under antibiotic selection. Human short-term patient-derived melanoma cell lines MM001 and MM099 were derived from patient biopsies by the Laboratory of Oncology and Experimental Surgery (G. Ghanem, Institute Jules Bordet). These cells were maintained in Ham's F-10 nutrient mix medium (22390, Thermo Fisher Scientifics), supplemented

with 10% FBS, 2.4% L-glutamine and 1% penicillin–streptomycin. The murine melanoma cell line YUMM3.3 dsRed was a gift from A. Tasdogan (Institute for Tumor Metabolism, University Hospital Essen). These cells were maintained in DMEM/F12 (11520396, Thermo Fisher Scientific) medium containing 10% FBS and supplemented with 1% penicillin–streptomycin. All cells were maintained routinely in 5% CO_2 and 95% air at 37 °C. Cells were routinely checked for mycoplasma contamination using the plasmotest kit (Invivogen), according to the manufacturer's instructions.

Nucleofection

Nucleofection was used to transiently transfect cells with siRNAs or plasmids and to stably knock out genes of interest. Nucleofection was performed using the SF 4D-Nucleofector kit (V4XC-2024, Lonza), following the protocol recommended by the manufacturer. To knock down BDH2, siRNA transient nucleofection was performed using 200 nM of non-targeting siRNA (Horizon) or siRNA against human *BDH2* (Horizon). Knockout was achieved by nucleofecting ribonucleoprotein complexes (RNPs) consisting of pooled sgRNAs against a scrambled region or against BDH2 or MITF conjugated with Cas9 (Synthego). To transiently express the SPLICS–P2ALY–MT reporters[37] and the FIRE–pHLy plasmid[88], nucleofection was performed using 2.5 µg of the plasmids. Experiments were conducted using pooled clones.

Acidic nanoparticles preparation

AcNPs were prepared as previously described[41]. In brief, 31 mg of Resomer RG 503H PLGA (lactide to glycolide ratio 50:50, molecular weight 24–38 kDa) (719870, Sigma-Aldrich) was dissolved in 3.1 ml of tetrahydrofuran, and subsequently 500 µl of this solution was simultaneously injected (3 ml × min^{-1}) with 1.5 ml of deionized water (9 ml × min^{-1}) using syringe pumps, resulting in a concentration of 2.5 mg × ml^{-1}. Cells were then treated with 1 µM acNP for 24 h.

Imaging

Airyscan live-cell imaging of Fe(II). Cells were seeded on glass-bottom dishes with 1.5 mm coverslips (P35G-1.5-14-C, Mattek) and stained with LysoTracker green (L7526, Thermo Fisher Scientific), MitoTracker deep red (M22426, Invitrogen), FerroOrange (F374, Dojindo) and Mito-FerroGreen (M489, Dojindo), according to the manufacturer's instructions. Cells were imaged in HBSS (14025092, Thermo Fisher Scientific). Image acquisition was performed using an inverted Zeiss LSM880 microscope in fast Airyscan mode with a Plan Apochromat ×60 oil objective lens (NA 1.4). The setup was controlled by ZEN black (v2.3, Carl Zeiss Microscopy). Image processing and analysis were performed using ImageJ/Fiji Software.

Widefield live-cell imaging for lysosomal pH measurement. Cells were seeded on glass-bottom dishes with 1.5-mm coverslips (P35G-1.5-14-C, Mattek) and stained with LysoSensor Yellow/Blue DND-160 (L7545, Thermo Fisher Scientific) in HBSS (14025092, Thermo Fisher Scientific). Image acquisition was done using an Olympus IX81 Cell^R microscope equipped with a Hamamatsu Image EM EM-CCD camera and a Plan Apochromat Scientific ×40 oil objective lens (NA 1.3) with a ×1.6 camera relay lens. The fluorophore was excited through a mercury lamp, with 340/11 excitation filter; the signal was collected with an 525/50 emission filter (at the isosbestic point). Image processing and analysis were performed using ImageJ/Fiji Software.

SPLICS reporter Airyscan imaging. Following nucleofection of the $SPLICS_S$–P2ALY–MT and $SPLICS_L$–P2ALY–MT plasmids, cells were seeded on glass-bottom dishes with 1.5 mm coverslips (P35G-1.5-14-C, Mattek) and fixed with 4% PFA for 15 min. Imaging was performed using an inverted Zeiss LSM880 microscope in fast Airyscan mode with a Plan Apochromat ×60 oil objective (NA 1.4). Z-stacks were collected at the Nyquist sampling rate. The setup was controlled by ZEN black (v2.3, Carl Zeiss Microscopy). Image processing and analysis were performed using Imaris (v10.2).

Structured illumination microscopy for measurement of mitochondria–lysosome contacts. For image acquisition, an inverted Zeiss Elyra 7 (with lattice SIM module for structured illumination) microscope equipped with two PCO.edge 4.2 CLHS sCMOS cameras in combination with a ×63 Plan Apochromat objective (NA 1.40) was used. The setup was controlled by ZEN black (v3.0, Carl Zeiss Microscopy). MitoTracker Deep Red was excited using a 640 nm laser (0.20% of a 500 mW diode), and the emission was captured above 640 nm on camera 1 with a 50-ms exposure time. RDA was excited with a 561 nm laser (0.25% of a 500 mW diode), and the emission was collected between 560 and 640 nm on camera 2 with a 50 ms exposure time. Lysotracker green was excited with a 488 nm laser (0.20% of a 500 mW diode), and the emission was collected between 490 and 560 nm on camera 1 with a 30 ms exposure time. The same combination of filters (LBF405/488/561/647 and BP 490-560 + LP640) was used for every channel, with sequential acquisition. Lysosome–mitochondria dynamics were recorded in a time-lapse experiment without delay between the timepoints (4.2-s interval), implementing a focus strategy every five time points. Images were captured at 512×512 pixels with a sampling rate of 63 nm pixel−, with the same SIM grid (grid G3 with 36.5 µm spacing) to optimize the imaging speed. Images were processed by SIM reconstruction using a processing strength of 7.0 for the Mitochondria Deep Red channel, and 6.5 for Lysotracker Green and RDA channels. The baseline cut was scaled to the raw image, and the detrend option was used for bleaching correction. For image analysis, mitochondria were segmented using a pixel classifier trained in Ilastik on images acquired in the MitoTracker channel. Lysosomes were then detected using StarDist, which was applied to images stained with LysoTracker. Lysosomal tracking was performed using the trackpy library, with a search range of 15 pixels and a memory of 2 frames. To assess interactions between mitochondria and lysosomes, a ring-shaped region was generated around each lysosome. The overlap between segmented mitochondria and each lysosomal ring was calculated to identify contact sites between the two organelles (MLC). For each contact region, the mean intensity of RDA was measured as a proxy for signal at the MLC. As a control (no contact), the mean RDA intensity across the entire mitochondrial network was considered. Boxplots in Figure 2 show the quantification of the average difference (Δ) in MFI of RDA per cell, measured between the end and start of MLC events. This quantification compares 'MLC' regions, that is, overlapping $MitoTracker^+LysoTracker^+$ areas, to 'No MLC' regions, defined as the mean RDA intensity in the $MitoTracker^+$ areas during the same time interval.

Immunocytochemistry and Airyscan imaging. Cells were seeded on glass-bottom dishes with 1.5 mm coverslips (P35G-1.5-14-C, Mattek), fixed with 4% PFA for 15 min, followed by permeabilization and blocking in 0.1% saponin, 5% normal goat serum for 1 h. Cells were incubated with primary antibodies (1:100 anti-Lamp1 (Ab25630, Abcam), 1:100 anti-Tom20 (ab186735, Abcam)) overnight at 4 °C and were then washed before the addition of secondary antibodies conjugated with Alexa Fluor 488 (1:500, A11034 or A11029, Invitrogen) for 1 h at room temperature (RT). Coverslips were mounted with Prolong Gold (P36934, Thermo Fisher Scientific). Images were acquired in an inverted Zeiss LSM880 microscope in fast Airyscan mode with a Plan Apochromat ×60 oil objective lens (NA 1.4). Z-stacks were captured at the Nyquist sampling rate. The setup was controlled by ZEN black (v2.3, Carl Zeiss Microscopy). Image processing and analysis were performed using ImageJ/Fiji software. Colocalization analysis was performed using the JAcoP plugin, Manders coefficients[89].

Immunocytochemistry and structured illumination microscopy. Cells were seeded on chemically cleaned 1.5H high-performance coverslips (0109030091, Marienfeld). Cells were fixed with 4% PFA

and 0.05% glutaraldehyde for 15 min, followed by permeabilization and blocking in 0.1% saponin and 5% normal goat serum for 1 h. Cells were incubated with primary antibodies (1:100 anti-Lamp1 (ab24170, Abcam), 1:100 anti-Tom20 (ab289670 or ab186735 Abcam), 1:00 anti-Bdh2 (sc-393030, Santa Cruz Biotechnology)) overnight at 4 °C followed by washing before the addition of secondary antibodies conjugated with Alexa Fluor 488, Alexa Fluor 546 or Alexa Fluor 647 (1:500, A11030 or A11034 or A48265, Invitrogen) for 1 h at RT. After immunocytochemistry, samples were mounted with Prolong Glass (P36980, Thermo Fisher Scientific). Image acquisition was done with a Nikon Ti2 N-SIM S microscope equipped with a Hamamatsu ORCA-Flash 4.0 (C13440) in combination with an SR HP Apo TIRF ×100 objective lens (NA 1.49). The setup was controlled using NIS-Elements 5.30.07 (Build 1569). Stacks of 3 µm were acquired in 3D SIM mode (3 angles and 5 phases per image), with a step size of 0.06 µm. Samples were excited sequentially with 488 nm, 561 nm or 640 nm lasers; the emissions were collected using bandpass filters of 525/30, 595/30 or Cy5 em, respectively. Stack reconstruction was optimized for each wavelength and performed in batches per experiment. Postprocessing and image analysis were done in batches using NIS-Elements 5.42.03 (Nikon). The GA3 analysis protocol included background subtraction of a constant noise background and automated 3D thresholding. A manual threshold was applied for mitochondria when necessary. Binary masks were added to find overlapping 3D structures, which were counted, and their volume was measured. Image visualization was done using Imaris. Alternatively, image acquisition was done with an inverted Zeiss Elyra 7 (with lattice SIM module for structured illumination) microscope, equipped with two PCO.edge 4.2 CLHS sCMOS cameras in combination with a Plan Apochromat ×60 objective lens (NA 1.4). The setup was controlled by ZEN black (v3.0, Carl Zeiss Microscopy). Samples were excited sequentially either with a 488 nm or 561 nm laser. Emission was collected with a bandpass filter 420–480 or 570–620, respectively. Image processing and analysis were performed using Imaris (v10.2).

Multiplex immunocytochemistry. Tissue samples from representative lesions were collected and fixed in 4% paraformaldehyde for 24 h and then processed for paraffin embedding (HistoStar Embedding Workstation). Sections of 4 µm of thickness obtained from the paraffin-embedded tissues (Thermo Scientific Microm HM355S microtome) were mounted on Superfrost Plus Adhesion slides (Thermo Scientific). The following antibodies were used: anti-BDH2 (rabbit, 1:100, Novus Biologicals, NBP2-32713), anti-SLC25A37 (rabbit, 1:50, ProteinTech, 26469-1), anti-MITF (rabbit, 1: 200, Sigma, HPA003259) and anti-RAB7 (rabbit, 1:100, Cell Signalling, 9367). Furthermore, the Opal 6-Plex Detection Kit - for Whole Slide Imaging (Akoya, NEL871001KT) was used for tyramide signal amplification, following the manufacturer's protocol. For introduction of the secondary horseradish peroxidase (HRP), the Envision+/HRP goat anti-rabbit (Dako Envision+ Single Reagents, HRP, Rabbit, Code K4003) was used for all antibodies. The various proteins were detected by using the OPAL 520 (BDH2), OPAL 690 (SLC25A37), OPAL 480 (MITF), OPAL 570 (S100A1) or OPAL 780 (RAB7) reagents, according to the manufacturer's protocol. Images were acquired on the Akoya PhenoImager HT (formerly known as Vectra Polaris) using a ×20 objective without binning.

ChIP–seq. All the methodology and conditions used for the ChIP–seq performed in 501Mel cells and subsequent data analyses were previously described in Laurette et al.[90] and are publicly available at GSE61967. The FOSL2 and TEAD4 ChIP–seq data are previously described in Fontanals-Cirera et al.[91] and are publicly available at GSE94488.

Total iron measurement

Intracellular total iron and iron redox species (Fe(II), Fe(III)) measurements. Cells were lysed in modified RIPA lysis buffer containing PBS pH 7.4, 0.5% sodium deoxycholate, 1% NP-40 containing 1 mM PMSF, 1 mM orthovanadate and 1× cOmplete Protease Inhibitor on ice for 45 min with gentle agitation. Cell lysates were centrifuged at 10,000*g* for 10 min, and supernatants were analysed. Speciation and quantification of Fe(II) and Fe(III) were performed by capillary electrophoresis inductively coupled plasma mass spectrometry (CE-ICP-MS), as previously described[92]. In brief, samples were analysed on a 'PrinCe 706' CE system equipped with an uncoated capillary (85 cm × 50 µm ID) and a laboratory-constructed CE-ICP-MS interface for element selective iron quantification of separated iron redox species at ICP-DRC-MS. Separation and quantification of Fe(II) and Fe(III) were performed in 20 mM HCl-electrolyte at a separation voltage of +25 kV separation voltage and ^{56}Fe isotope detection at ICP-DRC-MS. DRC technology, with NH_3 as the reaction gas, was used for interference-free detection of the ^{56}Fe isotope. Total iron content was determined to assess iron-recovery accuracy using ICP-sector field mass spectrometry (ICP-sf-MS). The ICP-sf-MS ('ELEMENT 2', Thermo Fisher Scientific) settings included radio frequency power (1260 W), plasma gas flow (16 L Ar min^{-1}), auxiliary gas flow (0.85 L Ar min^{-1}), nebulizer gas flow (1.085 L Ar min^{-1}) and a dwell time of 300 ms. The sum of quantified iron species per sample from CE-ICP-DRC-MS was compared with total iron content (set at 100%), yielding values ranging between 90% and 107%.

Intracellular Fe(II) measurements. Intracellular Fe(II) content was measured upon staining of cells with FerroOrange (F374, Dojindo) as previously described[93]. In brief, cells were seeded in a black 96-well plate and stained with 1 µM FerroOrange in HBSS. Following incubation with the dye, the plate was read using a Synergy H1 Multimode reader (BioTek), with the excitation set at 543 nm and emission at 580 nm. For protein normalization, cells were collected in RIPA buffer for BCA-based protein quantification.

Cell death assays

Cells were seeded in a clear-bottom white 96-well plate (3610, Costar). Then, 1 µM of SYTOX Green dye (S7020, Thermo Fisher Scientific) was added with the cell death inducers and inhibitors. Cells were first pretreated with the inhibitors for 2 h (30 µM Z-VAD-FMK, 30 µM necrostatin-1s, 100 µM deferoxamine (DFO), 2 µM ferrostatin-1), and then treated with the ferroptosis inducers for 24 h (2.5 µM RSL3, 1.25 µM IKE). After 24 h, the MFI was measured using a Synergy H1 Multimode reader (BioTek), with the excitation set at 485 nm and emission at 538 nm.

3D spheroid model

To create the spheroids, 10,000 cells per well were seeded for 2 days in non-adherent 96-well plates (Nucleon Sphere plates from Thermo Fisher Scientific). After 2 days, spheroids were treated with IKE (10 µM) with or without Liproxstatin-1 (1 µM) for 24 h (6 spheroids per condition). After 24 h, spheroids from the same condition were pooled, washed (5 min at 300*g*) and trypsinized (5 min at 37 °C) to obtain a single-cell suspension. Then the cells were stained for flow cytometry analysis with eFluor 780 Live/Dead dye (for the viability assay) and Bodipy C11 (to detect lipid peroxidation) for 30 min. Cells were analysed with the BD LSFortessa X-20 + HTS flow cytometer.

2,5-DHBA measurement by metabolomics

Cells were lysed using an extraction buffer composed of 80% methanol and containing 2 µM d27 myristic acid. Cell lysates were centrifuged at 20,000*g* for 15 min. The resulting pellet was used for protein quantification and normalization, and the supernatant was used for 2,5-DHBA measurement. 10 µl of each sample was loaded into a Dionex UltiMate 3000 LC System (Thermo Scientific Bremen, Germany) equipped with a C-18 column (Acquity UPLC -HSS T3 1.8 µm; 2.1 × 150 mm, Waters) coupled to a Q Exactive Orbitrap mass spectrometer (Thermo Fisher Scientific) operating in negative ion mode. A step gradient was carried

out using solvent A (10 mM TBA and 15 mM acetic acid) and solvent B (100% methanol). The gradient began with 5% solvent B and 95% solvent A, maintaining this ratio until 2 min postinjection. A linear gradient then increased to 37% B by 7 min and 41% by 14 min. Between 14 and 26 min, the gradient increased to 95% of B, where it remained for 4 min. At 30 min, the gradient returned to 5% B. Chromatography was stopped at 40 min, maintaining a constant flow rate of 0.25 ml min^{-1}, and the column was placed at 40 °C throughout the analysis. The MS operated in full scan mode (*m/z* range: 70.0000–1050.0000) using a spray voltage of 4.80 kV, capillary temperature of 300 °C, sheath gas at 40.0 and auxiliary gas at 10.0. The AGC target was set at 3.0×10^6 using a resolution of ×140,000, with a maximum IT fill time of 512 ms. Data collection was performed using the Xcalibur software (Thermo Fisher Scientific). The data analyses were performed by integrating the peak areas using El-Maven, through Polly (Elucidata). For protein quantification, the pellet obtained from the extraction step was dissolved in a 200 nM NaOH solution and incubated at 95 °C for 20 min. Lysate was cooled down on ice and spun for 10 min at 5,000 r.p.m. using an Eppendorf tabletop centrifuge.

Flow cytometry

Cells were stained with DQ Red BSA (D12051, Thermo Fisher Scientifics), Tetramethylrhodamine (TMRM) (T668, Thermo Fisher Scientifics), MitoTracker green (M7514, Thermo Fisher Scientifics), BODIPY 581/591 C11 (D3861, Thermo Fisher Scientifics) and eBioscience Fixable Viability Dye eFluor 780 (65-0865, Thermo Fisher Scientifics), according to the manufacturer's instructions. Cells were analysed using a BD FACSCanto II system (BD Biosciences), and data were analysed using FCS Express (v6).

Immunoblotting

Cells were lysed in RIPA buffer (89900, Thermo Fisher Scientific). Protein concentrations in cell lysates were determined using the BCA protein assay reagents (23225, Thermo Fisher Scientific). Precision Plus Protein ladder (1610374, Bio-Rad) was used for protein size reference. Samples were separated by SDS–PAGE on the Criterion system (Bio-Rad) on a 4%–12% Bis-TRIS gel and electrophoretically transferred to Amersham Protran 2 µm-pored nitrocellulose paper (GE Healthcare). The blots were blocked for 1 h at RT in TBS-T buffer (50 mM Tris, pH 7.4, 150 mM NaCl, 0.1% Tween-20) containing 5% non-fat dry milk (wt/vol) and then incubated with primary and secondary antibody solutions prepared in blocking buffer. Primary antibodies to MITF (1:1,000, MA5-14154) and OxPhos Human WB Antibody Cocktail (1:1,000, 45-8199) were purchased from Thermo Fisher Scientific; BDH2 (1:1,000, 27207-1-AP) and DMT1 (1:1,000, 20507-1-AP) were purchased from Proteintech; Sox10 (1:1,000, sc-365692), v-ATPase H (1:1,000, sc-166227) and v-ATPase A (1:1,000, sc-374475) were purchased from Santa Cruz Biotechnology; AXL (1:1,000, 8661), SOX9 (1:1,000, 82630), IRP2 (1:1,000, 37135), RAB7 (1:1,000, 2094), HA-Tag (1:1,000, 14904), EGFR (1:1,000, 4267), ZEB1 (1:1,000, 3396), MLKL (1:1,000, 14993) and VDAC (1:1,000, 4866) were purchased from Cell Signaling Technology; TRPML1 (1:1,000, ab28508) and TCF4 (1:1,000, ab217668) were purchased from Abcam; MCU (1:1000, HPA016480) and β-actin (1:2,000, A5441) were purchased from Sigma-Aldrich. Appropriate secondary antibodies for chemical (HRP-based) detection were purchased from Cell Signalling Technologies (7074S, 7076S), and those used for infrared detection were purchased from Invitrogen (35568, 5A535521). Signal detection was performed using the Typhoon infrared-imaging system (GE Healthcare) or Chemidoc MP system (Bio-Rad Laboratories) using the ECL solution from Pierce (32106, Thermo Fisher Scientific). Quantifications by densitometry of the bands were calculated using the software Image Studio (v6, Li-Cor Biosciences).

Quantitative real-time PCR

RNA extraction was performed using RNeasy Plus mini kit (74136, Qiagen) and reverse transcription using the QuantiTect kit (205313, Qiagen), according to the manufacturer's instructions. Gene expression was determined using ORA qPCR Green L mix (QPD0105, HighQu) with an ABI7500 system (Applied Biosystems) and analysed using the $2^{-\Delta\Delta Ct}$ method. To determine mitochondrial mass starting from mitochondrial DNA (mtDNA), two mtDNA sequences were analysed and mtDNA expression was normalized to that of nuclear DNA. Primer sequences are reported in Supplementary Table 4.

Seahorse

Cells were seeded on Seahorse Xp culture plates (102340-100, Agilent) in culture medium overnight. Before the assay began, cells were switched to the Seahorse XF Assay Medium (103575-100, Agilent) pH 7.4, containing 10 mM glucose (103577-100, Agilent), 1 mM sodium pyruvate (103578-100, Agilent) and 2 mM glutamine (103579-100, Agilent). Cells were maintained for 1 h in a CO_2-free incubator at 37 °C. The OCR was measured after serial injections of 1 µM oligomycin (75351, Sigma-Aldrich), 0.5 µM FCCP (1528-10, Sanbio) and 0.5 µM antimycin A (A8674, Sigma-Aldrich). Once the run was finished, all the medium was removed from the wells, and cells were collected in 10 µl RIPA buffer for BCA-based protein quantification. Analysis was performed using Seahorse Wave Desktop Software (Agilent).

NMR

^{1}H NMR spectra were recorded on a 500 MHz Bruker spectrometer at 310 K. Then, 1.0 mg of 2,5-DHBA was dissolved in 600 µl of methanol-d_4 (MeOD, D048FD, Eurisotop). To reach up to 1.0 molar equivalent of $FeCl_3$ or $FeCl_2$, portions of 3.0 µl of iron solutions ($FeCl_3$, 205 mM, or $FeCl_2$, 210 mM, in MeOD) were incrementally added. NMR spectra were collected after each addition. Then, a drop of trifluoroacetic acid (TFA, T6508, Sigma-Aldrich) or sodium deuteroxide (NaOD, D076Y, Eurisotop) was added.

Click chemistry

For in-cell labelling of 2,5-DHBA using click chemistry, the alkyne-containing analogue of 2,5-DHBA (cDHBA) was synthesized by Chemieliva Pharmaceutical. Cells were seeded on 1.5H high-performance coverslips (0109030091, Marienfeld). The following day, cells were treated with 1 mM cDHBA for 2 h and then fixed and permeabilized as described in the immunocytochemistry section. The click reaction was performed using the Click-iT EdU Imaging kit (C10338, Thermo Fisher Scientific), according to the manufacturer's instructions. Subsequently, immunolabelling and imaging were performed as previously described in this paper.

LOX activity assay

Cells were seeded in 5 cm^2 dishes and treated with FAS (100 µM), either alone or in combination with 2,5-DHBA (1 mM). After 24 h, cells were collected and lysed using the LOX lysis buffer provided with the Lipoxygenase Assay Kit (ab241038, Abcam). The assay was performed following the manufacturer's instructions. Fluorescence generated by the reaction was measured using a Synergy H1 Multimode reader (BioTek) with the excitation set at 500 nm and emission at 536 nm in kinetic mode for 40 min. For protein normalization, cells were collected in RIPA buffer for BCA-based protein quantification.

In silico analysis

Publicly available datasets were used for in silico analyses. Single-cell RNA-sequencing data from a PDX melanoma model were obtained from ref. 21 (GSE116237). The raw count matrix was imported in R (v4.1.3) for data analysis, and was analysed using the Seurat R package pipeline (v.4.0.1). Data were normalized and scaled using SCTransform, and cell states were annotated using the original clustering information provided in the metadata (phenotype). Cells were grouped by MITF expression to reflect a MEL versus MES comparison, considering 'MITFinterm_melanocytic' as $MITF^{hi}$ (MEL), and 'mesenchymal-like' and

'NCSC' as MITF^{lo} (MES). Plots were produced in R with ggplot2 (v3.5.1) and differential expression between MITF^{hi} and MITF^{lo} groups was tested by two-sided *t*-test. Bulk RNA-sequencing data from a panel of 51 melanoma cell lines originally profiled for molecular classification were obtained from ref. 28 (GSE80829). For the 51 cell lines, $\log_2$-normalized fragments per kilobase of transcript per million mapped reads (FPKM) values were imported in R (v4.1.3) for data analysis. The normalized counts matrix was subsetted to include only a curated set of 110 genes involved in iron metabolism identified through the Reactome and KEGG pathway databases. Cell lines originally classified in four main subtypes were grouped as follows, to update the nomenclature to a MEL versus MES comparison: 'Melanocytic' and 'Transitory' were annotated as 'MEL'; 'Undifferentiated' and 'Neural crest like' were annotated as 'MES'. Principal component analysis was performed using prcomp considering only the iron metabolism geneset. Figure 3b and Extended Data Fig. 5a were produced in R with ggplot2 (v3.5.1), $\log_2$(FPKM) was scaled by gene and the differential expression between the MES and MEL groups was tested by two-sided *t*-test with a significance threshold of $P < 0.05$.

Animal studies

Animal procedures were approved by the Institutional Animal Care and Research Advisory Committee of the KU Leuven (ECD P116/2023) and were performed following the institutional and national guidelines and regulations. C57BL/6J 7-week-old female mice were used for all the experiments.

Tail-vein injections

One million YUMM3.3 dsRed cells, either untreated or pretreated with Liproxstatin-1 (5 µM) or 2.5-DHBA (5 mM), were injected in the tail vein of 7-week-old C57BL/6 female mice. Twenty-four hours postinjection, the mice were euthanized, and their lungs were collected in PBS on ice. The lungs were cut into small fragments in a Petri dish and put in gentleMACS C Tubes holding 3 ml of digestion solution (DMEM F12 medium completed with Gibco collagenase type II (10 mg ml^{-1}), type IV (25 mg ml^{-1}) and DNAse I (15 µg ml^{-1})). The samples were run on the gentleMACS Octo Dissociator following three consecutive programmes: (1) 30 s 165 r.p.r (rotations per revolution) at RT, (2) 30 min 600 r.p.r. at 37 °C, and (3) 30 s 2000 r.p.r. at RT. After digestion, the samples were passed through a 70 µm pluriStrainer Mini, washed with PBS, and counted. Ten million cells from each lung sample were stained with a viability dye (eFluor780) for 30 min on ice. After washing, all the samples were recorded on the BD Fortessa Cytometer. A similar experiment was done by injecting one million untreated EV- or BDH2-overexpressing YUMM3.3 dsRed cells. Lungs were collected 1 day after the tail-vein injection and processed as described above.

Statistical analysis

Data represent the mean ± s.e.m. of biologically independent experiments. For box plots, boxes represent the interquartile range and median, and whiskers indicate the minimum and maximum values. *n* values represent the number of independent experiments performed (in vitro data), the number of cells per condition (imaging) or the number of animals per condition (in vivo). Cells and mice were randomly assigned to the different experimental groups. For each independent in vitro experiment, unless otherwise specified, a minimum of three biological replicates was used as a standard, and sample sizes were increased in more complex experiments to ensure reproducibility. No statistical methods were used to predetermine sample sizes, but our sample sizes are similar to those reported in previous publications[13,64,79]. Data collection and analysis were not performed blind to the conditions of the experiments. No mice or data points were excluded. All statistical analyses were conducted using GraphPad Prism 10. In brief, for comparisons between two groups, two-tailed Student's *t*-tests were used. Two-tailed one-sample *t*-tests were applied for relative comparisons in which control values were normalized to 1. For comparisons involving more than two groups, one-way ANOVA with Tukey multiple-comparison correction was applied. For Student's *t*-tests and one-sample *t*-tests, the data distribution was assumed to be normal, but this was not formally tested. For ANOVAs, the normality of the residuals was tested using the Shapiro–Wilk test. Detection of mathematical outliers was performed using the ROUT test in GraphPad, and significant outliers were excluded. $P < 0.05$ was considered statistically significant.

Reporting summary

Further information on research design is available in the Nature Portfolio Reporting Summary linked to this article.

Data availability

Single-cell RNA-sequencing and bulk RNA-sequencing data reanalysed in this study are available at GEO: GSE116237 and GSE80829, respectively. Gel source images are provided in this paper. All other data supporting the findings of this study are available within the article and Supplementary Information and from the corresponding authors upon reasonable request. Source data are provided with this paper.

References

1. Rizzollo, F., More, S., Vangheluwe, P. & Agostinis, P. The lysosome as a master regulator of iron metabolism. *Trends Biochem. Sci.* **46**, 960–975 (2021).
2. Galy, B., Conrad, M. & Muckenthaler, M. Mechanisms controlling cellular and systemic iron homeostasis. *Nat. Rev. Mol. Cell Biol.* **25**, 133–155 (2024).
3. Salnikow, K. Role of iron in cancer. *Semin. Cancer Biol.* **76**, 189–194 (2021).
4. Weber, R. A. et al. Maintaining iron homeostasis is the key role of lysosomal acidity for cell proliferation. *Mol. Cell* **77**, 645–655 (2020).
5. Hughes, C. E. et al. Cysteine toxicity drives age-related mitochondrial decline by altering iron homeostasis. *Cell* **180**, 296–310 (2020).
6. Yambire, K. F. et al. Impaired lysosomal acidification triggers iron deficiency and inflammation in vivo. *eLife* **8**, e51031 (2019).
7. Ben Zichri- David, S., Shkuri, L. & Ast, T. Pulling back the mitochondria's iron curtain. *npj Metab. Health Dis.* **3**, 6 (2025).
8. Rouault, T. A. & Tong, W.-H. Iron–sulphur cluster biogenesis and mitochondrial iron homeostasis. *Nat. Rev. Mol. Cell Biol.* **6**, 345–351 (2005).
9. Dixon, S. J. et al. Ferroptosis: an iron-dependent form of nonapoptotic cell death. *Cell* **149**, 1060–1072 (2012).
10. Tian, R. et al. Genome-wide CRISPRi/a screens in human neurons link lysosomal failure to ferroptosis. *Nat. Neurosci.* **24**, 1020–1034 (2021).
11. Mai, T. T. et al. Salinomycin kills cancer stem cells by sequestering iron in lysosomes. *Nat. Chem.* **9**, 1025–1033 (2017).
12. Conrad, M. & Pratt, D. A. The chemical basis of ferroptosis. *Nat. Chem. Biol.* **15**, 1137–1147 (2019).
13. Cañeque, T. et al. Activation of lysosomal iron triggers ferroptosis in cancer. *Nature* **8642**, 492–500 (2025).
14. Seiler, A. et al. Glutathione peroxidase 4 senses and translates oxidative stress into 12/15-lipoxygenase dependent- and AIF-mediated cell death. *Cell Metab.* **8**, 237–248 (2008).
15. Stockwell, B. R. et al. Ferroptosis: a regulated cell death nexus linking metabolism, redox biology, and disease. *Cell* **171**, 273–285 (2017).
16. Dixon, S. J. & Olzmann, J. A. The cell biology of ferroptosis. *Nat. Rev. Mol. Cell Biol.* **25**, 424–442 (2024).
17. Müller, S. et al. CD44 regulates epigenetic plasticity by mediating iron endocytosis. *Nat. Chem.* **12**, 929–938 (2020).

18. Marine, J.-C., Dawson, S.-J. & Dawson, M. A. Non-genetic mechanisms of therapeutic resistance in cancer. *Nat. Rev. Cancer* **20**, 743–756 (2020).
19. Ciriello, G. et al. Cancer evolution: a multifaceted affair. *Cancer Discov.* **14**, 36–48 (2024).
20. Rodriguez, R., Schreiber, S. L. & Conrad, M. Persister cancer cells: iron addiction and vulnerability to ferroptosis. *Mol. Cell* **82**, 728–740 (2022).
21. Rambow, F. et al. Toward minimal residual disease-directed therapy in melanoma. *Cell* **174**, 843–855 (2018).
22. Rambow, F., Marine, J.-C. & Goding, C. R. Melanoma plasticity and phenotypic diversity: therapeutic barriers and opportunities. *Genes Dev.* **33**, 1295–1318 (2019).
23. White, R. M. & Zon, L. I. Melanocytes in development, regeneration, and cancer. *Cell Stem Cell* **3**, 242–252 (2008).
24. Andrews, M. C. et al. Multi-modal molecular programs regulate melanoma cell state. *Nat. Commun.* **13**, 4000 (2022).
25. Pedri, D., Karras, P., Landeloos, E., Marine, J. & Rambow, F. Epithelial-to-mesenchymal-like transition events in melanoma. *FEBS J.* **289**, 1352–1368 (2022).
26. Pozniak, J. et al. A TCF4-dependent gene regulatory network confers resistance to immunotherapy in melanoma. *Cell* **187**, 166–183 (2024).
27. Hoek, K. S. et al. In vivo switching of human melanoma cells between proliferative and invasive states. *Cancer Res.* **68**, 650–656 (2008).
28. Tsoi, J. et al. Multi-stage differentiation defines melanoma subtypes with differential vulnerability to drug-induced iron-dependent oxidative stress. *Cancer Cell* **33**, 890–904 (2018).
29. Wang, H. et al. FBXL5 regulates IRP2 stability in iron homeostasis via an oxygen-responsive [2Fe2S] Ccluster. *Mol. Cell* **78**, 31–41(2020).
30. Wang, J. et al. Iron-mediated degradation of IRP2, an unexpected pathway involving a 2-oxoglutarate-dependent oxygenase activity. *Mol. Cell. Biol.* **24**, 954–965 (2004).
31. Stehling, O. & Lill, R. The role of mitochondria in cellular iron–sulfur protein biogenesis: mechanisms, connected processes, and diseases. *Cold Spring Harb. Perspect. Biol.* **5**, a011312 (2013).
32. Ratnikov, B. I., Scott, D. A., Osterman, A. L., Smith, J. W. & Ronai, Z. A. Metabolic rewiring in melanoma. *Oncogene* **36**, 147–157 (2017).
33. Garciaz, S. et al. Pharmacologic reduction of mitochondrial iron triggers a noncanonical BAX/BAK-dependent cell death. *Cancer Discov.* **12**, 774–791 (2022).
34. Wong, Y. C., Ysselstein, D. & Krainc, D. Mitochondria–lysosome contacts regulate mitochondrial fission via RAB7 GTP hydrolysis. *Nature* **554**, 382–386 (2018).
35. Rizzollo, F. & Agostinis, P. Mitochondria–lysosome contact sites: emerging players in cellular homeostasis and disease. *Contact* **8**, 25152564251329250 (2025).
36. Alonso-Curbelo, D. et al. RAB7 controls melanoma progression by exploiting a lineage-specific wiring of the endolysosomal pathway. *Cancer Cell* **26**, 61–76 (2014).
37. Giamogante, F. et al. A SPLICS reporter reveals α-synuclein regulation of lysosome-mitochondria contacts which affects TFEB nuclear translocation. *Nat. Commun.* **15**, 1516 (2024).
38. Rauen, U. et al. Assessment of chelatable mitochondrial iron by using mitochondrion-selective fluorescent iron indicators with different iron-binding affinities. *ChemBioChem* **8**, 341–352 (2007).
39. Peng, W., Wong, Y. C. & Krainc, D. Mitochondria–lysosome contacts regulate mitochondrial Ca^{2+} dynamics via lysosomal TRPML1. *Proc. Natl Acad. Sci. USA* **117**, 19266–19275 (2020).
40. Vrijsen, S. et al. Inter-organellar communication in Parkinson's and Alzheimer's disease: looking beyond endoplasmic reticulum–mitochondria contact sites. *Front. Neurosci.* **16**, 900338 (2022).
41. Cunha, A. et al. Trehalose-based nucleolipids as nanocarriers for autophagy modulation: an in vitro study. *Pharmaceutics* **14**, 857 (2022).
42. Arotcarena, M. et al. Acidic nanoparticles protect against α-synuclein-induced neurodegeneration through the restoration of lysosomal function. *Aging Cell* **21**, e13584 (2022).
43. Bourdenx, M. et al. Nanoparticles restore lysosomal acidification defects: implications for Parkinson and other lysosomal-related diseases. *Autophagy* **12**, 472–483 (2016).
44. Wolff, N. A. et al. Evidence for mitochondrial localization of divalent metal transporter 1 (DMT1). *FASEB J.* **28**, 2134–2145 (2014).
45. Mackenzie, B., Takanaga, H., Hubert, N., Rolfs, A. & Hediger, M. A. Functional properties of multiple isoforms of human divalent metal-ion transporter 1 (DMT1). *Biochem. J.* **403**, 59–69 (2007).
46. Ludwiczek, S. et al. Ca^{2+} channel blockers reverse iron overload by a new mechanism via divalent metal transporter-1. *Nat. Med.* **13**, 448–454 (2007).
47. Dong, X.-P. et al. The type IV mucolipidosis-associated protein TRPML1 is an endolysosomal iron release channel. *Nature* **455**, 992–996 (2008).
48. Uzarska, M. A. et al. Mitochondrial Bol1 and Bol3 function as assembly factors for specific iron-sulfur proteins. *eLife* **5**, e16673 (2016).
49. Ben-Shimon, L. et al. Fe-S cluster coordination of the chromokinesin KIF4A alters its subcellular localization during mitosis. *J. Cell Sci.* **131**, jcs211433 (2018).
50. McCoubrey, W. K., Ewing, J. F. & Maines, M. D. Human heme oxygenase-2: characterization and expression of a full-length cDNA and evidence suggesting that the two HO-2 transcripts may differ by choice of polyadenylation signal. *Arch. Biochem. Biophys.* **295**, 13–20 (1992).
51. Ishikawa, K. et al. Heme oxygenase-2. *J. Biol. Chem.* **270**, 6345–6350 (1995).
52. Cunha, L. et al. Human uroporphyrinogen III synthase: NMR-based mapping of the active site. *Proteins Struct. Funct. Bioinf.* **71**, 855–873 (2008).
53. Mathews, M. A. A. Crystal structure of human uroporphyrinogen III synthase. *EMBO J.* **20**, 5832–5839 (2001).
54. Richardson, D. R. et al. Mitochondrial iron trafficking and the integration of iron metabolism between the mitochondrion and cytosol. *Proc. Natl Acad. Sci. USA* **107**, 10775–10782 (2010).
55. Shi, X. et al. Combinatorial GxGxE CRISPR screen identifies SLC25A39 in mitochondrial glutathione transport linking iron homeostasis to OXPHOS. *Nat. Commun.* **13**, 2483 (2022).
56. Shaw, G. C. et al. Mitoferrin is essential for erythroid iron assimilation. *Nature* **440**, 96–100 (2006).
57. Kleven, M. D., Dlakić, M. & Lawrence, C. M. Characterization of a single b-type heme, FAD, and metal binding sites in the transmembrane domain of six-transmembrane epithelial antigen of the prostate (STEAP) family proteins. *J. Biol. Chem.* **290**, 22558–22569 (2015).
58. Kallberg, Y., Oppermann, U., Jörnvall, H. & Persson, B. Short-chain dehydrogenases/reductases (SDRs). *Eur. J. Biochem.* **269**, 4409–4417 (2002).
59. Devireddy, L. R., Hart, D. O., Goetz, D. H. & Green, M. R. A mammalian siderophore synthesized by an enzyme with a bacterial homolog involved in enterobactin production. *Cell* **141**, 1006–1017 (2010).
60. Liu, Z. et al. Regulation of mammalian siderophore 2,5-DHBA in the innate immune response to infection. *J. Exp. Med.* **211**, 1197–1213 (2014).
61. Shvartsman, M. & Ioav Cabantchik, Z. Intracellular iron trafficking: role of cytosolic ligands. *Biometals* **25**, 711–723 (2012).

62. Correnti, C. et al. Siderocalin/Lcn2/NGAL/24p3 does not drive apoptosis through gentisic acid mediated iron withdrawal in hematopoietic cell lines. *PLoS ONE* **7**, e43696 (2012).
63. Porcelli, A. M. et al. pH difference across the outer mitochondrial membrane measured with a green fluorescent protein mutant. *Biochem. Biophys. Res. Commun.* **326**, 799–804 (2005).
64. Elia, I. et al. Proline metabolism supports metastasis formation and could be inhibited to selectively target metastasizing cancer cells. *Nat. Commun.* **8**, 15267 (2017).
65. Tidwell, T. R., Røsland, G. V., Tronstad, K. J., Søreide, K. & Hagland, H. R. Metabolic flux analysis of 3D spheroids reveals significant differences in glucose metabolism from matched 2D cultures of colorectal cancer and pancreatic ductal adenocarcinoma cell lines. *Cancer Metab.* **10**, 9 (2022).
66. Abuwatfa, W. H., Pitt, W. G. & Husseini, G. A. Scaffold-based 3D cell culture models in cancer research. *J. Biomed. Sci.* **31**, 7 (2024).
67. Zanoni, M. et al. Modeling neoplastic disease with spheroids and organoids. *J. Hematol. Oncol.* **13**, 97 (2020).
68. Russell, W. R., Scobbie, L., Duthie, G. G. & Chesson, A. Inhibition of 15-lipoxygenase-catalysed oxygenation of arachidonic acid by substituted benzoic acids. *Bioorg. Med. Chem.* **16**, 4589–4593 (2008).
69. Geserick, P. et al. Absence of RIPK3 predicts necroptosis resistance in malignant melanoma. *Cell Death Dis.* **6**, e1884 (2015).
70. Podder, B. et al. TAK1 suppresses RIPK1-dependent cell death and is associated with disease progression in melanoma. *Cell Death Differ.* **26**, 2520–2534 (2019).
71. Ubellacker, J. M. et al. Lymph protects metastasizing melanoma cells from ferroptosis. *Nature* **585**, 113–118 (2020).
72. Labelle, M. & Hynes, R. O. The initial hours of metastasis: the importance of cooperative host–tumor cell interactions during hematogenous dissemination. *Cancer Discov.* **2**, 1091–1099 (2012).
73. Khalil, S. et al. A specialized pathway for erythroid iron delivery through lysosomal trafficking of transferrin receptor 2. *Blood Adv.* **1**, 1181–1194 (2017).
74. Cantarero, L. et al. Mitochondria–lysosome membrane contacts are defective in GDAP1-related Charcot–Marie–Tooth disease. *Hum. Mol. Genet* **29**, 3589–3605 (2021).
75. Liu, Z., Ciocea, A. & Devireddy, L. Endogenous siderophore 2,5-dihydroxybenzoic acid deficiency promotes anemia and splenic iron overload in mice. *Mol. Cell. Biol.* **34**, 2533–2546 (2014).
76. Mims, M. P. & Prchal, J. T. Divalent metal transporter 1. *Hematology* **10**, 339–345 (2005).
77. Li, M. et al. Structural basis of dual Ca^{2+}/pH regulation of the endolysosomal TRPML1 channel. *Nat. Struct. Mol. Biol.* **24**, 205–213 (2017).
78. Barra, J. et al. DMT1-dependent endosome-mitochondria interactions regulate mitochondrial iron translocation and metastatic outgrowth. *Oncogene* **43**, 650–667 (2024).
79. Hangauer, M. J. et al. Drug-tolerant persister cancer cells are vulnerable to GPX4 inhibition. *Nature* **551**, 247–250 (2017).
80. Viswanathan, V. S. et al. Dependency of a therapy-resistant state of cancer cells on a lipid peroxidase pathway. *Nature* **547**, 453–457 (2017).
81. More, S. et al. Secreted Apoe rewires melanoma cell state vulnerability to ferroptosis. *Sci. Adv.* **10**, eadp6164 (2024).
82. Li, B. et al. Inactivation of 3-hydroxybutyrate dehydrogenase type 2 promotes proliferation and metastasis of nasopharyngeal carcinoma by iron retention. *Br. J. Cancer* **122**, 102–110 (2020).
83. Liang, H. et al. BDH2 is downregulated in hepatocellular carcinoma and acts as a tumor suppressor regulating cell apoptosis and autophagy. *J. Cancer* **10**, 3735–3745 (2019).
84. Deshwal, S., Fiedler, K. U. & Langer, T. Mitochondrial proteases: multifaceted regulators of mitochondrial plasticity. *Annu. Rev. Biochem.* **89**, 501–528 (2020).
85. Cisneros, J., Belton, T. B., Shum, G. C., Molakal, C. G. & Wong, Y. C. Mitochondria-lysosome contact site dynamics and misregulation in neurodegenerative diseases. *Trends Neurosci.* **45**, 312–322 (2022).
86. Ryan, S. K. et al. Therapeutic inhibition of ferroptosis in neurodegenerative disease. *Trends Pharmacol. Sci.* **44**, 674–688 (2023).
87. Hirayama, T., Okuda, K. & Nagasawa, H. A highly selective turn-on fluorescent probe for iron(ii) to visualize labile iron in living cells. *Chem. Sci.* **4**, 1250 (2013).
88. Chin, M. Y. et al. Genetically encoded, pH-sensitive mTFP1 biosensor for probing lysosomal pH. *ACS Sens.* **6**, 2168–2180 (2021).
89. BOLTE, S. & Cordelières, F. P. A guided tour into subcellular colocalization analysis in light microscopy. *J. Microsc.* **224**, 213–232 (2006).
90. Laurette, P. et al. Transcription factor MITF and remodeller BRG1 define chromatin organisation at regulatory elements in melanoma cells. *eLife* **4**, e06857 (2015).
91. Fontanals-Cirera, B. et al. Harnessing BET inhibitor sensitivity reveals AMIGO2 as a melanoma survival gene. *Mol. Cell* **68**, 731–744.e9 (2017).
92. Michalke, B., Willkommen, D. & Venkataramani, V. Iron redox speciation analysis using capillary electrophoresis coupled to inductively coupled plasma mass spectrometry (CE-ICP-MS). *Front Chem.* **7**, 136 (2019).
93. Vara-Pérez, M. et al. BNIP3 promotes HIF-1α-driven melanoma growth by curbing intracellular iron homeostasis. *EMBO J.* **40**, e106214 (2021).

Acknowledgements

We thank G. Ghanem, R. Lo (UCLA) and A. Ribas for providing us with the human melanoma cell lines, and A. Tasdogan (Institute for Tumor Metabolism, University Hospital Essen, Germany) for providing us with the YUMM3.3 dRed cells. We thank the VIB Bio Imaging Core for their support and assistance in image acquisition and analysis, and W. Annaert for providing access to the Zeiss Elyra 7 microscope, funded by the Flemish Research Foundation (FWO) Heavy Infrastructure grant I001322N (3SUREMIND). The authors would like to thank the staff of the KU Leuven PDX platform TRACE for access to data from established melanoma PDX models. This work was supported by grants from the FWO (G0A3320N), the Stichting tegen Kanker (F/2022/2037), the KU Leuven C14/21/095 InterAction consortium, the EOS DECODE consortium N° 30837538, the EOS MetaNiche consortium N° 40007532 and the iBOF/21/053 ATLANTIS network to P.A. F.R. received a doctoral fellowship (11L7622N) and J.B. a postdoctoral fellowship (1247924N) from the FWO. T.C. is supported by grants from the Ministry of University and Research (PRIN2017 no. 2017E5L5P3 and PRIN2022 no. 2022XKAAZ7); from the Università degli Studi di Padova (STARS Consolidator Grant 2019 to T.C. and Progetto di Ateneo 2023 no. CALI_BIRD23_01), PNRR — CN3 National Center for Gene Therapy and Drugs based on RNA Technology no. CN00000041 (2022–26). B.M. and V.V. were supported by the Deutsche Forschungsgemeinschaft (German Research Foundation, grant VE 1249/1-1).

Author contributions

F.R. designed, performed and analysed most of the experiments. In vitro experiments were performed by F.R. with the technical help of N.B.L. In vivo experiments were designed, performed and analysed by J.B with the technical help of N.B.L. In silico analyses were performed by N.F. Microscopy images were acquired and analysed

by F.R. and A.E.-A acNPs were prepared by F.R. and J.C. Genetically modified cell lines were generated by C.V.D.H. and J.V.A. Multiplex immunohistochemistry of PDX samples was performed by D.N., and analysis was performed by J.B. Iron speciation analysis through CE-ICP-MS was performed by V.V. and B.M. NMR experiments were performed by C.G. S.M., P.H.V., L.B., T.C., I.D., S.H.L.V, P.V., J-C.M. and R.R. provided expertise and discussed the results. F.R. used BioRender to create the figures. F.R. and P.A. wrote and edited the paper. P.A. conceptualized and directed the study. All authors discussed the results and commented on the paper.

Competing interests
The authors declare no competing interests.

Additional information
Extended data is available for this paper at https://doi.org/10.1038/s42255-025-01352-4.

Supplementary information The online version contains supplementary material available at https://doi.org/10.1038/s42255-025-01352-4.

Correspondence and requests for materials should be addressed to Julie Bonnereau or Patrizia Agostinis.

Peer review information *Nature Metabolism* thanks Bruno Galy and the other, anonymous, reviewer(s) for their contribution to the peer review of this work. Primary Handling Editor: Alfredo Giménez-Cassina, in collaboration with the *Nature Metabolism* team.

Francesca Rizzollo[1,2], Abril Escamilla-Ayala[3,4], Nicola Fattorelli[5,6], Natalia Barbara Lysiak[1,2], Sanket More[1,2], Pablo Hernández Varas[3,4], Lucia Barazzuol[7], Chris Van den Haute[8,9], Joris Van Asselberghs[8,9], David Nittner[10], Jonathan Coene[11], Vivek Venkataramani[12,13], Bernhard Michalke[14], Christine Gaillet[15], Tatiana Cañeque[15], Irwin Davidson[16], Steven H. L. Verhelst[11], Peter Vangheluwe[17], Tito Calì[7,18,19], Jean-Christophe Marine[20,21], Raphaël Rodriguez[15], Julie Bonnereau[1,2] ✉ & Patrizia Agostinis[1,2] ✉

[1]Cell Death Research and Therapy Laboratory, Center for Cancer Biology, VIB, Leuven, Belgium. [2]Department of Cellular and Molecular Medicine, KU Leuven, Leuven, Belgium. [3]VIB Bioimaging Core Leuven, VIB Technologies, Leuven, Belgium. [4]VIB-KU Leuven Centre for Brain Disease Research, Department of Neurosciences, KU Leuven, Leuven, Belgium. [5]Microglia and Inflammation in Neurological Disorders (MIND) Lab, VIB Center for Molecular Neurology, VIB, Antwerp, Belgium. [6]Department of Biomedical Sciences, University of Antwerp, Antwerp, Belgium. [7]Department of Biomedical Sciences (DSB), University of Padova, Padova, Italy. [8]Research Group for Neurobiology and Gene Therapy, Department of Neurosciences, KU Leuven, Leuven, Belgium. [9]Leuven Viral Vector Core, Department of Neurosciences, KU Leuven, Leuven, Belgium. [10]Single Cell & Spatial Multiomics, Center for Cancer Biology, VIB, Leuven, Belgium. [11]Laboratory of Chemical Biology, Department of Cellular and Molecular Medicine, KU Leuven, Leuven, Belgium. [12]Department of Internal Medicine II, Medical Oncology, University Hospital Würzburg, Würzburg, Germany. [13]National Center for Tumor Diseases (NCT) WERA, Würzburg, Germany. [14]Research Unit Analytical BioGeoChemistry, Helmholtz Zentrum München, Deutsches Forschungszentrum für Gesundheit und Umwelt, Munich, Germany. [15]Institut Curie, CNRS, INSERM, PSL Research University, Paris, France. [16]Department of Functional Genomics and Cancer, Institut de Genétique et de Biologie Moleculaire et Cellulaire, CNRS/INSERM/UDS, Illkirch Cedex, France. [17]Laboratory of Cellular Transport Systems, Department of Cellular and Molecular Medicine, KU Leuven, Leuven, Belgium. [18]Padova Neuroscience Center (PNC), University of Padova, Padova, Italy. [19]Study Center for Neurodegeneration (CESNE), University of Padova, Padova, Italy. [20]Laboratory for Molecular Cancer Biology, Center for Cancer Biology, VIB, Leuven, Belgium. [21]Department of Oncology, KU Leuven, Leuven, Belgium. ✉e-mail: julie.bonnereau@kuleuven.be; patrizia.agostinis@kuleuven.be

https://doi.org/10.1038/s42255-025-01352-4

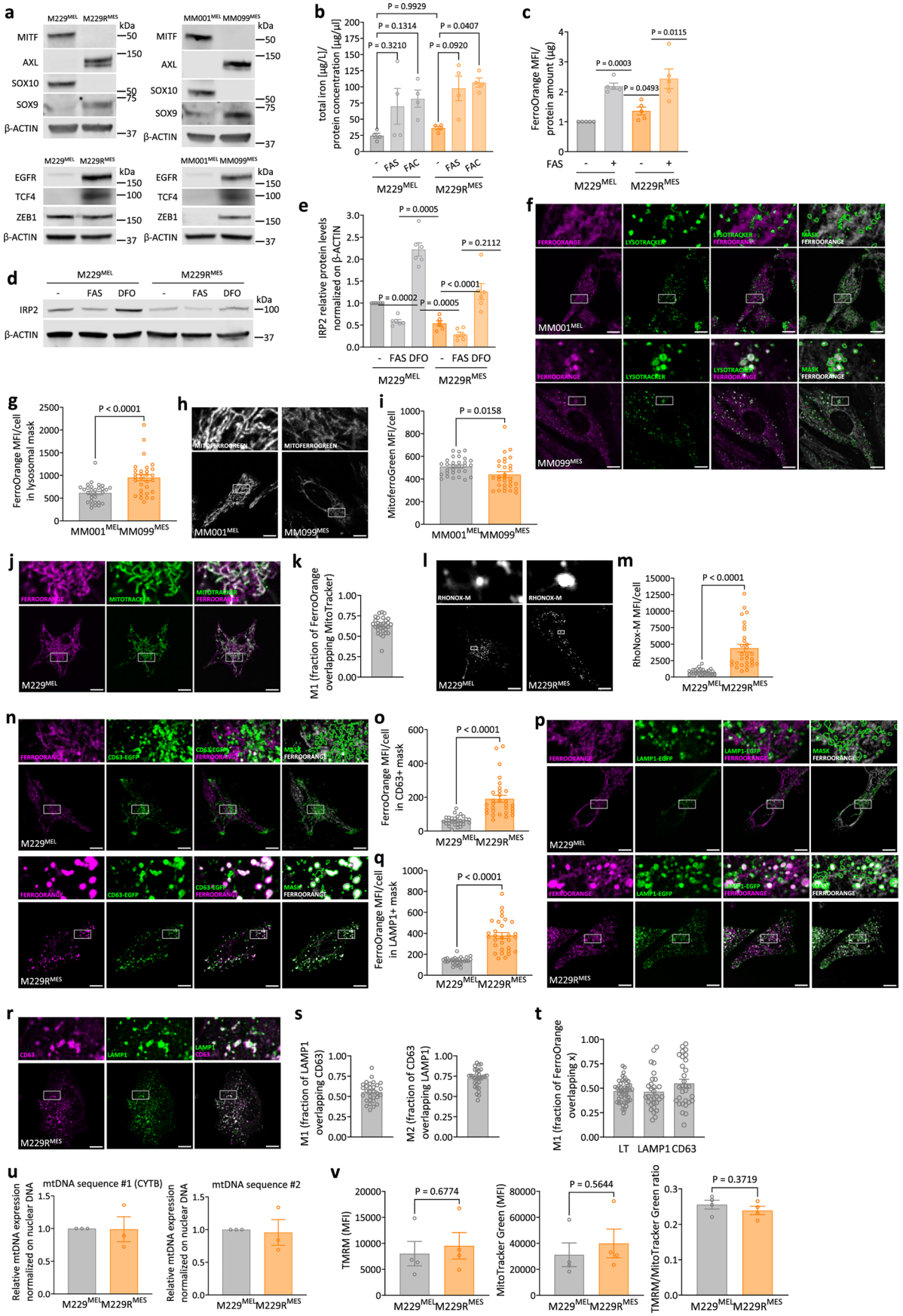

Extended Data Fig. 1 | See next page for caption.

https://doi.org/10.1038/s42255-025-01352-4

Extended Data Fig. 1 | Inter-organelle iron redistribution is a hallmark of the melanoma phenotype switching. a, Representative western blot of MITF, AXL, SOX10, SOX9, EGFR, TCF4, and ZEB1 in $M229^{MEL}$ vs $M229R^{MES}$ and $MM001^{MEL}$ vs $MM099^{MES}$ cells (n = 3). **b**, Total iron (iron(II) and iron(III)) levels by Capillary electrophoresis-inductively coupled plasma mass spectrometry (CE-ICP-MS) in $M229^{MEL}$ and $M229R^{MES}$ cells; Ammonium Iron (II) Sulfate (FAS) and Ammonium Iron (III) Citrate (FAC)-treated cells were used as positive controls (n = 4). **c**, Total iron(II) levels by FerroOrange staining in $M229^{MEL}$ and $M229R^{MES}$ cells; FAS-treated cells were used as positive control (n = 5). **d**,**e**, Representative western blot (**d**) and quantification (**e**) of IRP2 in $M229^{MEL}$ and $M229R^{MES}$ cells, in untreated (−), FAS- and DFO-treated conditions (n = 6). **f**,**g**, Representative images (**f**, scale bar: 10 µm) and quantification of lysosomal iron using FerroOrange mean fluorescence intensity (MFI) per cell within the lysosomal mask (**g**) in $MM001^{MEL}$ (n = 30) and $MM099^{MES}$ (n = 30) cells (three independent experiments). **h**,**i**, Representative images (**h**, scale bar: 10 µm) and quantification of mitochondrial iron using MitoferroGreen mean fluorescence intensity (MFI) per cell (**i**) in $MM001^{MEL}$ (n = 30) and $MM099^{MES}$ (n = 30) cells (three independent experiments). **j**,**k**, Representative images (**j**, scale bar: 10 µm) and quantification of FerroOrange-MitoTracker colocalization (Manders' colocalization coefficient M1) (**k**) in $M229^{MEL}$ (n = 30) cells (three independent experiments). **l**,**m**, Representative images (**l**, scale bar: 10 µm) and quantification of lysosomal iron using RhoNox-M mean fluorescence intensity (MFI) per cell (**m**) in $M229^{MEL}$ (n = 30) and $M229R^{MES}$ (n = 30) cells. **n**,**o**, Representative images (**n**, scale bar: 10 µm) and quantification of lysosomal iron using FerroOrange mean fluorescence intensity (MFI) per cell within the Cd63+ mask (**o**) in $M229^{MEL}$ (n = 30) and $M229R^{MES}$ (n = 30) cells (three independent experiments). **p**,**q**, Representative images (**p**, scale bar: 10 µm) and quantification of lysosomal iron using FerroOrange mean fluorescence intensity (MFI) per cell within the LAMP1+ mask (**q**) in $M229^{MEL}$ (n = 30) and $M229R^{MES}$ (n = 30) cells (three independent experiments). **r**,**s**, Representative images (**s**, scale bar: 10 µm) and quantification of CD63-LAMP1 colocalization (Manders' colocalization coefficients M1 and M2) (**s**) in $M229R^{MES}$ (n = 30) cells (three independent experiments). **t**, Quantification of FerroOrange colocalization with LysoTracker (LT) (n = 48) or CD63 (n = 30) or LAMP1 (n = 30) (Manders' colocalization coefficient M1) in $M229R^{MES}$ cells (three independent experiments). **u**, Relative mitochondrial DNA (mtDNA) levels in $M229^{MEL}$ and $M229R^{MES}$ cells (n = 3). v, Relative mitochondrial membrane potential levels in $M229^{MEL}$ and $M229R^{MES}$ cells stained with TMRM (mitochondrial membrane potential) and MitoTracker green (mitochondrial mass) and measured by flow cytometry (n = 4). Data are presented as the mean ± s.e.m. Statistical significance was assessed by one-way ANOVA (**b**), two-tailed one-sample t-test (**c**, **e, u**), and unpaired two-tailed Student's t-test (**g**, **i**, **m**, **o**, **p**, **v**). Please note that for panel b, an unpaired two-tailed Student's t-test between the basal (−) conditions only would result in a significant difference in total iron levels (p-value = 0.0476).

https://doi.org/10.1038/s42255-025-01352-4

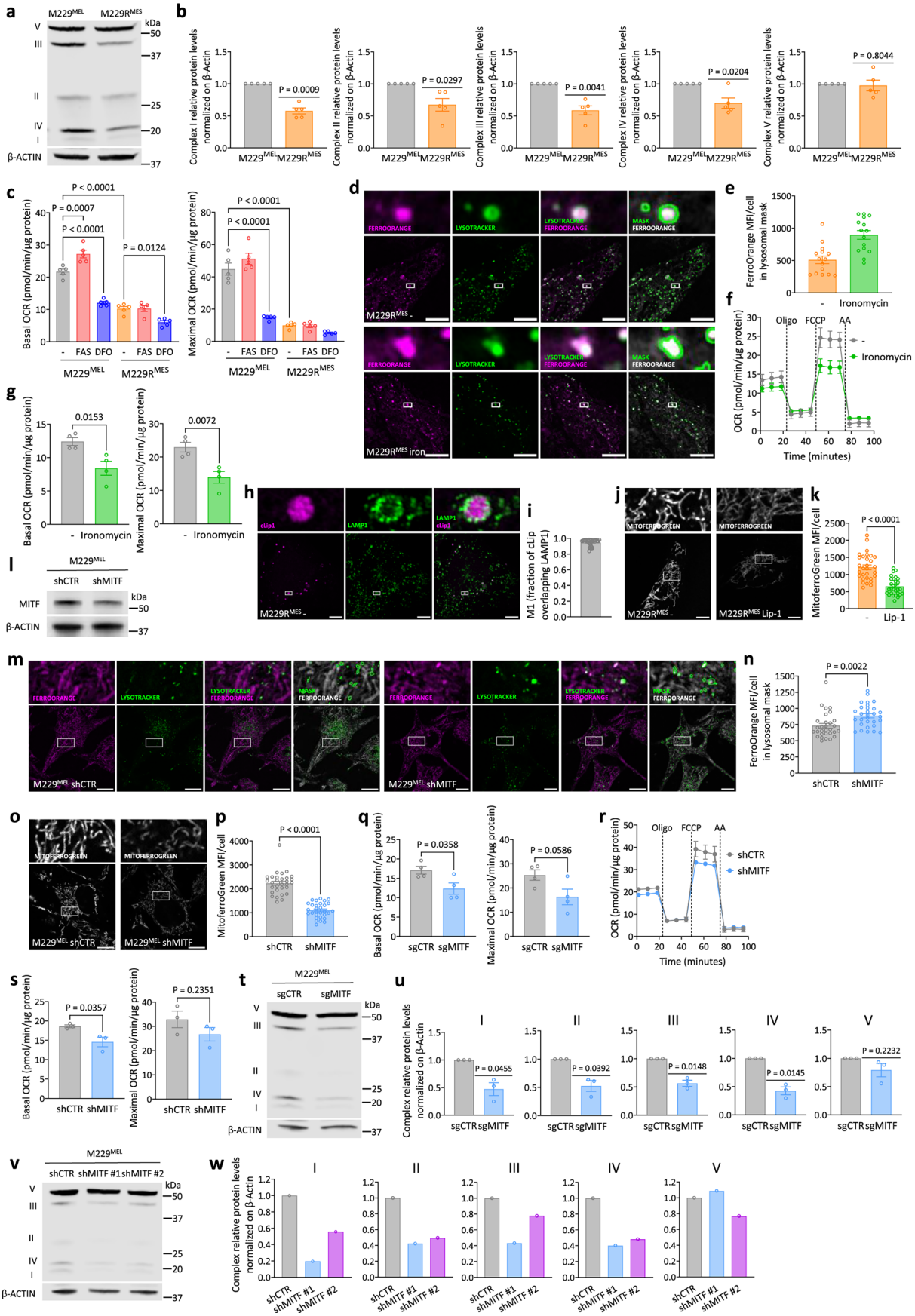

Extended Data Fig. 2 | See next page for caption.

https://doi.org/10.1038/s42255-025-01352-4

Extended Data Fig. 2 | Iron organellar compartmentalization and metabolism are rewired during the melanoma phenotype switching. a,**b**, Representative western blot (**a**) and quantification (**b**) of OXPHOS complexes in $M229^{MEL}$ vs $M229R^{MES}$ cells (n = 3). **c**, Quantification of basal and maximal oxygen consumption rate (OCR) of $M229^{MEL}$ and $M229R^{MES}$ cells in untreated (−), FAS-treated, and DFO-treated conditions (n = 5). **d**,**e**, Representative images (**d**, scale bar: 10 µm) and quantification of lysosomal iron using FerroOrange mean fluorescence intensity (MFI) per cell within the lysosomal mask (**e**) in $M229R^{MES}$ basal (-, n = 15) and ironomycin-treated (n = 15) cells (one biological replicate). **f**,**g**, Oxygen consumption rate (OCR) of $M229^{MEL}$ cells in basal (−) or ironomycin-treated conditions (**f**) and quantification of basal and maximal respiration (**g**) (n = 4). **h**,**i**, Representative images (**h**, scale bar: 10 µm) and quantification of cLip1 and LAMP1 colocalization (Manders' colocalization coefficient M1) (**i**) in $M229R^{MES}$ (n = 29) cells (three independent experiments). **j**,**k**, Representative images (**j**, scale bar: 10 µm) and quantification of mitochondrial iron using MitoferroGreen mean fluorescence intensity (MFI) per cell (**k**) in $M229R^{MES}$ cells in basal (-, n = 30) and liproxstatin1-treated (Lip-1, n = 29) conditions (three independent experiments). **l**, Representative western blot of MITF in $M229^{MEL}$ shCTR and shMITF cells (n = 3). **m**,**n**, Representative images (**m**, scale bar: 10 µm) and quantification of lysosomal iron using FerroOrange mean fluorescence intensity (MFI) per cell within the lysosomal mask (**n**) in $M229^{MEL}$ shCTR (n = 30) and shMITF (m = 30) cells (three independent experiments). **o**,**p**, Representative images (**o**, scale bar: 10 µm) and quantification of mitochondrial iron using MitoferroGreen mean fluorescence intensity (MFI) per cell (**p**) in $M229^{MEL}$ shCTR (n = 30) and shMITF (m = 30) cells (three independent experiments). **q**, Quantification of basal and maximal oxygen consumption rate (OCR) of $M229^{MEL}$ sgCTR and sgMITF cells (n = 4). **r**,**s**, Oxygen consumption rate (OCR) of $M229^{MEL}$ shCTR and shMITF cells (**f**) and quantification of basal and maximal respiration (**g**) (n = 3). **t**,**u**, Representative western blot (**t**) and quantification (**u**) of OXPHOS complexes in $M229^{MEL}$ sgCTR and sgMITF cells (n = 3). v,w, Representative western blot (**v**) and quantification (**w**) of OXPHOS complexes in $M229^{MEL}$ shCTR, shMITF#1, and shMITF#2 cells (n = 1). Data are presented as the mean ± s.e.m. Statistical significance was assessed by two-tailed one-sample t-test (**b**, **u**), one-way ANOVA (**c**), and unpaired two-tailed Student's t-test (**g**, **k**, **n**, **p**, **q**, **s**).

https://doi.org/10.1038/s42255-025-01352-4

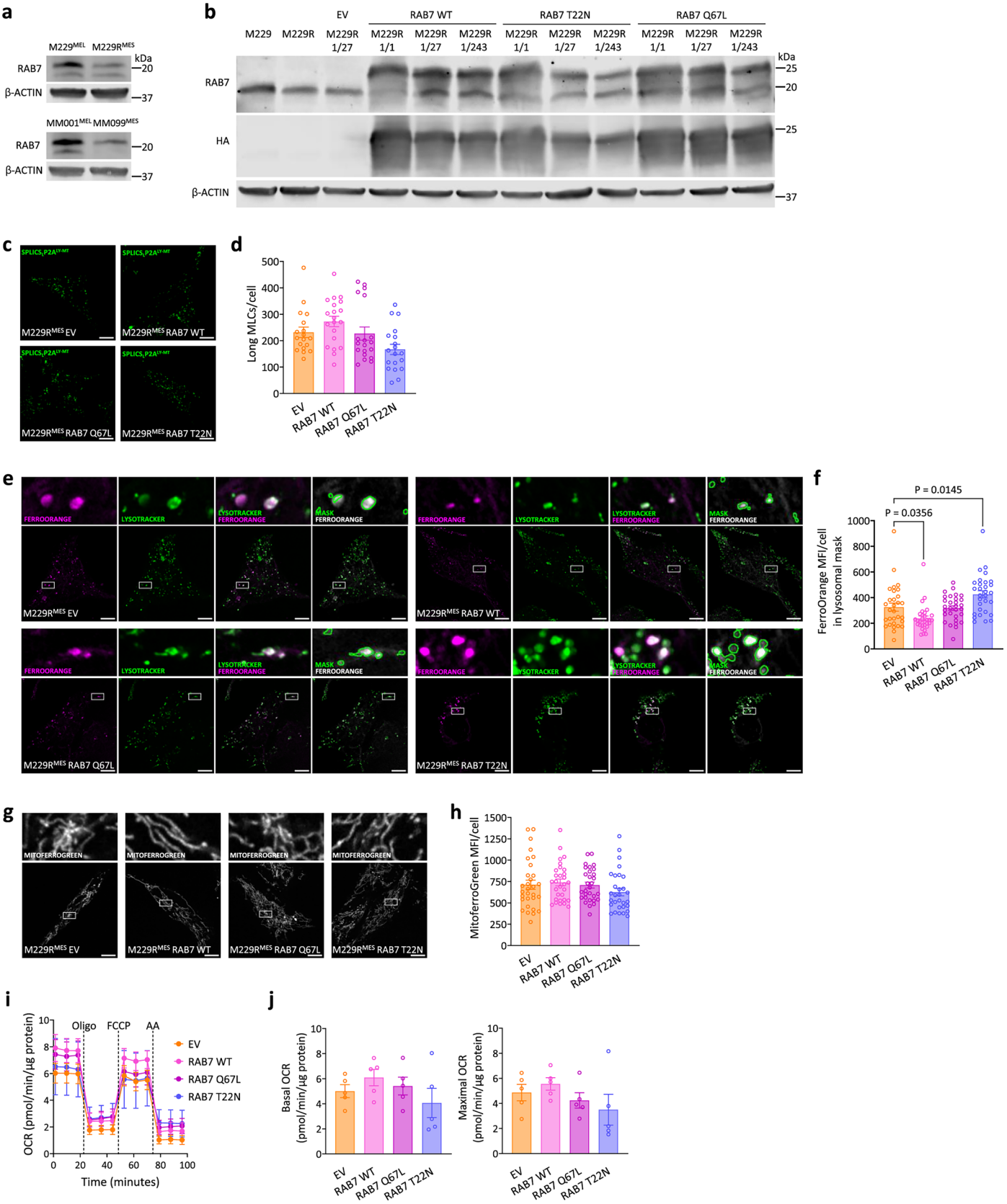

Extended Data Fig. 3 | See next page for caption.

https://doi.org/10.1038/s42255-025-01352-4

Extended Data Fig. 3 | Restoration of RAB7 levels or activity only partially rescues iron compartmentalization and metabolism in MES cells. **a**, Representative western blot of RAB7 in M229^{MEL} vs M229R^{MES} and MM001^{MEL} vs MM099^{MES} cells (n = 3). **b**, Representative western blot of RAB7 and HA in M229^{MEL} and M229R^{MES} WT or stably transduced with an empty vector (EV) or RAB7 WT, RAB7 Q67L, RAB7 T22N vectors. Exogenously expressed RAB7 contains a 2xHA tag. For each vector, several dilutions were tested (1/1, 1/27, 1/243). Final dilution used is 1/27 (n = 1). **c**,**d**, Representative images (**c**, scale bar: 10 µm) and quantification of long MLCs per cell (**d**) in M229R^{MES} EV (n = 18), RAB7 WT (n = 20), RAB7 Q67L (n = 19), and RAB7 T22N (n = 19) cells (two independent experiments). **e**,**f**, Representative images (**e**, scale bar: 10 µm) and quantification of lysosomal iron using FerroOrange mean fluorescence intensity (MFI) per cell within the lysosomal mask (**f**) in M229R^{MES} EV (n = 30), RAB7 WT (n = 30), RAB7 Q67L (n = 30), and RAB7 T22N (n = 30) cells (three independent experiments). **g**,**h**, Representative images (**g**, scale bar: 10 µm) and quantification of mitochondrial iron using MitoferroGreen mean fluorescence intensity (MFI) per cell (**h**) in M229R^{MES} EV (n = 30), RAB7 WT (n = 30), RAB7 Q67L (n = 30), and RAB7 T22N (n = 30) cells (three independent experiments). **i**,**j**, Oxygen consumption rate (OCR) of M229R^{MES} EV, RAB7 WT, RAB7 Q67L, and RAB7 T22N cells (**i**) and quantification of basal and maximal respiration (**j**) (n = 5). Data are presented as the mean ± s.e.m. Statistical significance was assessed by one-way ANOVA (**d**, **f**, **h**, **j**).

https://doi.org/10.1038/s42255-025-01352-4

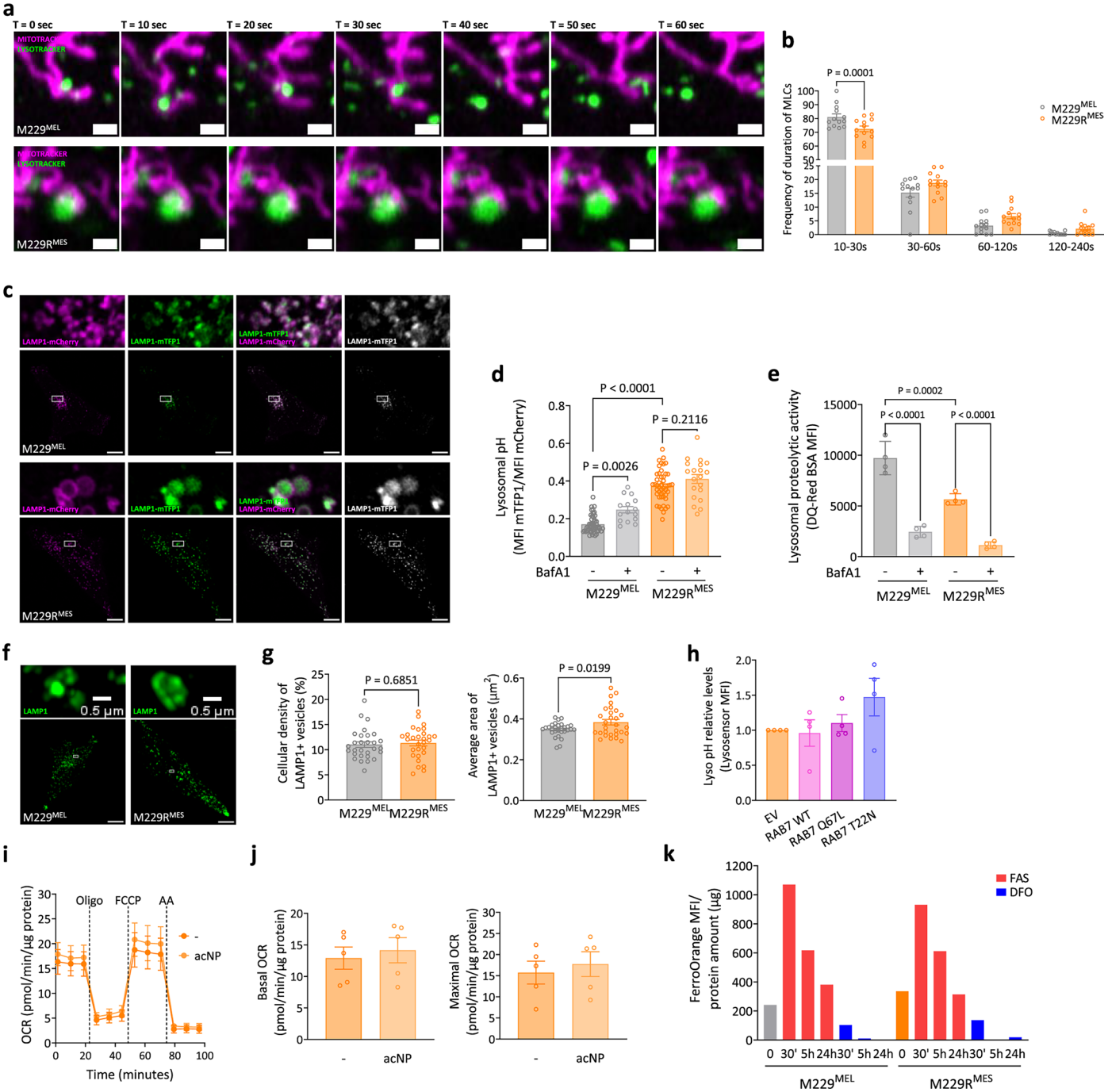

Extended Data Fig. 4 | Restoration of lysosomal acidity only partially rescues iron compartmentalization and metabolism in MES cells. a,**b**, Representative images (**a**, scale bar: 1 µm) and quantification of the frequency of duration of MLCs (**b**) in M229^{MEL} (n = 13) and M229R^{MES} (n = 13) cells (two independent experiments). **c**,**d**, Representative images (**c**, scale bar: 10 µm) and quantification of lysosomal pH (**d**) in M229^{MEL} basal (-, n = 51) or bafilomycinA1-treated (BafA1, n = 15) and M229R^{MES} basal (-, n = 48) or BafA1-treated (n = 20) cells expressing the LAMP1-targeted pH-sensitive mTFP1 biosensor (also called FIRE-pHLy[88]). Lysosomal pH is quantified as ratio mTFP1 mean fluorescent intensity (MFI)/ mCherry MFI, where mTFP1 (monomeric teal fluorescent protein 1) is a pH-sensitive fluorescent protein and mCherry is used for normalization (three independent experiments). **e**, Lysosomal proteolytic activity (DQ-Red BSA MFI) of M229^{MEL} basal (−) or bafilomycin A1-treated (BafA1) and M229R^{MES} basal (−) or BafA1-treated cells (n = 4). **f**,**g**, Representative images (**f**, scale bar: 10 µm for whole-cell image, 0.5 µm for magnified image) and quantification of lysosomal cellular density (%) and average area (µm^2) (**g**) in M229^{MEL} (n = 29) and M229R^{MES} (n = 29) cells fixed and stained using anti-LAMP1 antibody (three independent experiments). **h**, Relative lysosomal pH levels (LysoSensor MFI) of M229^{MES} EV, RAB7 WT, RAB7 Q67L, and RAB7 T22N cells (n = 4). **i**,**j**, Oxygen consumption rate (OCR) of M229R^{MES} cells in untreated (−) or acNP-treated conditions (**i**) and quantification of basal and maximal respiration (**j**) (n = 5). **k**, Total iron(II) levels by FerroOrange staining in M229^{MEL} and M229R^{MES} cells treated with DFO or FAS. Data are presented as the mean ± s.e.m. Statistical significance was assessed by two-way ANOVA (**b**), one-way ANOVA (**d**, **e**), unpaired two-tailed Student's t-test (**g**,**j**), and two-tailed one-sample t-test (**h**).

https://doi.org/10.1038/s42255-025-01352-4

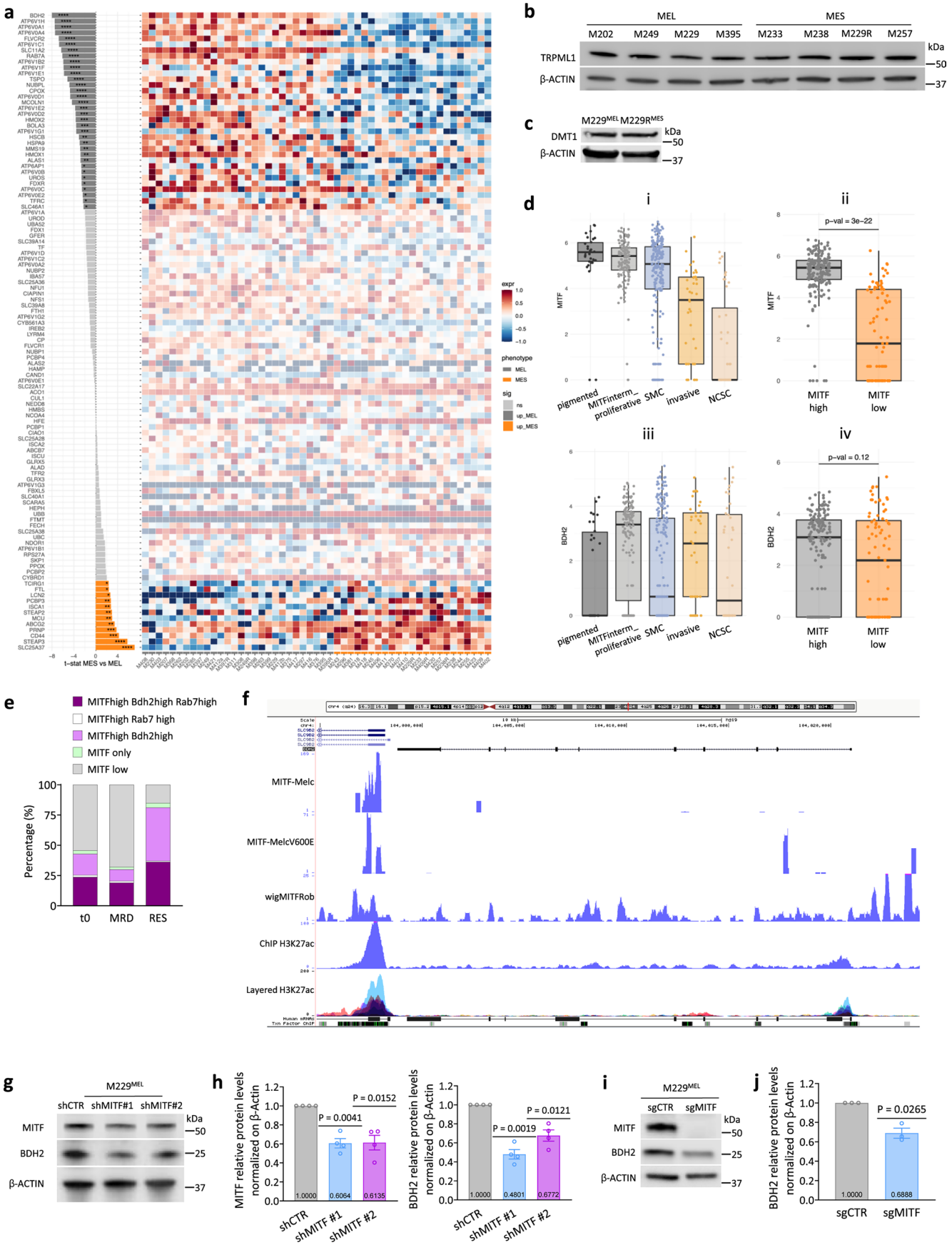

Extended Data Fig. 5 | See next page for caption.

https://doi.org/10.1038/s42255-025-01352-4

Extended Data Fig. 5 | The MES phenotype is associated with reduced levels of BDH2, the mammalian homolog of the bacterial EntA. a, Heatmap showing the statistically significant differentially expressed (DE) iron metabolism-related genes between the two melanoma clusters, MES vs MEL, according to t test. The bar plot on the left reports the t statistics value for each gene. Bars are colored according to the phenotype in which the gene is upregulated. **b**, Representative western blot of TRPML1 in MEL (M202, M249, M229, and M395) and MES (M233, M238, M229R, and M257) cells (n = 1). **c**, Representative western blot of DMT1 in $M229^{MEL}$ and $M229R^{MES}$ cells (n = 1). **d**, Box plots showing MITF (i, ii) and BDH2 (iii, iv) expression in single cells from Rambow et al.[21]. Bars are colored according to cell states as defined in the original publication (i, iii) and grouped by MITF expression (ii, iv), considering 'MITFinterm_melanocytic' as $MITF^{high}$, and 'invasive' and 'NCSC' as $MITF^{low}$. **e**, Percentage of different populations based on their expression of BDH2, MITF, and RAB7 from multiplex co-staining of the primary tumor of the melanoma MEL015 PDX model[21] at different drug-resistant stages in response to dabrafenib/trametinib treatment; MRD: minimal residual disease, RES: resistance. **f**, ChIP-Seq peaks indicating chromatin accessibility regions upstream the BDH2 locus. **g**,**h**, Representative western blot (**g**) and quantification (**h**) of MITF and BDH2 in $M229^{MEL}$ shCTR, shMITF#1, and shMITF#2 cells (n = 4). **i**,**j**, Representative western blot (**i**) and quantification (**j**) of MITF and BDH2 in $M229^{MEL}$ sgCTR and sgMITF cells (n = 3). Data in bar plots are presented as the mean ± s.e.m. Data in the box plot (**d**) represent the median (centre line), the 25th and 75th percentiles (bounds of the box), and the whiskers indicate the minimum and maximum values. Statistical significance was assessed by unpaired two-tailed Student's t-test (**d**), and two-tailed one-sample t-test (**h**,**j**). Stars indicate level of significance: *P < 0.05; **P < 0.01; ***P < 0.001; ****P < 0.0001.

https://doi.org/10.1038/s42255-025-01352-4

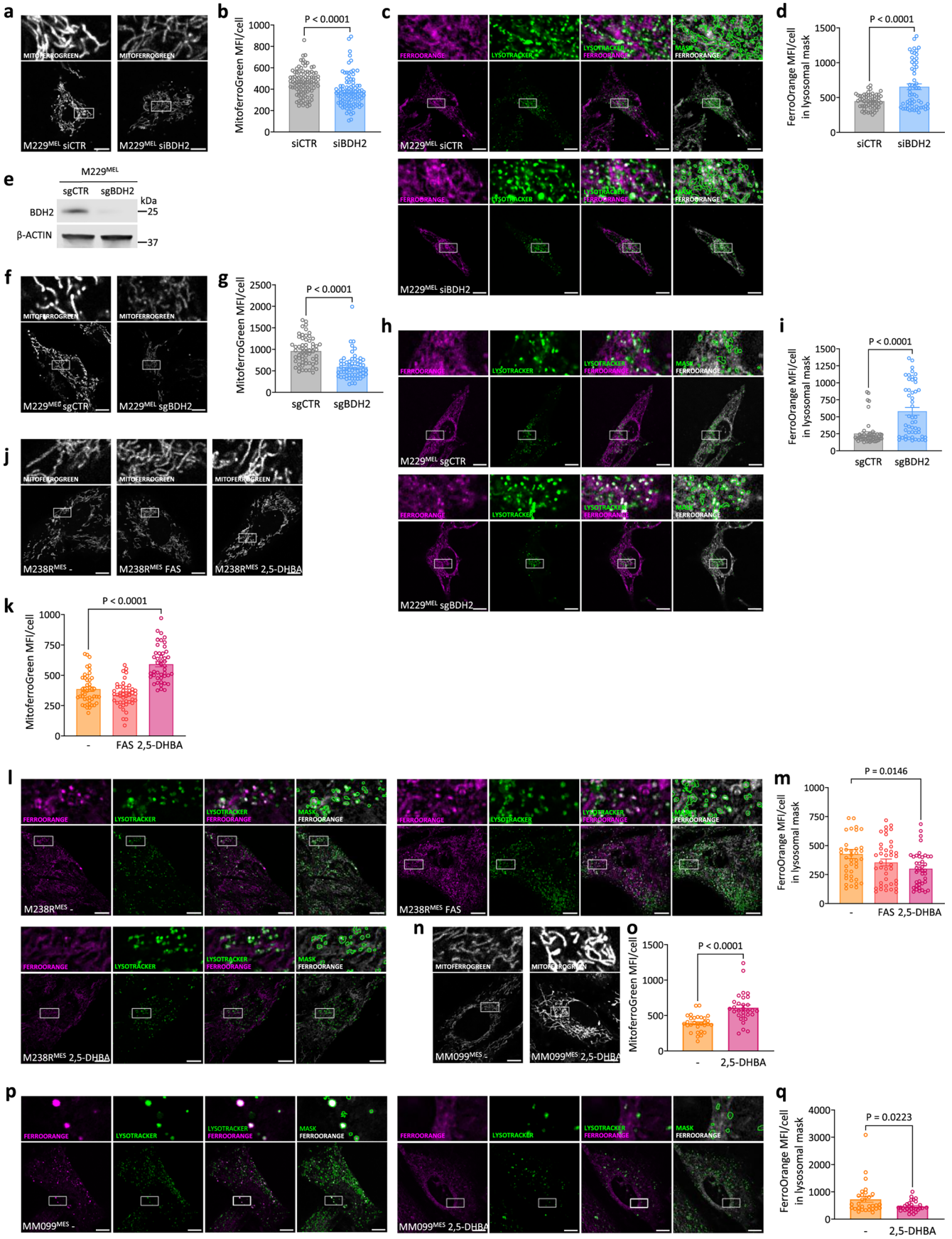

Extended Data Fig. 6 | See next page for caption.

https://doi.org/10.1038/s42255-025-01352-4

Extended Data Fig. 6 | Production of 2,5-DHBA by BDH2 is required for inter-organelle iron transport. a,**b**, Representative images (**a**, scale bar: 10 µm) and quantification of mitochondrial iron using MitoferroGreen mean fluorescence intensity (MFI) per cell (**b**) in M229^{MEL} siCTR (n = 100) and siBDH2 (n = 99) cells (three independent experiments). **c**,**d**, Representative images (**c**, scale bar: 10 µm) and quantification of lysosomal iron using FerroOrange mean fluorescence intensity (MFI) per cell within the lysosomal mask (**d**) in M229^{MEL} siCTR (n = 60) and siBDH2 (n = 60) cells (three independent experiments). **e**, Representative western blot of BDH2 in M229^{MEL} sgCTR and sgBDH2 cells (n = 2). **f**,**g**, Representative images (**f**, scale bar: 10 µm) and quantification of mitochondrial iron using MitoferroGreen mean fluorescence intensity (MFI) per cell (**g**) in M229^{MEL} sgCTR (n = 50) and sgBDH2 (n = 50) cells (three independent experiments). **h**,**i**, Representative images (**h**, scale bar: 10 µm) and quantification of lysosomal iron using FerroOrange mean fluorescence intensity (MFI) per cell within the lysosomal mask (**i**) in M229^{MEL} sgCTR (n = 60) and sgBDH2 (n = 60) cells (three independent experiments). **j**,**k**, Representative images (**j**, scale bar: 10 µm) and quantification of mitochondrial iron using MitoferroGreen mean fluorescence intensity (MFI) per cell (**k**) in M238R^{MES} untreated (-, n = 45), FAS-treated (n = 45), and 2,5-DHBA-treated (n = 45) cells (three independent experiments). **l**,**m**, Representative images (**l**, scale bar: 10 µm) and quantification of lysosomal iron using FerroOrange mean fluorescence intensity (MFI) per cell within the lysosomal mask (**m**) in M238R^{MES} untreated (-, n = 40), FAS-treated (n = 40), and 2,5-DHBA-treated (n = 40) cells (three independent experiments). **n**,**o**, Representative images (**n**, scale bar: 10 µm) and quantification of mitochondrial iron using MitoferroGreen mean fluorescence intensity (MFI) per cell (**o**) in MM099^{MES} untreated (-, n = 30) and 2,5-DHBA-treated (n = 30) cells (two independent experiments). **p**,**q**, Representative images (**p**, scale bar: 10 µm) and quantification of lysosomal iron using FerroOrange mean fluorescence intensity (MFI) per cell within the lysosomal mask (**q**) in MM099^{MES} untreated (-, n = 30) and 2,5-DHBA-treated (n = 30) cells (two independent experiments). Data are presented as the mean ± s.e.m. Statistical significance was assessed by unpaired two-tailed Student's t-test (**b**, **d**, **g**, **I**, **o**, **q**), one-way ANOVA (**k**), and Kruskal-Wallis test (**m**).

https://doi.org/10.1038/s42255-025-01352-4

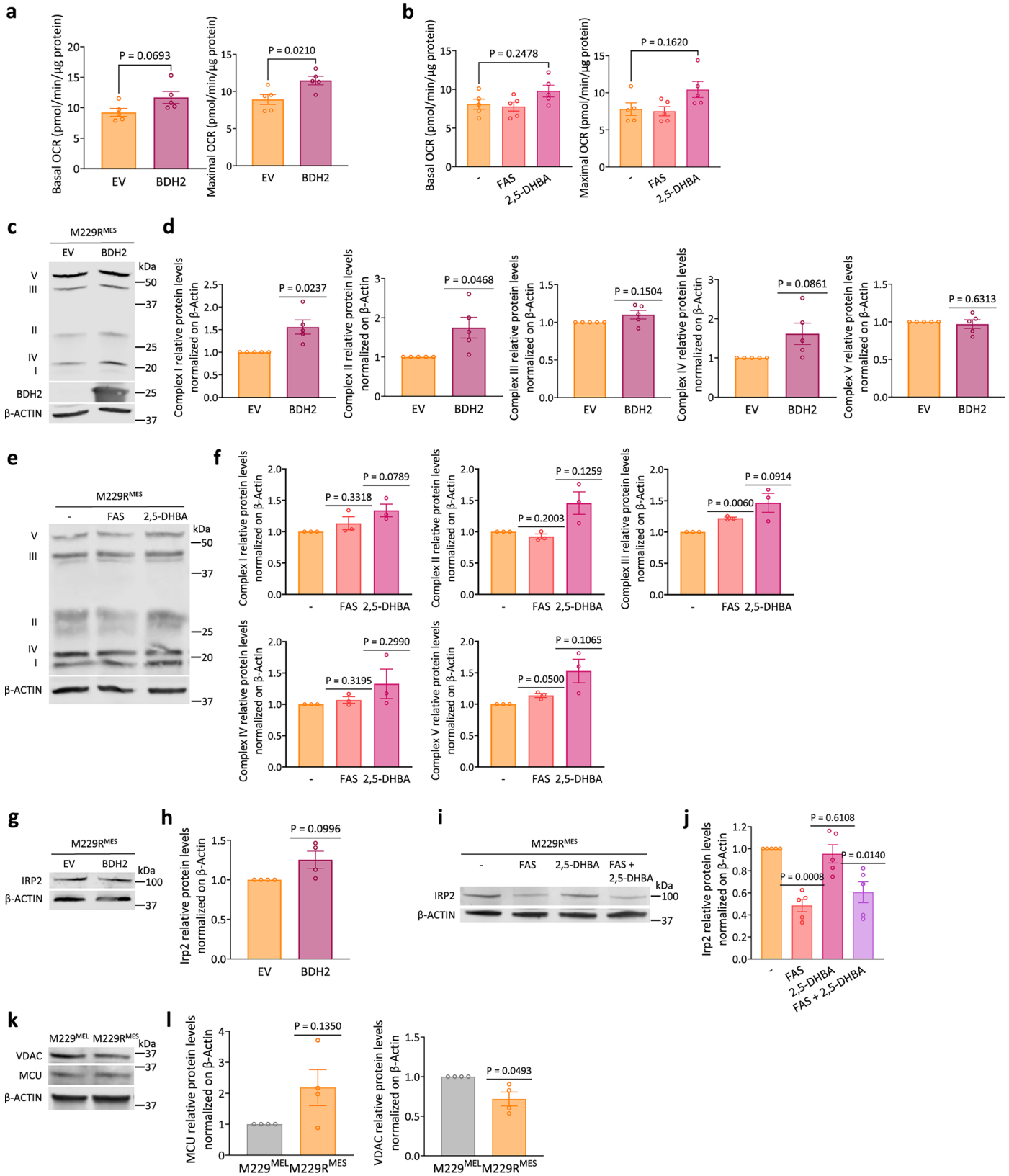

Extended Data Fig. 7 | Restoration of the BDH2-2,5-DHBA axis improves mitochondrial iron levels and metabolism in MES cells. a, Quantification of basal and maximal oxygen consumption rate (OCR) of M229R^{MES} EV and BDH2 cells (n = 3). **b**, Quantification of basal and maximal oxygen consumption rate (OCR) of M229R^{MES} cells untreated and treated with FAS and 2,5-DHBA (n = 5). **c**,**d**, Representative western blot (**c**) and quantification (**d**) of OXPHOS complexes in M229R^{MES} EV and BDH2 cells (n = 5). **e**,**f**, Representative western blot (**e**) and quantification (**f**) of OXPHOS complexes in M229R^{MES} cells untreated and treated with FAS and 2,5-DHBA (n = 3). **g**,**h**, Representative western blot (**g**) and quantification (**h**) of IRP2 in M229R^{MES} EV and BDH2 cells (n = 4). **i**,**j**, Representative western blot (**i**) and quantification (**j**) of IRP2 in M229R^{MES} cells untreated and treated with FAS and 2,5-DHBA (n = 5). **k**,**l**, Representative western blot (**k**) and quantification (**j**) of VDAC and MCU in M229^{MEL} and M229R^{MES} cells (n = 3). Data are presented as the mean ± s.e.m. Statistical significance was assessed by unpaired two-tailed Student's t-test (**a**), one-way ANOVA (**b**), and two-tailed one-sample t-test (**d**, **f**, **h**, **j**).

https://doi.org/10.1038/s42255-025-01352-4

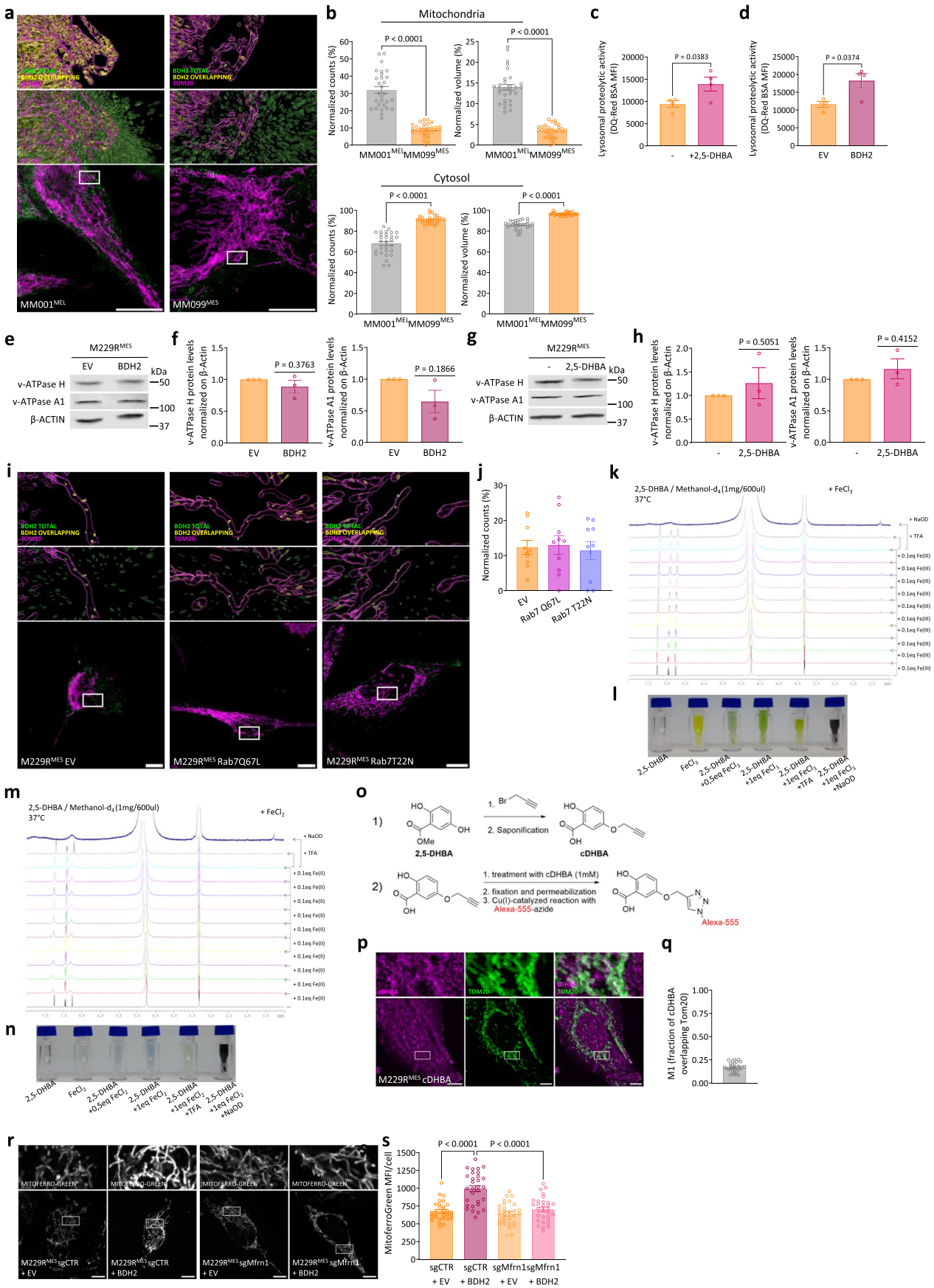

Extended Data Fig. 8 | See next page for caption.

https://doi.org/10.1038/s42255-025-01352-4

Extended Data Fig. 8 | BDH2 localizes at the mitochondria-lysosome contacts to regulate lysosomal pH and MLC formation. a,**b**, Representative SIM images (**a**, scale bar: 10 µm) and quantification of BDH2 intracellular localization (**b**) in MM001^{MEL} (n = 29) and MM099^{MES} (n = 30) cells (three independent experiments). **c**, Lysosomal proteolytic activity (DQ-Red BSA MFI) of M229R^{MES} basal (−) and 2,5-DHBA-treated cells (n = 4). **d**, Lysosomal proteolytic activity (DQ-Red BSA MFI) of M229R^{MES} EV and BHD2 cells (n = 4). **e**,**f**, Representative western blot (**e**) and quantification (**f**) of v-ATPase H and v-ATPase A in M229R^{MES} EV and BHD2 cells (n = 3). **g**,**h**, Representative western blot (**g**) and quantification (**h**) of v-ATPase H and v-ATPase A in M229R^{MES} untreated (−) and 2,5-DHBA-treated cells (n = 3). **i**,**j**, Representative SIM images (**i**, scale bar: 10 µm) and quantification of BDH2 intracellular localization (**j**) in M229R^{MES} EV (n = 10), RAB7 Q67L (n = 10), and RAB7 T22N (n = 10) cells (two independent experiments). **k**,**l**, ^{1}H NMR spectra of 2,5-DHBA (10.8 mM) in presence of $FeCl_3$ recorded at 310 K in methanol-d_4. $FeCl_3$ was added in portions of 0.1 mol. eq. up to 1.0 eq. Then, a drop of trifluoroacetic acid (TFA) and sodium deuteroxide (NaOD) was added. **m**,**n**, ^{1}H NMR spectra of 2,5-DHBA (10.8 mM) in presence of $FeCl_2$ recorded at 310 K in methanol-d_4. $FeCl_2$ was added in portions of 0.1 mol. eq. up to 1.0 eq. Then a drop of trifluoroacetic acid (TFA) and sodium deuteroxide (NaOD) was added. **o**, Schematics of the experimental procedure for in-cell labelling of CDHBA by click chemistry. **p**,**q**, Representative images (**p**, scale bar: 10 µm) and quantification of cDHBA-Tom20 colocalization (Manders' colocalization coefficient M1) (**q**) in M229R^{MES} cells (n = 30, three independent experiments). **r**,**s**, Representative images (**r**, scale bar: 10 µm) and quantification of mitochondrial iron using MitoferroGreen mean fluorescence intensity (MFI) per cell (**s**) in M229R^{MES} sgCTR EV (n = 30) or BDH2 (n = 30), and sgMitoferrin-1 (Mfrn1) EV (n = 30) or BDH2 (n = 30) cells (three independent experiments). Data are presented as the mean ± s.e.m. Statistical significance was assessed by unpaired two-tailed Student's t-test (**b**, **c**, **d**), two-tailed one-sample t-test (**f**, **h**), and one-way ANOVA (**j**, **s**).

https://doi.org/10.1038/s42255-025-01352-4

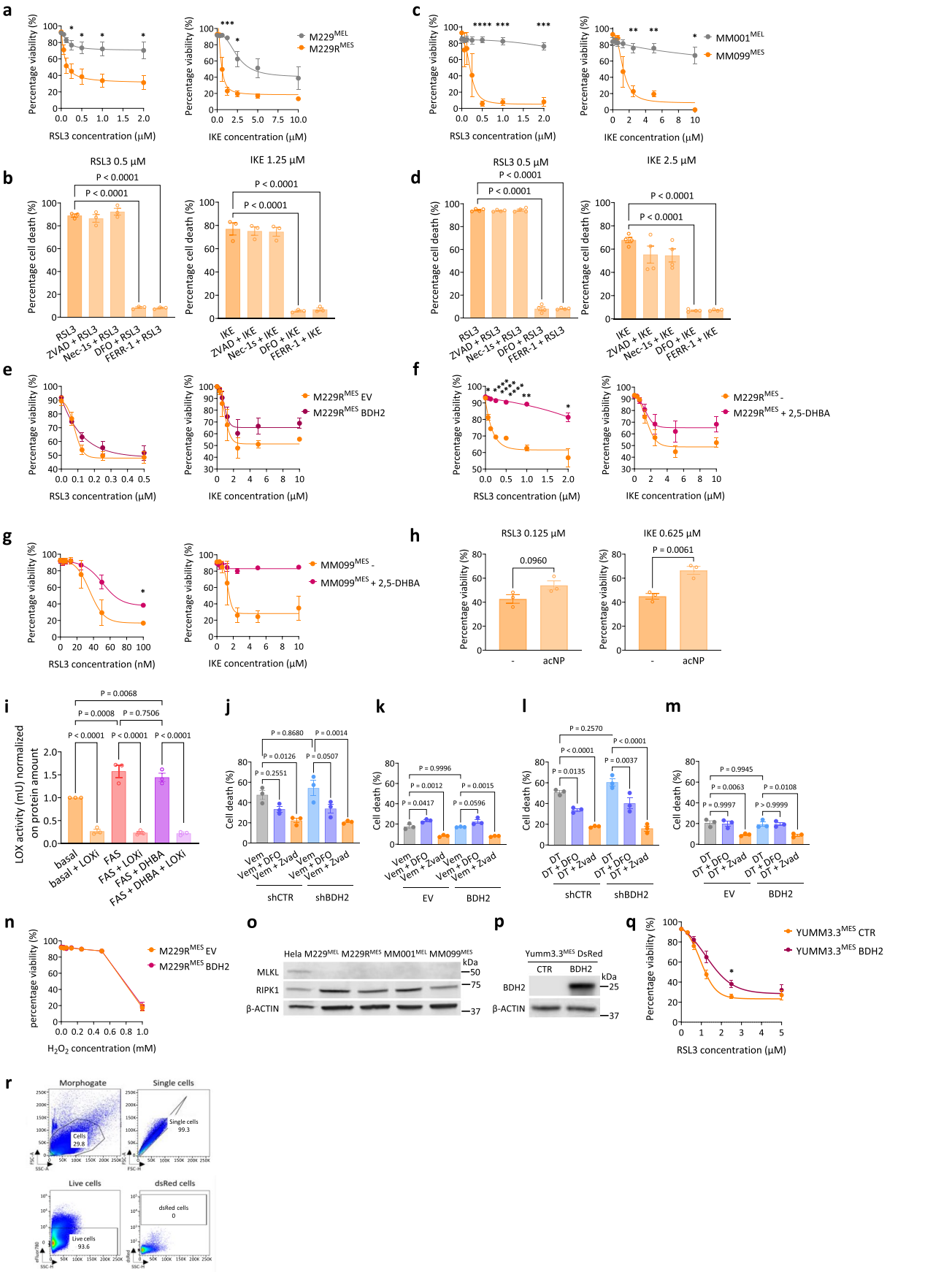

Extended Data Fig. 9 | See next page for caption.

https://doi.org/10.1038/s42255-025-01352-4

Extended Data Fig. 9 | The BDH2-2,5-DHBA axis protects MES cells against ferroptosis *in vitro* and in the bloodstream. a, Percentage of viability of $M229^{MEL}$ and $M229R^{MES}$ cells upon treatment with increasing doses of RSL3 and IKE (n = 4). **b**, Percentage of cell death of $M229R^{MES}$ cells upon RSL3 (0.5 µM) or IKE (1.25 µM) treatment alone (−) or in combination with several cell death inhibitors (30 µM Z-VAD-FMK (ZVAD), 30 µM necrostatin-1s (Nec-1s), 100 µM deferoxamine (DFO), 2 µM ferrostatin-1 (Ferr-1)) (n = 3). **c**, Percentage of viability of $MM001^{MEL}$ and $MM099^{MES}$ cells upon treatment with increasing doses of RSL3 and IKE (n = 4). **b**, Percentage of cell death of $MM099^{MES}$ cells upon RSL3 (0.5 µM) or IKE (2.5 µM) treatment alone (−) or in combination with several cell death inhibitors (30 µM Z-VAD-FMK (ZVAD), 30 µM necrostatin-1s (Nec-1s), 100 µM deferoxamine (DFO), 2 µM ferrostatin-1 (Ferr-1)) (n = 4). **e**, Percentage of viability of $M229R^{MES}$ EV and BDH2 cells upon treatment with increasing doses of RSL3 and IKE (n = 3). **f**, Percentage of viability of $M229R^{MES}$ untreated (−) and 2,5-DHBA-treated cells upon treatment with increasing doses of RSL3 and IKE (n = 5). **g**, Percentage of viability of $MM099^{MES}$ untreated (−) and 2,5-DHBA-treated cells upon treatment with increasing doses of RSL3 and IKE (n = 2). **h**, Percentage of viability of $M229R^{MES}$ untreated (−) and acNP-treated cells upon RSL3 (0.125 µM) and IKE (0.625 µM) (n = 3). **i**, Relative lipoxygenase (LOX) activity in $M229R^{MES}$ cells in basal condition versus FAS treatment alone and in combination with 2,5-DHBA; treatment with LOX inhibitor (LOXi) was used as a negative control for the assay. **j**, Percentage of cell death of $M229^{MEL}$ shCTR and shBDH2 cells upon Vemurafenib (Vem) treatment alone (−) and in combination with DFO or ZVAD (n = 3). **k**, Percentage of cell death of $M229R^{MES}$ EV and BDH2 cells upon Vemurafenib (Vem) treatment alone (−) and in combination with DFO or ZVAD (n = 3). **l**, Percentage of cell death of $M229^{MEL}$ shCTR and shBDH2 cells upon Dabrafenib/Trametinib (DT) treatment alone (−) and in combination with DFO or ZVAD (n = 3). **m**, Percentage of cell death of $M229R^{MES}$ EV and BDH2 cells upon Dabrafenib/Trametinib (DT) treatment alone (−) and in combination with DFO or ZVAD (n = 3). **n**, Percentage of viability of $M229R^{MES}$ EV and BDH2 cells upon treatment with increasing doses of H_2O_2 (n = 4). **o**, Representative western blot of MLKL and RIPK1 in $M229^{MEL}$, $M229R^{MES}$, $MM001^{MEL}$, $MM099^{MES}$ cells; HeLa cells were used as a positive control for MLKL and RIPK1 expression. **p**, Representative western blot of BDH2 in $YUMM3.3^{MES}$ CTR and BDH2 cells. **q**, Percentage of viability of $YUMM3.3^{MES}$ CTR and BDH2 cells upon treatment with increasing doses of RSL3 (n = 4). **r**, Gating strategy used to detect the dsRed cells in the lungs. The dsRed cells were detected among the single and live (eFluor780 viability) cells; the dsRed gate was set up using lungs coming from non-injected mice. Data are presented as the mean ± s.e.m. Statistical significance was assessed by unpaired two-tailed Student's t-test (**a**, **c**, **e**, **f**, **g**, **h**, **n**, **q**), one-way ANOVA (**b**, **d**, **j**, **k**, **l**, **m**), and two-tailed one-sample t-test (**i**). Stars indicate level of significance: *P < 0.05; **P < 0.01; ***P < 0.001; ****P < 0.0001.

nature portfolio

Corresponding author(s): Patrizia Agostinis

Last updated by author(s): Jul 7, 2025

Reporting Summary

Nature Portfolio wishes to improve the reproducibility of the work that we publish. This form provides structure for consistency and transparency in reporting. For further information on Nature Portfolio policies, see our Editorial Policies and the Editorial Policy Checklist.

Statistics

For all statistical analyses, confirm that the following items are present in the figure legend, table legend, main text, or Methods section.

n/a	Confirmed
☐	☒ The exact sample size (*n*) for each experimental group/condition, given as a discrete number and unit of measurement
☐	☒ A statement on whether measurements were taken from distinct samples or whether the same sample was measured repeatedly
☐	☒ The statistical test(s) used AND whether they are one- or two-sided *Only common tests should be described solely by name; describe more complex techniques in the Methods section.*
☒	☐ A description of all covariates tested
☐	☒ A description of any assumptions or corrections, such as tests of normality and adjustment for multiple comparisons
☐	☒ A full description of the statistical parameters including central tendency (e.g. means) or other basic estimates (e.g. regression coefficient) AND variation (e.g. standard deviation) or associated estimates of uncertainty (e.g. confidence intervals)
☐	☒ For null hypothesis testing, the test statistic (e.g. *F*, *t*, *r*) with confidence intervals, effect sizes, degrees of freedom and *P* value noted *Give P values as exact values whenever suitable.*
☒	☐ For Bayesian analysis, information on the choice of priors and Markov chain Monte Carlo settings
☒	☐ For hierarchical and complex designs, identification of the appropriate level for tests and full reporting of outcomes
☒	☐ Estimates of effect sizes (e.g. Cohen's *d*, Pearson's *r*), indicating how they were calculated

Our web collection on statistics for biologists contains articles on many of the points above.

Software and code

Policy information about availability of computer code

Data collection	4D-Nucleofector (Lonza Bioscience) for transient transfection and CRISPR-Cas9 gene knockout. Zeiss LSM880 microscope for confocal (Airyscan) imaging. Olympus IX81 Cell^R microscope for widefield imaging. Inverted Zeiss Elyra 7 microscope and Nikon Ti2 N-SIM S microscope for SIM imaging. Akoya PhenoImager HT for multiplex imaging. PrinCe 706 capillary electrophoresis system for iron measurment. Synergy H1 Multimode reader (BioTek) for fluorescence measurment in plate reader assays. BD LSFortessa X-20 + HTS and BD FACSCanto II system (BD Biosciences) flow cytometers for flow cytometry analyses. Dionex UltiMate 3000 LC System (Thermo Scientific) for metabolomics. Typhoon infrared-imaging system (GE Healthcare) or ChemidocTM MP system (Bio-Rad Laboratories) for immunoblotting. ABI7500 system (Applied Biosystems) for quantitative-real-time PCR. Seahorse XFe24 Analyzer (Agilent) for seahorse assays. 500MHz Bruker spectrometer for NMR experiments.
Data analysis	ImageJ/Fiji, Imaris (v10.2) and QuPath (v0.6.0) softwares for mciroscopy analysis. FCS Express (v6) and FlowJo (v10.10) for flow cytometry data analyses. Xcalibur software for metabolomics. Image Studio (v6.0, Li-Cor Biosciences) software for immunoblotting analysis. Seahorse Wave Software online (Agilent) for seahorse analyses. R (v4.1.3) for in silico analyses. GraphPad Prism v10.4.2 for statistical analysis of all experiments.

For manuscripts utilizing custom algorithms or software that are central to the research but not yet described in published literature, software must be made available to editors and reviewers. We strongly encourage code deposition in a community repository (e.g. GitHub). See the Nature Portfolio guidelines for submitting code & software for further information.

Data

Policy information about availability of data

All manuscripts must include a data availability statement. This statement should provide the following information, where applicable:

- Accession codes, unique identifiers, or web links for publicly available datasets
- A description of any restrictions on data availability
- For clinical datasets or third party data, please ensure that the statement adheres to our policy

Gel source images are provided in this paper. All other data supporting the findings of this study are available within the article and Supplementary Information and from the corresponding author on reasonable request. Source data are provided with this paper.

Research involving human participants, their data, or biological material

Policy information about studies with human participants or human data. See also policy information about sex, gender (identity/presentation), and sexual orientation and race, ethnicity and racism.

Reporting on sex and gender	N/A
Reporting on race, ethnicity, or other socially relevant groupings	N/A
Population characteristics	N/A
Recruitment	N/A
Ethics oversight	N/A

Note that full information on the approval of the study protocol must also be provided in the manuscript.

Field-specific reporting

Please select the one below that is the best fit for your research. If you are not sure, read the appropriate sections before making your selection.

☒ Life sciences ☐ Behavioural & social sciences ☐ Ecological, evolutionary & environmental sciences

For a reference copy of the document with all sections, see nature.com/documents/nr-reporting-summary-flat.pdf

Life sciences study design

All studies must disclose on these points even when the disclosure is negative.

Sample size	For all analysis a minimum of 3 independent biological replicates unless specified. No statistical methods were applied to predefine sample size. We based on our lab's previous experience in determining the power for disclosing specific effects.
Data exclusions	No data was excluded in any experiments.
Replication	All attempts at replication and reproducibility of the experimental findings were successful. This information has been added to the corresponding figure legend.
Randomization	Sample were allocated randomly into experimental groups.
Blinding	The investigators analyzing the data were blinded to experimental groups/treatments assignment.

Reporting for specific materials, systems and methods

We require information from authors about some types of materials, experimental systems and methods used in many studies. Here, indicate whether each material, system or method listed is relevant to your study. If you are not sure if a list item applies to your research, read the appropriate section before selecting a response.

Materials & experimental systems

n/a	Involved in the study
☐	☒ Antibodies
☐	☒ Eukaryotic cell lines
☒	☐ Palaeontology and archaeology
☐	☒ Animals and other organisms
☒	☐ Clinical data
☒	☐ Dual use research of concern
☒	☐ Plants

Methods

n/a	Involved in the study
☒	☐ ChIP-seq
☐	☒ Flow cytometry
☒	☐ MRI-based neuroimaging

Antibodies

Antibodies used

For imaging, anti-LAMP1 (Ab25630, abcam), anti-TOM20 (ab186735, abcam), anti-LAMP1 (ab24170, abcam), anti-TOM20 (ab289670 and ab186735 abcam), anti-BDH2 (sc-393030, Santa Cruz Biotechnology), anti-BDH2 (NBP2-32713, Novus Biologicals), anti-SLC25A37 (26469-1, ProteinTech), anti-MITF (HPA003259, Sigma) and anti-RAB7 (9367, Cell Signaling), secondary antibodies conjugated with Alexa Fluor 488/546/647 (A11030, A11034, A48265, A11029, Invitrogen), secondary Envision+/HRP goat anti-Rabbit (K4003, Dako Envision+ Single Reagents); For western blot, anti-MITF (MA5-14154, Thermo Fischer Scientifics), OxPhos Human WB Antibody Cocktail (45-8199, Thermo Fisher Scientific), anti-BDH2 (27207-1-AP, Proteintech), anti-DMT1 (20507-1-AP, Proteintech), anti-SOX10 (sc-365692, Santa Cruz Biotechnology), anti-v-ATPase H (sc-166227, Santa Cruz Biotechnology) and anti-v-ATPase A (sc-374475, Santa Cruz Biotechnology), anti-AXL (8661, Cell Signaling), ani-SOX9 (82630, Cell Signaling), anti-IRP2 (37135, Cell Signaling), anti-RAB7 (2094, Cell Signaling), HA-Tag (14904, Cell Signaling), anti-TRPML1 (ab28508, abcam), anti-EGFR (4267, Cell Signaling), anti-TCF4 (ab217668, Abcam), anti-ZEB1 (3396, Cell Signaling), anti-MLKL (14993, Cell Signaling), anti-RIPK1 (TA800357, OriGene), anti-VDAC (4866, Cell Signaling), anti-MCU (HPA016480, Sigma), anti-β-ACTIN (A5441, Sigma-Aldrich), secondary antibodies (7074S, 7076S, Cell Signaling) for HRP detection, secondary antibodies (35568, 5A535521, Invitrogen) for infrared detection. All primary antibodies were diluted 1:1000, anti-β-ACTIN antibody was diluted 1:2000, and seconday antibodies 1:2000.

Validation

All antibodies used in this manuscript were commercially bought and validated by the manufacturers, as mentioned on their website. All antibodies were used to detect the respective protein at the expected molecular weight or subcellular localization.

Eukaryotic cell lines

Policy information about cell lines and Sex and Gender in Research

Cell line source(s)

human melanoma cell lines were a kind gift of Dr. G. Ghanem, Dr. R. Lo (UCLA), and Dr. A. Ribas. Murine melanoma cell line Yumm 3.3 was a gift by Dr. Alpaslan Tasdogan.

Authentication

Cell line used were not authenticated

Mycoplasma contamination

Cells were regularly checked for mycoplasma contamination and used only when testing mycoplasma negative.

Commonly misidentified lines
(See ICLAC register)

No misidentified cell lines were used in this study.

Animals and other research organisms

Policy information about studies involving animals; ARRIVE guidelines recommended for reporting animal research, and Sex and Gender in Research

Laboratory animals

C57BL/6 7-week-old female mice were used for all the experiments.

Wild animals

n.a.

Reporting on sex

Only female mice were used as the YUMM3.3 mouse melanoma cell line used for in vivo experiments was derived from a 4-hydroxytamoxifen-induced melanoma tumor in a female C57BL/6J mouse. Female mice were distinguished from male mice by checking the presence of nipples and the anogenital distance.

Field-collected samples

n.a.

Ethics oversight

Animal procedures were approved by the Institutional Animal Care and Research Advisory Committee of the KU Leuven (ECD P116/2023) and were performed following the institutional and national guidelines and regulations.

Note that full information on the approval of the study protocol must also be provided in the manuscript.

Plants

Seed stocks	N/A
Novel plant genotypes	N/A
Authentication	N/A

Flow Cytometry

Plots

Confirm that:

☒ The axis labels state the marker and fluorochrome used (e.g. CD4-FITC).

☒ The axis scales are clearly visible. Include numbers along axes only for bottom left plot of group (a 'group' is an analysis of identical markers).

☒ All plots are contour plots with outliers or pseudocolor plots.

☒ A numerical value for number of cells or percentage (with statistics) is provided.

Methodology

Sample preparation	For in vitro experiments, cells were stained with DQ Red BSA (D12051, Thermo Fisher Scientifics), Tetramethylrhodamine (TMRM) (T668, Thermo Fisher Scientifics), MitoTracker green (M7514, Thermo Fisher Scientifics), BODIPY 581/591 C11 (D3861, Thermo Fisher Scientifics), eBioscience Fixable Viability Dye eFluor 780 (65-0865, Thermo Fisher Scientifics) according to the manufacturer's instructions. For in vivo experiments, the lungs were cut in small fragments in a petri dish and put in gentleMACS™ C Tubes holding 3mL of digestion solution (DMEM F12 medium completed with Gibco™ Collagenase Type II (10mg/mL), Type IV (25mg/mL) and DNAse I (15µg/mL)). The samples were run on the gentleMACS™ Octo Dissociator following three consecutive programs: (1) 30 seconds 600 rpm at room temperature, (2) 30 min 600 rpm at 37°C, and (3) 30 seconds 600 rpm at room temperature. After digestion, the samples were passed through a 70 µm pluriStrainer Mini, washed with PBS, and counted. 10 million cells from each lung sample were stained with a viability dye (eFluor780) for 30 min on ice. After washing, all the samples were recorded on the BD Fortessa Cytometer.
Instrument	BD FACS Canto™ II and BD LSFortessa X-20 + HTS flow cytometers.
Software	Analysis was performed using FCS Express and FlowJo softwares.
Cell population abundance	10 million cells from each lung sample were stained with a viability dye (eFluor780). Among total lung live cells, dsRed+ cancer cells were between 0 and 50,000, as indicated in fig. 6.
Gating strategy	SSC-A vs FSC-A for the morphogate, FSC-H vs FSC-A and SSC-A vs SSC-H for doublets discrimination, PE-Cy7 for eFluor780 for live cells, and then FITC for MitoTracker green, PE for TMRM, APC for DQ Red BSA, FITC and PE for Bodipy C11.

☒ Tick this box to confirm that a figure exemplifying the gating strategy is provided in the Supplementary Information.